Growth and Characterization of Non-Hydrazine Solution Processed $Cu_2(ZnSn)(SSe)_4$ Thin Films for Solar Cells

A Thesis

in partial fulfillment of the requirement for the award

of

Doctor of Philosophy

submitted by

Indu Gupta
(Regd. No. 901312001)

THAPAR INSTITUTE
OF ENGINEERING & TECHNOLOGY
(Deemed to be University)

School of Physics and Materials Science
Thapar Institute of Engineering and Technology, Patiala 147004, India
July, 2019

DEDICATED

TO

MY LOVING GRANDPARENTS AND PARENTS

THESIS CERTIFICATE

I hereby certify that work presented in this thesis entitled **"Growth and Characterization of Non-Hydrazine Solution Processed $Cu_2ZnSn(SSe)_4$ Thin Films for Solar Cells"** in partial fulfillment of the requirement of the award of degree of DOCTOR OF PHILOSOPHY in the School of Physics and Materials Science, Thapar Institute of Engineering and Technology, Patiala is an authentic record of my own work carried out under supervision of Dr. Bhaskar Chandra Mohanty. The matter embodied in this thesis has not been submitted in part or full to any other university or institute for the award of any degree.

Indu Gupta

Indu Gupta

This is to certify that the above statement made by the candidate is true to the best of my knowledge.

Research Guide

5/8/2019

(Dr. Bhaskar Chandra Mohanty)
Associate Professor
School of Physics and Material Sciences
Thapar Institute of Engineering and Technology
Patiala

ACKNOWLEDGEMENT

Prima facea, I am grateful to the God for the good health and wellbeing that were necessary to complete this thesis.

I would like to express my sincere gratitude to my advisor, Assoc. Prof. Bhaskar Chandra Mohanty for introducing me to the diverse and dynamic field of photovoltaics. Experimenting with this material calls for multidisciplinary approach, combining chemistry, physics and material science. I am grateful for his support and assistance during my thesis.

Furthermore, I would like to thank Dr. Puneet Sharma, Dr. Poonam Uniyal and Dr. Hardeep Singh for being part of my thesis committee, as well as for all the fruitful discussions.

I am very grateful to Dr. Bhupendra N. Chudasama from Nano medicine Lab, School of Physics and Material Sciences for allowing me to use their equipment for optical measurements and Dr. Poonam Uniyal and Dr. D. P. Singh and his student Shobhneek Kaur for letting me use their equipment for electrical measurements.

I would also like to thank Dr. P. Malar from SRM institute of engineering and technology, Chennai and her team for her collaboration during this study.

I am especially grateful to my laboratory colleagues, Neetu Bansal, Kaushlendra Pandey and Jyoti Jangra for their support and assistance to my work.

I thank all my friends for their great support throughout the tough times, for being so positive, supportive and helpful.

Lastly, I offer sincere thanks to my grandparents (Mr. Chaman Lal and late Mrs. Angoori Devi), parents (Mr. Surinder Nath and Mrs. Santosh kumari) and my brothers (Mr. Vijay Goyal and Mr. Mohit Garg) for their love, motivation, encouragement, and unlimited patience throughout my education.

Indu Gupta

ABSTRACT

Kesterite Cu_2ZnSnS_4 (CZTS) has emerged as a very promising absorber layer in thin film solar cells due to its earth abundant environmentally benign constituents and suitable optical properties. So far, the highest conversion efficiency of 12.6% for Se-alloyed CZTS (CZTSSe) films has been obtained by the solution process using hydrazine based slurry. Considering the explosive, hepatotoxic and carcinogenic nature of hydrazine, there have been wider research on facile synthesis of CZTS films from non-hydrazine non-toxic solutions. In this work, the CZTSSe films have been prepared from ethanol based homogeneous solutions using a direct solution coating route via dip coating. Firstly, ethanol, besides being an environmentally friendly solvent, solvates many common inorganic salts and can evaporate quickly (boiling point is ~78.5 °C) which can minimize residual carbon and/or oxygen related impurities in the films. Secondly, contrary to the approaches relying on fabricating thin films from CZTS particle-containing inks, homogeneous solution method offers several advantages such as better stoichiometric control (due to mixing at molecular-scale) and no requirement of pre-fabrication and stabilization of CZTS particles.

In the CZTS device technology, the requirement of phase purity, dense microstructure with large grains, conformally deposited film thickness of ~ 1 μm, appropriate band gap (1.0 - 1.5 eV) and electrical properties of the films are very critical for obtaining high efficiency of the devices. In the solution based approaches for semiconductor thin films, the film growth proceeds from the release of cations and anions from the precursor salts, and their subsequent reactions. The reaction pathway depends on various process parameters (such as temperature, precursor composition, deposition duration, complexing agent, etc.) and determines the eventual microstructure and phase of the films. In this thesis, while growing CZTS films from ethanol based solutions containing common metal salts, the influence of the process parameters has been investigated in detail and attempts were made to develop an understanding of the reaction pathway leading to the formation of sub-micrometer thick single phase kesterite CZTS films from the precursor solution via intermediate solid state binary and ternary compounds during deposition and the subsequent sulfurization/selenization treatment.

While investigating the role of complexing agents, we found that the presence of monoethanolamine (MEA) - a routinely used complexing agent - in the initial stage of solution mixing, inhibits complete reduction (oxidation) of Cu^{2+} (Sn^{2+}), which subsequently affected the reaction pathway resulting in undesirable secondary phases. On the other hand, the activation

energy for the decomposition of the precursor complex was found to be smaller, surmounted in the early formation of the single phase CZTS in the absence of MEA.

Another important aspect of growth of the CZTS thin films is the post-deposition high temperature annealing (HTA), which must be carefully controlled first to weaken the bonds in the organic-inorganic complexes, and then to allow reactions to yield the eventual films. We have studied the influencing mechanisms of phase evolution by employing ten possible HTA settings with elemental sulfur that includes systematic variations in ramp rate, sulfur source temperature and reaction temperature. Phase pure kesterite CZTS was found to have formed only in one instance, highlighting the crucial dependence of reaction path on the HTA setting. The proposed HTA strategy for reproducible growth of phase pure kesterite CZTS films is based on the geometry-controlled confinement of the sulfur vapor flux nearer to the reacting surface of the precursor film creating a sufficiently high partial pressure of sulfur that promoted growth of kesterite CZTS and prevented its decomposition reaction at elevated temperatures.

The thickness of the films and the grain size was significantly improved with minimum process steps with an intuitive optimization of precursor solution concentration and the sulfurization and selenization ambience - amount of S and Se flakes, heat treatment duration and temperature. It was found that in just two dipping cycles from precursor solutions having 1.0 M $CuCl_2$ solution direct solution coating followed by sulfurization at 500 °C, phase pure kesterite CZTS films of ~850 nm thickness can be obtained. Additionally, in contrast to the reported bilayered structure (i.e., performance limiting small-grained bottom layer and large grained top layer), the resulting films exhibited a conformal microstructure with reasonably large grains. Selenization of the above-obtained phase pure CZTS films at 575 °C for 15 min with 1.5 gm of Se resulted in single phase CZTSSe thin films with Se/S+Se ratio of 0.68 and bandgap of 1.06 eV. These films having a thickness of 1.2 μm exhibited a very compact and large-grained microstructure. Thus, in the given experimental setting, this presents a case of optimized condition for the formation of CZTSSe films for photovoltaic application.

In order to complete the p-n junction for the solar cells, n-type CdS thin films were prepared from ammonia free solutions in the chemical bath deposition approach. The ammonia-free recipe to prepare the CdS films assumes importance in that it helps to reduce the overall toxicity of the wastage from the film deposition process. We have found that the properties of the films grown from ammonia-free solutions are very similar to those of the films grown from solutions with

ammonia as reported in literature. The films were grown at different bath temperatures, namely at 40, 60 and 80 °C and the bath temperature dependence and scaling of surface roughness of the films were studied. From the series of the atomic force micrographs of films of varying deposition times, power spectral density and height-height correlation functions were evaluated, and roughness and growth exponents were determined. The surface width $w(r,t)$ for small r exhibited power law scaling dependence on t, but differently at local and global scale, which is typical of anomalous scaling. We find that deposition at 40 °C yielded films suitable for application in CZTS based devices.

Solar cells in a typical structure of glass/Mo/CZTS/CdS/i:ZnO/ZnO:Al/Al were fabricated and a maximum efficiency of 0.49 % has been obtained. The main reason of the poor performance of the devices may be the low J_{SC} and the very low fill-factor (FF). The low FF has been attributed to the high series resistance and low shunt resistance of the device, which originate from the poor microstructure, reactions at interfaces, and inappropriate electrical properties of the window layers. Further studies have been suggested to improve the performance of the devices.

LIST OF TABLES

LIST OF FIGURES

LIST OF PUBLICATIONS

1. **Indu Gupta**, Bhaskar Chandra Mohanty

   "Dynamic surface evolution of semiconductor thin films grown from a chemical bath", ***Scientific Reports***, 6 (2016) 33136. doi.org/10.1038/srep33136

2. **Indu Gupta**, Preeti Gupta, Bhaskar Chandra Mohanty

   "Synthesis of non-hydrazine solution processed $Cu_2(ZnSn)S_4$ thin films for solar cells applications", ***AIP Conference Proceedings***, 1832 (2017) 080024. doi.org/10.1063/1.4980484

3. **Indu Gupta**, Bhaskar Chandra Mohanty

   "Eliminating secondary phases: Understanding kesterite phase evolution of Cu_2ZnSnS_4 thin films grown from ethanol based solutions with high photosensitivity", ***Solar Energy***, 181 (2019) 214-221. doi.org/10.1016/j.solener.2019.01.098

4. **Indu Gupta**, Kunal J. Tiwari, P. Malar, Bhaskar Chandra Mohanty

   "Evaluating the role of precursor concentration in facile conformal coating of sub-micrometer thick Cu_2ZnSnS_4 films using non-toxic ethanol based solutions", ***Applied Surface science***, 494 (2019) 795-804. doi.org/10.1016/j.apsusc.2019.07.246

5. **Indu Gupta**, Kaushlendra Pandey, Alok Jain, P. Malar, Bhaskar Chandra Mohanty

   "Facile geometry-controlled heat treatment with sulfur flakes strategy for growth of kesterite Cu_2ZnSnS_4 thin films from environment-friendly solutions", (Under review, ***Thin Solid Films***)

6. **Indu Gupta**, Bhaskar Chandra Mohanty

   "Influence of temperature on evolution of properties of Ammonia-free Chemical Bath Deposited CdS Thin Films" ***36th European Photovoltaic Solar Energy Conference and Exhibition***, 704 (2019). doi.org/10.4229/EUPVSEC20192019-3BV.1.60

7. **Indu Gupta**, Alok Jain, P. Malar, Bhaskar Chandra Mohanty "Influencing mechanism of selenization configuration on the grain growth, optical and electrical properties of $Cu_2ZnSn(S,Se)_4$ thin films prepared from environment-friendly solutions", (to be submitted to ***J. Phys. Chem. C***)

LIST OF ORAL AND POSTERS PRESENTATIONS IN INTERNATIONAL AND NATIONAL CONFERENCES

1. **European Photovoltaics Solar Energy Conference 2019** held at Marseille, France on 8th – 13th Sept. 2019.

   Influence of temperature on evolution of properties of Ammonia-free Chemical Bath Deposited CdS Thin Films. (Visual Presentation)

2. **International Conference on Applied Surface Sciences 2019**, held at Pisa Italy on 17th – 20th June 2019.

   Influencing Mechanism of Selenization duration on the grain growth of $Cu_2ZnSn(S,Se)_4$ thin film prepared from non-toxic ethanol based solution process. (Poster Presentation)

3. **International Conference on Nanotechnology: Ideas, Innovations and Initiatives 2017** held at IIT Roorkee, Rooekee from 6th – 8th Dec. 2017.

   Effect of sulfurization process on the growth of ethanol based solution processed Cu_2ZnSnS_4 thin films. (Oral Presentation)

4. **International Conference on Thin Films 2017** held at NPL, Delhi from 14th – 17th Nov. 2017.

   Growth of phase pure kesterite Cu_2ZnSnS_4 thin films from hydrazine free solutions: Effect of variation in copper concentration. (Poster Presentation)

5. **International Conference on Nanoscience and Nanotechnology 2017** held at SRM University, Chennai from 9th – 11th Aug. 2017.

   Influence of concentration of MEA on Cu_2ZnSnS_4 thin films grown by ethanol based solution process. (Oral Presentation)

6. **International Conference on Solar Energy Photovoltaics 2016** held at KIIT University, Bhuvneshwar, Orissa from 17th – 19th Dec. 2016.

   Phase evolution during growth of Cu_2ZnSnS_4 thin films grown by an ethanol based solution process. (Oral Presentation)

7. **DAE Solid State Physics Symposium 2016** held at KIIT University Bhubaneswar, Orissa from 26th – 30th Dec. 2016.

   Synthesis of non-hydrazine solution processed $Cu_2(ZnSn)S_4$ thin films for solar cells applications. (Poster Presentation)

8. **Conference on Microscopy in Materials Science 2015** held at Thapar University, Patiala.

Synthesis of non-hydrazine solution processed $Cu_2(ZnSn)(S,Se)_4$ thin films for solar cells applications. (Poster Presentation)

9. **International Conference on Recent Advances in Nano Science and Technology 2015** held at Sathyabama University, Chennai from 8th – 10th Jul. 2015.

   Bath Temperature dependent properties of ammonia-free chemical bath deposited CdS Thin Films. (Oral Presentation)

CONTENTS

CHAPTER 1 INTRODUCTION

CHAPTER 2 EXPERIMENTAL DETAILS

CHAPTER 7 EFFECT OF Se ALLOYING IN CZTS THIN FILMS

CHAPTER – 1
INTRODUCTION

1.1 ENERGY BACKGROUND

Increasing industrialization concurrent to modernization of lifestyles of a fast-rising world population has increased the energy demand by many fold. So far, fossil fuel has been the major source of energy. However, in addition to the depletion of this fuel at an alarming rate and the environmental threat (such as global warming) arising from the combustion of this fuel have becomes issues of serious concern. In fact, it was concluded by the United Nations Inter-governmental Panel on Climate Change (IPCC)that the global mean temperature increase of 2.0 to 2.4 °C can only be reduced by the reduction of CO_2 emissions by 50 - 80 % by 2050 [1]. In recent years, photovoltaics has emerged as a key alternative energy technology that promises to mitigate the energy crisis to a significant extent. It employs solar cells and modules consisting of an absorber layer - a semiconductor - that absorbs the incident photons and produces excitons. These excitons are harnessed to produce electricity. Since the sun light is abundant, nonpolluting, available free of charge, and cannot be monopolized by a single nation, the future of this technology is very bright.

As per a conservative estimation, the global energy demand in 2018 was 14,301 Mtoe [2]. A simple calculation reveals that the global energy demand can be met if only 1.5 percent of the planet's total land area (i.e., 10% of deserts) are covered with 2% efficiency solar cells. Despite this huge potential, the electricity derived from solar photovoltaics globally is only about 2.1% of the total electricity produced in 2018 [2]. One of the major reasons that has limited the wider use of solar cells is the cost of solar cell production and installation [3]. Till date, the solar cell market is dominated by the panels made from high purity crystalline silicon (first generation solar cells). The processing of such high quality silicon is expensive and drives the cost of the eventual devices. More recently, solar cells based on thin (~1 μm) films of semiconductor materials have emerged as potential substitutes to the silicon based devices. The typical thin coatings of $Cu(InGa)Se_2$ and CdTe) have shown excellent absorption coefficient, when compared with crystalline silicon. These thin coatings absorb the same energy as the crystalline silicon materials. In addition, purity and quality of the crystal remains less stringent in thin film absorbers than those of the crystalline silicon. With the advances in the thin film technology, cheap manufacturing of thin films on a variety of substrates (such as flexible or rigid, metal or insulator) has been possible. Such versatility enables engineering and designing of the layer to improve the device characteristics and performance. Thus the thin film solar cell technology is expected to fabricate the devices on large scale at significantly reduced cost.

The key factors that influence the suitability of thin film semiconductor as absorber layers in thin film solar cells are bandgap and absorption coefficient in the available range of solar radiation. Figure 1.1 shows the typical spectrum of sun radiation on the earth's surface. Since the maximum energy is received in the wavelength region 400 to 100 nm, this is the region that a photovoltaic cell must respond to, in order to yield maximum possible energy output. In single bandgap photovoltaics, there is a tradeoff between absorbing many photons and getting high energy electrons. Photons with energies below the bandgap of the absorber material will not be absorbed and photons with energy above the bandgap provide no increase in efficiency; they only heat the solar cell. In 1961, Shockley and Queisser predicted the maximum efficiency of single junction solar cells to be ~30% [4]. The maximum efficiency turned out to be with a bandgap of between 1.1 eV and 1.4 eV. Not surprisingly, thin film devices with Cu(InGa)Se_2 (CIGS) and CdTe absorber layers having bandgap in this range have been very successful with efficiencies >22% [5].

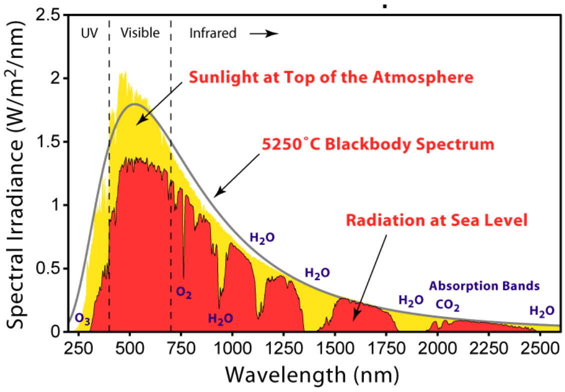

Fig. 1.1: The typical spectrum of sun radiation on the earth's surface [4].

It may also be noted that there are many other forms of photovoltaic devices. For example, dye sensitized and halide perovskite based solar cells have shown very promising results [6,7]. In particular, the halide perovskites which exhibit a direct bandgap, unlike Si, have drawn high research interest due to rapidly improved performance. In a decade's time, the highest efficiency has been achieved to be better than 22% [8]. Although stability of the perovskite halides remains an issue, global efforts have been going on to prepare air-stable high efficiency cost-effective devices [9].

1.2 Cu_2ZnSnS_4 BASED THIN FILMS FOR SOLAR CELLS

Among various absorber thin films, CIGS and CdTe based devices have shown record efficiencies of 22.0 % and 20.4 % [5,10], respectively in the laboratory, while their corresponding commercially available modules have reached the efficiencies of as high as 19.2 % and 17.0 % [11,12]. However, these popular absorber layers use elements which is either toxic (*e.g.*, cadmium) or rare in the earth's crust (*e.g.*, indium, tellurium). The abundance of the elements in these materials in the earth's crust are shown in Fig. 1.2. A number of other thin film materials are being examined as a possible absorber layers grown through cost-competitive techniques. With the group III element indium replaced by a group II element, zinc, and a group IV element, tin, in CIS, copper zinc tin sulfide Cu_2ZnSnS_4 (CZTS) has emerged as a leading absorber candidate over the last few years. Along with the abundantly presence in the earth crust, non-toxic, and cost effective constituents, CZTS exhibits a high absorption coefficient of $\sim 10^4$ cm^{-1} and a direct tunable bandgap (in the range from 1 to 1.5 eV by suitably doping with selenium) that can favorably match the solar spectrum [13,14]. Thus, the CZTS material appears to be both financially and environmentally viable without serious constraints from raw materials. Table 1.1 shows the progression of performance of the CZTS based thin film solar cells over the years. So far, the highest efficiency of 12.6% has been obtained for devices with selenium alloyed-CZTS absorber films [15].

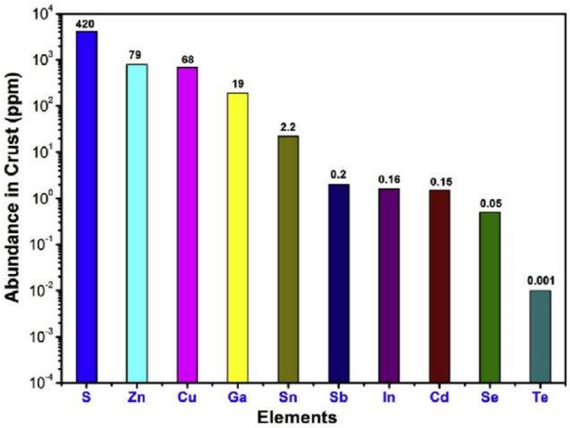

Fig. 1.2: Comparison of the abundance of the various elements in the earth's crust used in thin film solar cells [16].

Table 1.1: The progression of performance of the CZTS based thin film solar cells over the years

Process Used	η (%)	Year [Ref]
Electron beam evaporation of Cu/Sn/Zn stacks	0.6	1996 [17]
Annealing of co-deposited Cu-Zn-Sn films under Sulfur atmosphere.	2.3	1997 [18]
Modified sulfidization of the Cu/Sn/ZnS stacks	2.6	1999 [19]
Turbo pump evacuated sulfidation chamber was used which reduced the contamination from the residual gas.	5.4	2003 [20]
Film deposited by RF magnetron sputtering followed by soaking in deionized water.	6.7	2008 [21]
Precursors containing metal binary chalcogenides and hydrazine was spin coated followed by selenization	9.6	2010 [22]
Cu, Zn and Sn solutions with hydrazine, heated in a sulfur-rich atmosphere using a hot plate at 540°C with S/S+Se=0.4	10.1	2012 [23]
Cu-Zn-Sn precursor solution was prepared in hydrazine and varied the concentration of sulfur in the atmosphere during the final heat treatment.	11.1	2013 [24]
Prepared CZTSSe films by using hydrazine-based solutions and optimized the thickness of TCO and CdS so that the photon transmission to the absorber can be maximized.	12.6	2014 [15]

1.2.1 Crystal structure and phase diagram of CZTS

CIGS and CZTS materials have similar properties as they are derived from the chalcopyrite structure of CIS in which In and Ga was substituted by Zn and Sn atoms, respectively. CZTS is reported to crystallize in either kesterite (KS) (space group I4) or stannite (SS) (I42m) structure (Fig. 1.3) and can be deduced from the sphalerite structure by duplicating the unit cell. The difference between the KS and the SS lies in the ordering of cation sub lattice. As shown in Fig. 1.3a, in kesterite crystal, cation layers of Cu-Sn, Cu-Zn, Cu-Sn and Cu-Zn lies alternately at z = 0, ¼, ½ and ¾, respectively whereas in stannite crystal, Zn-Sn layers alternate with Cu-Cu layers are formed as shown in Fig. 1.3b [25]. The kesterite structure is reportedly more stable because of the lower negative formation energy than that of stannite structure [26].

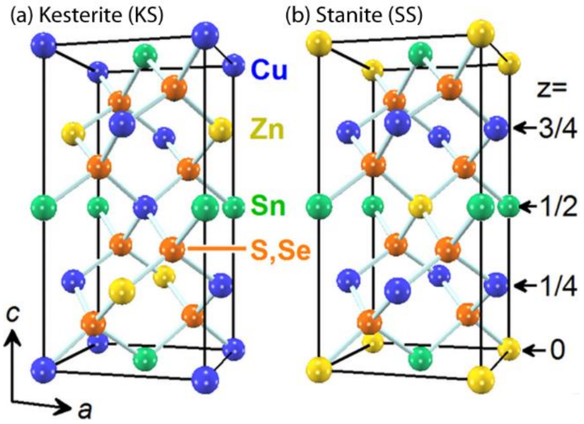

Fig. 1.3: (a) Kesterite (KS) and (b) Stannite structures (SS) of CZTS thin films [25].

CZTS is a p-type semiconductor compound which contains intrinsic point defects including vacancies (V_{Cu}, V_{Zn}, V_{Sn}, and V_S), antisite defects (Cu_{Zn}, Zn_{Cu}, Cu_{Sn}, Sn_{Cu}, Zn_{Sn}, and Sn_{Zn}), and interstitial defects (Cu_i, Zn_i, and Sn_i) [27]. Commonly observed Cu_{Zn} antisite defect in which a Cu atom and Zn atom exchange sub lattices give rise to p-type conductivity for CZTS semiconductor material. This implies that desired electrical properties in CZTS material can be obtained from stoichiometric ratio with Cu-poor, Zn-rich compositions which produce undesired second phase. The formation of these secondary phases can be investigated from the phase diagrams as shown in Fig 1.4. This ternary phase diagram was evolved [28] on the basis of the research by Olekseyuk et al. [29]. Even though CZTS is a quaternary compound, the phase diagram can be degenerated to three constituent by assuming to always get right amount of sulfur in samples [30]. In this diagram, depending on the atomic composition of each element, each field represents formation of CZTS phase along with the secondary phases. There are ten fields which shows that the feasibility of formation of secondary phase is very high. The pure CZTS phase formation is possible only in the middle or eleventh region.

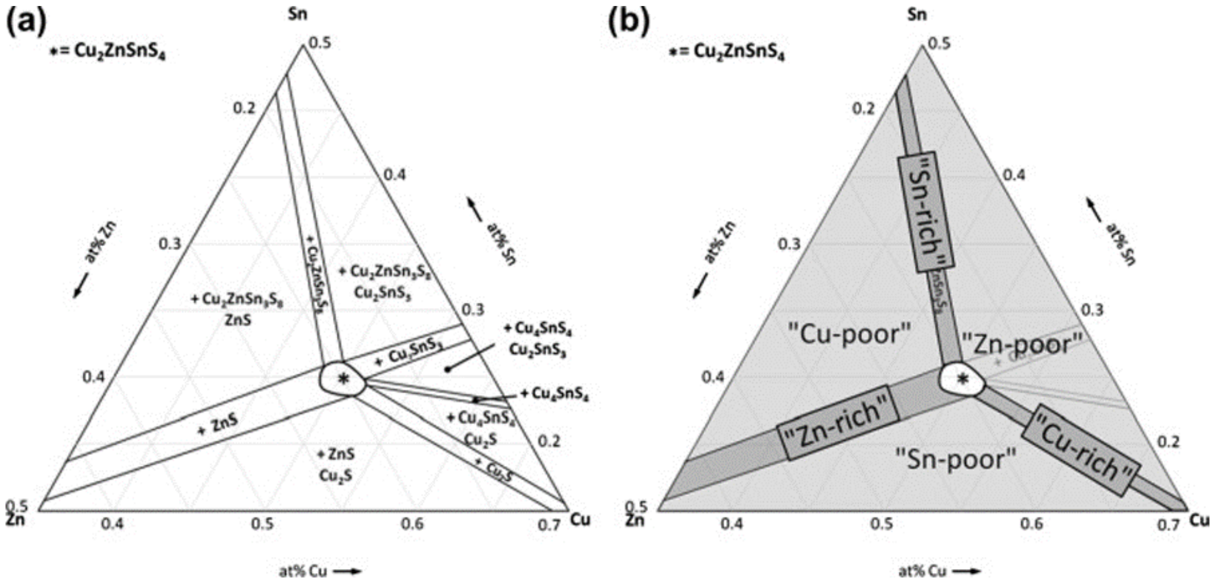

Fig. 1.4: Phase Diagram showing the possible region for the formation of pure CZTS phase [29].

1.2.2 Deposition of CZTS(Se) thin films

Despite the extensive research on CZTS over last two decades, there still exist key challenges in terms of ease of synthesis and achieving phase purity in CZTS films, compared to the more matured CIGS [31-33]. Firstly, owing to a narrow region of single phase CZTS in the Cu-Zn-Sn-S system, several secondary phases, suspected to arise from an initially non-optimized film composition which lies outside the region of single phase [34-36] and low enthalpy of formation [37], are reportedly formed spontaneously during the growth of the films [31-33] and hence, to synthesize single phase CZTS films reproducibly is very challenging. While a postdeposition heat treatment has been traditionally intended for the synthesis of phase pure films, potential loss of volatile (viz., Sn-based) compounds during the same poses additional difficulty in composition and phase control [38]. The presence of spurious phases arising as consequences of either poor composition control and/or decomposition at elevated annealing temperature detrimentally affects the performance of the devices, especially by limiting the open-circuit voltage and carrier life time [31-33, 39]. Consequently, finding an optimal, low-cost synthesis route having a better control over the composition and phase, while preserving the film quality has become a major challenge in the CZTS based device technology.

A variety of deposition techniques has been employed to prepare the CZTSSe thin films, such as thermal evaporation [40], sputtering [41], pulsed laser deposition [42], spray pyrolysis [43], nanoparticle or suspension printing [44], electrodeposition [45], solution based process [22-24,46-103], etc. The performance of the vacuum based physical deposition processes, which have yielded the highest efficiency for the CIGS-based device, has been poorer for the CZTSSe based devices [104]. Table 1.2 lists selected reports of photovoltaic performance of CZTSSe thin films grown by the solution based technique. So far, the highest conversion efficiency of 12.6% for any CZTSSe fabrication process has been obtained by the solution process in which the synthesized binary chalcogenides are then dispersed in hydrazine [15]. This hydrazine-based slurry is then used to deposit the CZTSSe films. However, the hydrazine is explosive, hepatotoxic [105] and carcinogenic [106]. Although the solution based processes have been traditionally considered to be the most economical way to fabricate thin films and can be upgraded for large-scale production on large area substrates, it is highly desirable that the process be free from high-toxic materials such as hydrazine and offer facile synthesis of the films.

Table 1.2: Selected reports on conversion efficiency (η) of CZTSSe thin films deposited by solution based process

Process Used	**η (%)**	**Year [Ref]**
Hydrazine Based Solution Method		
Hydrazine based solution process which involves a combination of solution- and nanoparticle-based deposition routes	9.6	2010 [22]
Cu, Zn and Sn solutions with hydrazine were prepared and sulfurized using a hot plate at the temperature of 540°C with S/S+Se = 0.4.	10.1	2011 [12]
Cu and Sn solution with hydrazine and Zn solution hydrazinocarboxylic acid were prepared. Annealing was done at 500°C under sulfur and selenium vapors.	8.08	2012 [53]
Absorber layer in a same way as [6] and the concentration of sulfur in the tube furnace was varied.	11.1	2013 [24]
Hydrazine based process as described by [6] with Cu/(Zn+Sn) = 0.8 and Zn/Sn = 1.1	12.6	2014 [15]
Non-Hydrazine Based Solution Method		
CZTS nanocrystals are synthesized by hot injection. After selenization CZTSSe is formed with Cu/(Zn+Sn) = 0.79 and Zn/Sn = 1.11	7.2	2010 [47]
Cu, Zn and Sn solution with 2 methoxyethanol, ammonium acetate and DI water with Cu/(Zn+Sn) = 0.87 and Zn/Sn = 1.15. Annealed in an N_2 +H_2S (5%) gas atmosphere for 1 hour at 500 °C.	1.61	2009 [54]
Ether solutions containing cationic salts and monoethanolamine (MEA) as stabilizer were spin coated with multiple layers. Annealed in Se atmosphere.	2.76	2012 [55]
Dimethyl sulfoxide as solvents;	4.1	2012 [49]
Economically founded precursors elements of ethanol-supported ink used for the preparation of layers of CZTS	5.14	2012 [56]

Cu, Zn, Sn and Ge precursor solutions were prepared and are mixed and then sulfur oleylamine was added at 225°C and CZTGeS nanocrystals were formed which were collected by centrifugation using hexane and ethanol.	8.4	2012 [57]
Adequate blending of binary and ternary nanoparticles results into ink are used for the preparation of CZTSSe thin coatings, succeeded by cooling with selenium.	8.5	2012 [58]
Cu, Zn and Sn precursor solution with carbon disulfide and butyldithiocarbamate were prepared. Films and selenium powders were then sealed under vacuum in a test tube followed by selenization at 540°C.	6.02	2013 [59]
The solution of precursors of Cu, Zn and Sn made up with water and ethanol, with ratio of fraction of Se and S (Se/Se+S) is 0.25, Cu,Zn and Sn (Cu/Zn+Sn) is 0.8, and Zn and Sn (Zn/Sn) is 1.28. for the decomposition of CZTS precursors and production of nanocrystals of sulfide, pre-annealing has been done at 250 °C using N_2 filled furnace, afterwards selenized has been done at 550°C for 30min with Se vapors.	6.2	2013 [60]
Dimethyl sulfoxide as solvents. Pre-annealing at 540 °C for 2.5 min was carried out followed by selenization at 540 °C for 20 min in presence of selenium.	8	2014 [62]
In 2-methoxyethanol copper (II) acetate monohydrate, zinc acetate dehydrate, stannous chloride dehydrate, and thiourea has been added to 2-methoxyethanol. The sol-gel method of thermal decomposition and reaction has been used for the production of CZTS thin coating.	5.1	2014 [63]
$Cu(CH_3COO)_2.H_2O$, $Zn(CH_3COO)_2.2H_2O$, $SnCl_2.2H_2O$ and $SC(NH_2)_2$ were dissolved in dimethyl sulfoxide which was diluted with acetone.	7.5	2014 [64]
Cu, Zn and Sn precursor solution with water and ethanol without any optimization process.	6.2	2014 [65]
Single component nanoparticle precursor of $Cu_{2-x}S$ nanoparticles capped with Zn-Sn complex was prepared. The precursor solution was spin-coated multiple times with intermediate annealing steps of 300 °C	1.2	2014 [66]
Precursor solution was prepared by dissolving $CuCl_2.H_2O$, $ZnCl_2$, $SnCl_2$ and thiourea in a mixture of deionized water and ethanol. This solution was spin coated followed by baking on a hot plate. Post sulfurization was done in a quartz tube furnace.	5.29	2014 [67]
The nano-paticulates of binary sulfide has been synthesized firstly, and finally deposited by spraying which is further followed by annealing Se atmosphere.	5.12	2014 [68]
Electrodeposition using a three electrode system. Electrolytic bath contained 4mM $CuSO_4$, 3mM $ZnSO_4$ and 3mM $SnSO_4$ without any complexing agent.	3.82	2014 [69]

For the preparation of nanocrystlas the adequate amount of copper acetylacetonate, zinc acetylacetonate hydrate, tin (IV) bis(acetylacetonate) dichloride has been blended in the solvent oleylamine. The condition for nanocrytals are such as performed in vaccum to 130 °C till 30 minutes. Then mixture is heated upto 225 °C in inert atmosphere provided by Ar. Further the Sulfur solution of 2M has been injected to the solution at same temperature which is put constant for 1 hour. After centrifuging nanocrystals has been obtained. These were dispersed in tolune and spin coated.	8.6	2014 [70]
The thin film prepared from the mixture of Cu, Zn and Sn and aqueous solutions of NaHS and NaHSe using the spin-coating technique which is afterwards then put on to heated substrates followed by selenization	8.6	2014 [71]
The mixture of Cu, Zn, Sn and Se in thioglycolic acid and ethanolamine gives a clear solution at 55 °C. Spin coated followed by sintering at 320 °C to get the film.	8.2	2015 [72]
The thin film prepared by mixture of $CuCl_2$, $SnCl_2$, $ZnCl_2$, thiourea, water and ethanol by spin-coating method. The deposited films (multiple times spin-coated followed by drying) were sulfurized.	3.95	2015 [73]
The homogeneous mixture of cation sources and elemental chalcogens in solvent primary amine and monothiol has been used to prepared thin film using the spin-coating technique, followed by drying at 250 °C and selenization at 500 °C.	7.86	2015 [74]
Firstly the CZTS layers were deposited in inert N_2 atmosphere, using spray which is non-pyrolytic of N_2 glove box, with 90% vol additive, water 10%vol, and ethanol as supported ink of ternery sulfide colloid composed of Cu–Zn–Sn. Afterwards the process has been done under Se atmosphere.	10.8	2015 [75]
Metal chlorides were dissolved in ethylene glycol monoethylether solution.	10.1	2017 [76]
Cu, Zn and Sn precursor solution were dissolved in DMSO to make ink. The N_2-filled glovebox has been used for ink-preparation and spin-coating. The concentration of O_2 and H_2O hs to be below 10 ppm.	10.7	2017 [77]

1.2.2.1 Solution process

Among various solution based approaches to prepare the CZTSSe thin films, three routes have been widely employed. In the first route, a layer of inks made up of CZTS nanocrystals is selenized to form CZTSSe [46]. This route has produced devices with 7.2% efficiency, when the elemental ratios were optimized [47]. It has been reported that it is easy to prepared nanocrystals by dispersion method, but the resulted coated material with ligands end up with carbon residues, which further reduces the efficiency of the solar cell [48]. In the 2nd route, pre-synthesized binary chalcogenides are dispersed in hydrazine and then this slurry was used to deposit the CZTSSe absorber layer directly. This route has yielded the highest efficiency i.e. 12.6 % for any CZTSSe fabrication process [15]. Using 3rd route for the preparation of nanocrystals, is much better. The homogeneous solution of CZTS precursor has been prepared, and then deposited. In comparison with first method and second method of preparation of nanocrystals, the third method is beneficial. The third method provides mixing at small molecular level scale and stochiometrically controlled precisely and no dependency on long-range diffusion.

Direct deposition of the homogeneous precursor solution via dip coating is one of the potential methods of fabrication of thin films of inorganic compound semiconductors. Surprisingly, compared to the other techniques, this process, which has been traditionally known for low cost, high throughput and large area deposition of uniform thin films, has drawn relatively low attention. This is most likely due to the fact that the deposited thin films are of thickness of order of 50-100 nm, thus requiring multiple coatings [78]. We believe that the advantages of the dip coating process far outweighs this inconvenience and hence, is chosen as the technique to grow the films in this work. In the followings, some of the studies on the films grown by this process have been highlighted.

Moriya et al., have obtained the coating of CZTS from the solution of $CuSO_4$, $ZnSO_4$, $SnSO_4$ and $Na_2S_2O_3$ using the photochemical reaction process [79]. Fischereder et al., depicted the idea of preparation of CZTS coating using pyridine based toxic solvent [80]. Wangperawong et al., used two techniques chemical bath deposition (CBD) and ion exchange consolidated, where the addition of Cu, Zn, Sn and S elements into the coating heaps has been done [81]. The CZTS absorb layer has been prepared with the sulfurized piles of film. Latter, Ki et al. and Choudhury et al., prepared coating of CZTS by mixing of Cu, Zn, Sn salts, and thiourea into dimethyl sulfoxide (DMSO) and methanol solvent respectively [49,50]. Mali˜ et al., prepared thin coatings using (SILAR) which is successive ionic layer adsorption and reaction. Where firstly the cationic and anionic precursors have been prepared separately, and substrate is dipped into them individually, and rinsing with liquid mainly water which is ion-exchanged [82]. The prepared coating efficiency is of 0.396%.

Afterwards by using same technique (SILAR), they increased the efficiency to 1.85% of CZTS based coating [83]. Shinde et al. used the same techniques and used the solution of CuCl, $ZnSO_4$ and $SnCl_4$ which is cationic in nature and thioacetamide (TAA) which is anionic in nature for the fabrication of the film [84]. They also reported the fabrication of CZTS film from CuCl, $ZnCl_2$, $SnCl_4$ and $Na_2S_2O_3$, those are all single precursor solutions [85]. However, they did not report any efficiency. Su˜ et al., used the improvised SILAR method for the fabrication of CZTS films. The coating prepared by glass/ZnS/Cu_2SnSx and glass/Cu_2SnSx/ZnS layers that undergoes the sulfurization process. SILAR method has been used for the fabrication of thin coating from precursor solution of ZnS and Cu_2SnS_3 and cation solution composed of $SnSO_4$ and $CuSO_4$, and NH_4F were added into the cation solution to avoid hydrolysis of Sn^{2+}. Both anion solutions contained $Na_2S{\cdot}9H_2O$ [86]. Gao et al. described another 3-step process to prepare CZTS films, which ensues with deposition of (Cu,Sn)S layer, an ioni-adsorption process, second step is ZnS layer CBD deposition, third step is the treatment with sulfur. However, the resulted coating are not of good quality. They shows bad quality of crystals with loosely held particles, and stoichiometric dependency [87]. Cao et al., synthesized CZTS films using CBD deposition method, which is a single step method and followed by cooling in S atmosphere. In this process, for the preparation of homogeneous solution of $CuSO_4.5H_2O$, $ZnCl_2.2H_2O$, $SnCl_2$, and deionized water, stirring is important. The stirring has been done for 5 to 8 minutes, which is afterwards followed by blending with urea, TAA, and sodium based chelating agent called Na_2EDTA into above mentioned solution. Lastly, pH has been altered by adding acid (HCl) or base (NaOH) into the solution [88]. They achieved the 0.30% efficiency. Liu et al. also reported the utilization of CBD method for the preparation of NR arrays from p-n junction hetro-structure of ZnO/CdS/CZTS. For the preparation of homogeneous solution of $Cu(CH_3COO)_2.H_2O$, $ZnCl_2$, $SnCl_2.H_2O$ and thiourea into solvent as DMSO, stirring is important. The prepared solution results into the CZTS solution. The substrate made up of sheath arrays of the ZnO/CdS core were used, for the deposition of layer. The substrate, for lesser time, was dipped into the above prepared solution, and cooling has been done under inert atmosphere of N_2 for 20 min at 420 °C [89]. Following their earlier report [86], Sun et al., reported the fabrication of coating of CZTS using the dip-coating method. They prepared solution from ethanol with metal complex as TAA and complexing agent as monoethanolamine (MEA). They found good solubility of all ingredients into the ethanol-MEA solvents and results into merging of molecular level has been shown into the solution of precursor. They have reported an efficiency of 5.36%, which is the highest for the dip-coating, chemical bath deposition (CBD) or SILAR method [52]. Kumar et al., reported the use of metal sulfates and sodium thiosulfate, for the fabrication of CZTS thin films, using the dip-coating method. They found that ammonia and TEA are important parameters for the film fabrication, otherwise no crystallization takes place [90]. Maheshwari and Kumar reported the use of metal chloride, thiourea, and ethylene glycol solvent, solution has been used for fabrication of CZTS thin film. They studied the cooling effect on film, which shows change in phase takes place from tetragonal to orthorhombic KS [91]. Subramanian et al. reported the use of metal nitrates, thiourea, and methanol solvent, solution for the manufacturing of CZTS based thin coating. For the prevention of precipitation, MEA has been used, which act as a stabilizer, and results into 1.34% efficiency [92]. Lately, Li et al., used CBD method for the fabrication of CZTS and CZTSSe based thin coatings. The annealing has been done in atmosphere of S and/or Se, for the progress of layers of precursors in the process [93]. The layers deposited on Mo-coated glass substrates in the rank of ZnS/Cu/SnS. The obtained efficiencies were 3.0% and 2.2%, for CZTSSe and CZTS supported thin coating respectively. The above survey shows that although direct deposition of precursor solution via dip coating offers a facile route of film fabrication, the performance of the devices have been poorer, which suggests a large scope for improvement and hence, is of research interest.

1.2.2.2 Challenges in fabrication of device grade CZTS films

Considering the explosive, hepatotoxic [105] and carcinogenic [106] nature of hydrazine, there have been wider research on facile synthesis of CZTS films from non-toxic solutions. Several non-hydrazine solutions such as dimethyl sulfoxide (DMSO) [49], pyridine [81], ethylene glycol, ethanol [52, 55, 94-97], methanol, [49,50] etc. have been studied, which are much safer to employ; however, these have not yielded such high PCE, thus suggesting a larger scope of research.

While global efforts are on to grow these films in solution based approaches from non-toxic chemicals, no consensus on protocols to suppress the unwanted secondary phases and to promote the formation of single phase CZTS has been developed yet. Ironically, the formation of single kesterite phase with better control over secondary phases has been the key to its success in photovoltaic applications. In all solution based approaches for semiconductor thin films, the film growth proceeds from the release of cations and anions from the precursor salts, and their subsequent reactions. The reaction pathway depends on various process parameters (such as temperature, precursor composition, deposition duration, complexing agent, etc.) and determines the eventual microstructure and phase of the films [52,95]. During the growth of inorganic semiconductor thin films from solutions, complexing agents are associated with maneuvering the release rate of ions and the reaction the kinetics [55]. Hence, prior comparative study of the use of complexing agents and/or their concentration forms a key component in that it can provide detailed insight to the understanding of film growth. In literature, although one can find the use of a number of complexing agents in solution processed CZTS films, [49,52,80,95-97] such a study elucidating its role in obtaining phase pure crystalline CZTS is not available and forms a key component of this thesis.

Another important aspect of growth of CZTS thin films that this thesis attempt to address is the post-deposition high temperature annealing (HTA) configuration. In most of the

CZTS thin film synthesis approaches, phase pure films with large grain size has been obtained by utilizing a two-step process viz. deposition of a precursor film followed by high temperature annealing (HTA) in a chalcogen environment [98-103]. The HTA is understood to have a vital role in the evolution of the kesterite phase of the films as well as in the growth of large grains [107,108]. However, the HTA process parameters, namely, the temperature, duration and sulfur vapor pressure are required to be delicately controlled, as evidenced from the reports of evolution of spurious phases and potential loss of volatile (viz., Sn-based) compounds as a consequence of HTA at conditions even marginally different from the optimum one [37,109-111]. For instance, decreasing the sulfur partial pressure during the HTA results in the decomposition of CZTS as given in reaction 1, driven by the change in the oxidation state of Sn from +4 to +2 [112].

$$Cu_2ZnSnS_4\ (s) \Leftrightarrow Cu_2S\ (s) + ZnS\ (s) + SnS\ (s) + \tfrac{1}{2} S_2\ (g);\ SnS\ (s) \Leftrightarrow SnS\ (g) \quad (1.1)$$

On the other hand, prolonged annealing often results in growth of a thicker MoS_2 layer at the CZTS/Mo back contact interface that may increase the back resistance [113,114]. Furthermore, in view of the growing interest in replacing the toxic H_2S gas by solid sulfur as a source of sulfur vapor [115-118], simultaneous optimization of sulfur source temperature (which in turn controls the sulfur pressure in the annealing chamber), reaction temperature and the annealing duration has become very important [116,119-121]. Especially for the solution processing of the thin films, the HTA parameters assume greater significance in view of the role of HTA in weakening of bonds in the organic-inorganic complexes in the precursor film followed by reactions and phase transformation of intermediate solid state binary and tertiary compounds to yield the eventual CZTS thin films [114-121]. Correspondingly, the optimized HTA process control has become critical for obtaining solution-processed films of desired properties. As an important step of processing, many groups have utilized different HTA settings and parameters, which however have produced considerable variation in the properties of the resulting films [116,119-121], most likely due to the variation in the chalcogen vapor flux reaching the reacting surface (i.e., the precursor film) [35,37,112]. While, a HTA strategy that is simpler and avoids overly-critical configurations is highly preferred, it is necessary to ascertain the influencing mechanisms of the same and rationalize the growth patterns for reliable reproduction of the CZTS films.

Another critical factor that affects the efficiency of the devices is the incorporation of Se in CZTS. Selenium alloying with CZTS (i.e., the formation of CZTSSe) has been found to lower V_{oc} deficit (i.e., $E_g/q - V_{oc}$) and helps in obtaining higher efficiency [122]. The pure selenide compound (CZTSe) has a lower bandgap of ~1 eV than the bandgap of pure sulfide compound (1.5 eV for CZTS). Despite the decrease in the bandgap, the V_{oc} deficit decreases in CZTSSe than that of CZTS, most likely due to the reduction in defect density acting as recombination centers due to selenium in the matrix. The ratio of Se/(S+Se) exhibits a significant impact on the electronic characteristics of the device such as open circuit voltage (V_{oc}), short circuit current density (J_{sc}) and also the power conversion efficiency of CZTSSe films. Thus, a systematic study of Se inclusion - that can impact the device performance - as a consequence of modification of process parameters is of high interest.

1.3 MOTIVATION AND OBJECTIVES

Following the preceding sections, it appears that combined with a non-toxic solution, dip coating can be a very promising method for growing the CZTSSe thin films. In this work, it is proposed to exploit the versatility of the dip coating method and the advantages of non-toxic homogeneous precursor solutions. Process parameters can be tuned to prepare films of potential photovoltaic characteristics. As mentioned before, complexing agents play an important role in the growth of inorganic semiconductor thin films. Secondly, during solution processing, the HTA is understood to have a vital role in evolution of the kesterite phase of the films as well as in the growth of large grains. However, the HTA process parameters, namely, the temperature, duration and sulfur vapor pressure are required to be delicately controlled, as evidenced from the reports of evolution of spurious phases and potential loss of volatile (viz., Sn-based) compounds as a consequence of HTA at conditions even marginally different from the optimum one. Lastly, a systematic study of Se inclusion - that can impact the device performance - as a consequence of modification of process parameters is of high interest.

In view of this, a prior comparative study of the use of complexing agent, HTA configuration and post-selenization assume importance in that such an investigation can provide critical insight to the understanding of growth of phase pure CZTSSe thin films.

Objectives

The main objectives are the followings:

1. Growth of CZTS thin films by non-hydrazine solution based process. The composition, post-deposition heat treatment temperature and duration will be optimized to obtain thin films suitable for photovoltaic application.
2. Identification of the set of process parameters those yield films suitable for photovoltaic application.

3. Investigation of the effects of selenium alloying in CZTS on the properties of resulting films.

1.4 OUTLINE OF THE THESIS

Chapter 1 points out the growing energy needs due to the scarcity of fossil fuels and figures out that photovoltaics has emerged as a key alternative energy technology that promises to mitigate the energy crisis to a significant extent. We identify the routes to reduce the cost, which can be achieved through better materials management, development of inexpensive production processes and new techniques to enhance the existing solar cell efficiencies using materials in the form of thin films and illustrates the importance and various properties of CZTS thin films. It highlights the key challenges in the fabrication of CZTS films and its impact on solar cells. This chapter provides the advantages of solution based (non-toxic, hydrazine free) approach along with the detailed survey from the literature which supports and provides the path to achieve the objectives.

Chapter 2 includes the experimental techniques used for the preparation of CZTS and CZTSSe thin films, and the other layers namely Mo, CdS, ZnO, ZnO: Al and Al films to complete the solar cells. This chapter also contains details of the various techniques used for the characterization of these layers.

Chapter 3 reports the growth and characterization of CdS thin films from ammonia-free chemical bath deposition (CBD) method. The role of bath temperature and scaling of surface roughness have been investigated. The study of evolving surfaces provides insight to the fundamental growth dynamics and enables one to control the roughness of the films. Such a study is of high technological relevance in that roughness of thin films in multilayer structures affects electrical, optical, mechanical and catalytic properties, and hence, determines the eventual performance of devices. The results of this chapter suggested the optimized condition for the growth of CdS thin film that can be used as n-type buffer layer in thin film solar cells.

Chapter 4 demonstrates the role of complexing agent in eliminating secondary phases during the growth of CZTS films from an ethanol based solution. By studying the films grown from solutions with and without the complexing agent, monoethanolamine (MEA), it is found that the absence of the complexing agent enhances the release rate of Cu^+ that is reduced from Cu^{2+}, which is crucial to the evolution of single phase. It elucidates the reaction mechanisms in transformation from precursor solution to CZTS phase via intermediate solid state binary and ternary compounds during deposition and the subsequent sulfurization treatment in the ethanol based solution process. The reaction pathway is demonstrated to be different to the other liquid based methods that requires dispersing agents to suspend nano- or micro-scale particles at elevated temperature.

Chapter 5 highlights the vital role of HTA in the evolution of the kesterite phase of the films as well as in the growth of large grains. Hence, the impact of HTA configuration including systematic variations in the ramp rate, sulfur source temperature and the reaction temperature is exhibited here and we proposed a strategy for facile synthesis of phase-pure kesterite CZTS thin films from environment-friendly ethanol based solutions by direct deposition of the solution via dip coating. The results elucidate the critical dependence of the HTA setting, in particular of the sulfur vapor flux, on the phase evolution of the films and highlight the promise of the approach including the proposed HTA strategy for reproducible growth of phase pure kesterite CZTS films.

Chapter 6 illustrates the role of precursor concentration and annealing temperature on the evolution of film to obtain micron-thick single phase, conformally coated large grained CZTS thin films. It elaborates that the efforts for conformal deposition of micrometer thick phase-pure CZTS films from ethanol based solutions via dip-coating with minimum process steps. We show how by intuitively manipulating the starting molar concentration of the cationic and anionic solutions and the sulfurization ambience (sulfur partial pressure, duration and temperature), thicker kesterite CZTS films can be obtained with just two dipping cycles. The results indicate the promise of the approach for facile growth of good quality films with high photosensitivity.

Chapter 7 deals with the systematic study of Se inclusion - that can impact the device performance - as a consequence of modification of process parameters. It is demonstrated that the Se/S+Se ratio can be tuned by manipulating the selenization conditions (such as, duration of selenization, the amount of Se during the selenization process, etc.) which affects the phase and other properties of the CZTSSe thin films. This chapter also contains some of the preliminary results on the device performance.

Chapter 8 summarizes the work carried out. It also discusses scope for future work.

CHAPTER – 2

EXPERIMENTAL DETAILS

This chapter contains the experimental techniques used for the preparation of CZTS and CZTSSe thin films, and the other layers namely Mo, CdS, ZnO, ZnO:Al and Al films to complete the solar cell structure. This chapter also contains details of the various techniques used for the characterization of these layers.

2.1. DEPOSITION OF CdS THIN FILMS

Thin films of CdS – an n-type semiconductor – has been routinely used as the window layer in the CZTS based solar cells. Although a variety of techniques has been used, chemical bath deposited (CBD) CdS films have been the most popular choice for solar cell application. It is one of the simplest and low cost solution based technique for preparing large area films, which makes it attractive for the photovoltaic industry. Most of the techniques reported in the literature to grow the CdS films by the CBD process are based on a system of a cd salt, ammonia and thiourea [123]. In view of toxicity of ammonia, many groups have grown the CdS thin films from bath solutions free from toxic ammonia, which reduces the overall toxicity in fabricating cost effective photovoltaic devices.

In this work, attempts were made to deposit CdS films from non-toxic ammonia-free solutions by the CBD process. The precursor solution was prepared by adding 25 ml of 0.1 M cadmium chloride (Loba Chemie, India, 99.0%), 20 ml of 1 M sodium citrate (Loba Chemie, India, 98.0%), 5 ml of 1 M potassium hydroxide (Loba Chemie, India, 85.0%) and 20 ml of buffer (NaOH) pH = 10 (Loba Chemie, India, 98.0%) sequentially in a beaker. The DI water was added in the solution to complete a total volume of 90 ml. The films were prepared at different bath temperatures in the range of 40 – 80 °C. The bath temperature was increased from room temperature and after reaching the bath temperature, 10 ml of 1 M thiourea (Loba Chemie, India, 99.0%) was added. A cleaned glass substrate was kept vertical in the beaker containing the bath solution. After the deposition, the films were taken out of the bath and the loosely adhered particles present on the films was removed by washing ultrasonically in DI water and finally dried in air. The schematic diagram of deposition process is shown in fig. 2.1.

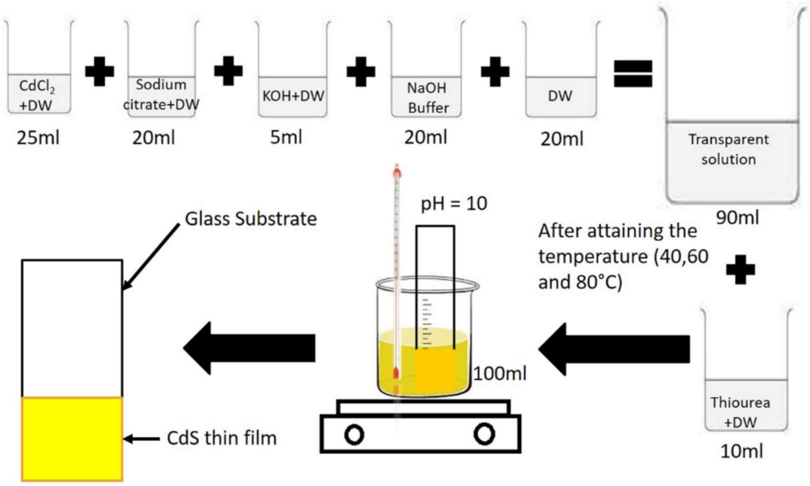

Fig. 2.1: Schematic diagram to illustrate various steps used for the deposition of CdS thin films.

2.2 DEPOSITION OF CZTS AND CZTSSe THIN FILMS

As discussed in Chapter 1 (Section 1.2.2.1 and 1.2.2.2), among various deposition techniques used to grow the CZTS based thin films, direct deposition of homogeneous non-hydrazine non-toxic precursor solutions via dip coating method can be a viable scalable approach for the growth of these films. In this work, ethanol based cationic and anionic precursor solutions were used to deposit the films. The typical precursor solution was prepared by mixing separately prepared cationic (Cu, Zn and Sn) and anionic (S) solutions under constant magnetic stirring. Firstly, solutions of $CuCl_2$ (99%+, Alfa Aesar), $ZnCl_2$ (99.99%, Alfa Aesar), $SnCl_2 \cdot 2H_2O$ (98%, Alfa Aesar) and Thioacetamide (TAA) (99%+, Spectrochem) in ethanol were prepared separately under constant magnetic stirring at room temperature until the solid salts were completely dissolved. The composition of $CuCl_2$ was varied from 0.25M to 1M and composition of other chemicals was changed keeping the ratios of Cu: (Zn+Sn) =1.00 and Zn:Sn = 1.05. In some cases, a complexing agent monoethanol amine (MEA) of various concentrations were used, and its effect was studied in detail as given in Chapter 4. We have found that acceptable results in terms of the formation of single phase CZTS were obtained when no MEA was used. For investigating the role of MEA, to every 10 ml of cationic solution, 10 ml of MEA solution (of varied concentrations) was added making each cationic solution of 20 ml. The $ZnCl_2$ and $SnCl_2$ solutions were added to the $CuCl_2$ solution sequentially with constant magnetic stirring and then the temperature was increased to 60 °C from room temperature. All the preparations were performed in air.

The precursor thin films were prepared by dip-coating from the above prepared precursor solution. Films were deposited onto sodalime glass substrates. The substrates were cleaned ultrasonically in DI water and isopropanol bath. The cleaned glass slide was vertically dipped in the precursor solution, following which the anionic solution (TAA solution) was added and continuously stirred for 60 min. The film was then dried at 130 °C for 10 min and a black colored appearance was observed. The thus-prepared precursor films on the substrates were then annealed in a tube furnace with different high temperature annealing (HTA) settings in S and/or Se atmosphere, as detailed in Chapter 5 and 7. The schematic diagram of the synthesis process is shown in fig. 2.2.

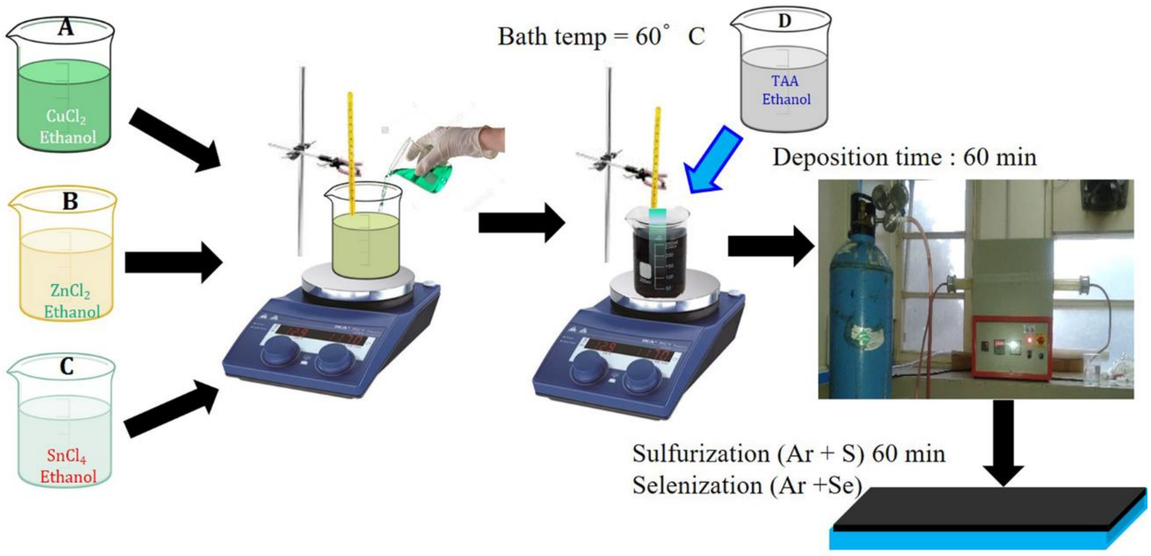

Fig. 2.2: Schematic diagram to illustrate various steps used for the deposition of CZTS(Se) thin films.

2.3 DEPOSITION OF Mo THIN FILMS

Molybdenum (Mo) thin films have been routinely used as the back contact to collect and move holes out of the cell [124-126]. Traditionally, sputter deposition has been used to grow Mo thin films [127-129]. It has been observed that the deposition at a high pressure produces films with an excellent adhesion, but the resistivity was relatively high primarily due to micro-cracks in the films, whereas the deposition at a low pressure yields films with lower resistivity and very poor adhesion [127,129]. Hence, deposition of a bilayer - first using high pressure followed by deposition at low pressure - has been used to take advantage of both pressure regimes.

DC magnetron sputtering was used to deposit Mo films on to SLG substrates where a water-cooled 2-inch target (99.99%, Tredmann Pvt. Ltd., Taiwan) held at room temperature was used. The substrate was rotated about its axis at the rate of 8 rpm. The centers of substrate and target was kept at about 10 cm away from each other. A rotary pump followed by turbo molecular pump was used to evacuate the chamber (base pressure lower than 5.0×10^{-6} mbar). DC power of 150 W was used for Mo bilayer deposition and Ar pressure was maintained at first 2.6×10^{-2} mbar (high pressure deposition, HPD) for 10 min followed by 2.6×10^{-3} mbar (low pressure deposition, LPD) for 20 min. The Ar flow in the chamber was controlled with the help of mass flow controller at 30 standard cubic centimeter per minute (SCCM) and the throttle valve was adjusted to maintain the sputter pressure.

2.4 DEPOSITION OF ZnO AND ZnO:Al THIN FILMS

High resistive high transparent ZnO and low resistive high transparent ZnO:Al thin films have been established as optimal window layers in the CZTS based solar cells. The main purpose of these window layers is to reduce the effect of pin-holes in the buffer layer which could provide a connection between the absorber layer and the top contact layer.

RF magnetron sputtering was used to deposit ZnO films on to SLG substrates where a water-cooled 2-inch target (99.99%, Tredmann Pvt. Ltd., Taiwan) held at room temperature was used. The substrate was rotated about its axis at the rate of 16 rpm. The centers of substrate and target was kept at about 5 cm away from each other. A rotary pump followed by turbo molecular pump was used to evacuate the chamber (base pressure lower than 4.0×10^{-6} mbar). RF power of 100 W was used for the ZnO layer deposition and Ar pressure was maintained at 5.0×10^{-3} mbar for 20 min. The Ar flow in the chamber was controlled with the help of mass flow controller at 95 standard cubic centimeter per minute (SCCM) and the throttle valve was adjusted to maintain the sputter pressure.

The Al-ZnO films were deposited by RF magnetron sputtering using in house prepared target of 2-inch diameter held at room temperature. The sputter configuration was similar to the one used for the growth of the ZnO layers. RF power of 100 W was used for the deposition and Ar pressure of around 1.5×10^{-3} mbar was maintained for 60 min. The Ar flow in the chamber was controlled with the help of mass flow controller at 20 standard cubic centimeter per minute (SCCM) and the throttle valve was adjusted to maintain the sputter pressure.

2.5 DEPOSITION OF Al FILMS

A grid of Al is most widely used as the top electrode of the cell. This must balance in collecting numerous carriers from the ZnO layer as possible with covering as little portion of the cell area as possible, as this shading limits the area that can absorb sunlight. Aluminum grid of area 25 mm^2 (separation between the grid was ~1 mm) were grown by thermal evaporation using shadow masks at a base pressure of 5×10^{-6} mbar in a vacuum chamber.

2.6 CHARACTERIZATION TECHNIQUES

Various techniques were used to characterize the films for the determination of phase, microstructure, optical and electrical properties. This section briefly describes the various techniques used.

2.6.1 X-Ray Diffraction (XRD) measurements

The crystal structure of solid sample is widely determined by X-ray diffraction technique. A PanAlytical X-Ray diffractometer using Cu-Kα radiations was employed in the present work. Debye-Scherrer equation given below is extensively used for the determination of crystallites of the films.

$$D_{hkl} = \frac{0.9\lambda}{\beta Cos\theta} \qquad (2.1)$$

where crystallite size is represented by D_{hkl} is, X-rays wavelength is represented by λ, FWHM is full width at half maxima represented by β is which is calculated by Lorentzian fitting to the diffraction peaks in the XRD patterns, and Braggs's angle is represented by 2θ.

However, the analogy is obtained between crystal structure of ZnS (JCPDS: 00-05-0566) and Cu_2SnS_3 (JCPDS: 00-027-0198) with kesterite structure CZTS (JCPDS: 026-0575), interpretation of phase purity of the samples based on the XRD patterns has been found to be incomplete. In most cases, XRD is accompanied with Raman measurements for the correct and complete analysis of the different phases of coating.

2.6.2 Raman Spectroscopy

Raman spectroscopy, is a molecular spectroscopy, which depends on change in polarizability within a sample. Its operational principle relies on the coupling of the incident light with the vibrating modes of the crystal lattice or phonons. When the sample is irradiated by monochromatic light, the photons are absorbed and then reemitted with a shifted frequency called Raman Shifts. The Raman shifts exhibits the rotational and vibrational frequency information of the molecules of samples. The frequency changes from phase to phase which is easily detected by the Raman spectroscopy. The energy shift is the characteristic of the vibrating chemical bonds in a material, and can be used to identify the material. For this work, the Renishaw Raman microscope system with 514 nm wavelength of lase has been used for the phase purity.

2.6.3 X-Ray Photoelectron Spectroscopy (XPS)

X-Ray photoelectron spectroscopy is a versatile technique, which is also known as ESCA (Electron Spectroscopy for Chemical Analysis). It provides surface layer information of the thin films and its chemical environment. The chemical bonding of elements can be differentiated which makes it a unique surface characterization technique. The basic principle of operation is by irradiation of atoms of samples by photons caused ejection of electrons. When a sample irradiated with X-ray photon of sufficient energy, it will knock out the electron. The kinetic energy (KE) of released electron is related to binding energy (BE) by equation

$$KE = h\nu - BE - \O_s \tag{2.2}$$

where, photons energy is expressed by $h\nu$ and work function is expressed by $\O_s$. The kinetic energy of electrons vs binding energy has been plotted using above equation. The graph is in the form of peaks, which have to be analyzed. The peaks depicts about the amount of electrons at certain binding energy which is a characteristics of elements present in samples.

The XPS measurements were carried out using the PHI 5000 VersaProbe III (Physical Electronics) system with Al K_α excitation source. XPS measurements of some of the samples were also carried out by a SPECS spectrophotometer (Surface Nano Analysis GmbH) using Al K_α radiation. The C 1s line at 284.6 eV has been used as reference for core levels binding energy.

2.6.4 Scanning Electron Microscopy (SEM)

The surface morphology of thin film has been studied with SEM. The SEM technology is powerful tool for the surface analysis of thin film. The basic principal of SEM and microscopy is similar, with the basic difference of photons used in SEM, whereas in microscopy light is used. SEM technology produces highly magnified images, with intense penetration of photons. When a focused beam of electrons with energy 10-30 keV is incident on sample surface, three basic electrons ejected from the surface, that is secondary electrons, backscattered electrons and X-rays. Secondary electrons are generated because of the inelastic interactions between incident photons and sample electrons and an elastic interaction is the main cause for the production of backscattered electrons. The qualitative and quantitative chemical information is provided by XRD. Field emission scanning electron microscopy (FESEM) (Hitachi SU8000) has been used for the surface morphology of film. Energy dispersive X-ray spectroscopy (EDS) (Brukers XFLASH 6130) has been for elemental composition of samples. The thickness of the samples was estimated from the cross sectional FESEM images.

2.6.5 Atomic Force Microscopy (AFM)

Figure 2.3 represents conventional diagram for the set up of AFM. AFM did the surface microscopy, with accessorized with flexible cantilever at the end, and sharp tip called probe. This sharp tipped probe analyzed the surface morphology of sample and signals collected by cantilever, which is further send to receiver. The cantilever movement is because of the interaction force between probe and surface atoms of sample. The detector receive the signals, send by centiliver, is made up of 4- quadrant photodiode. The AFM produces the 3 dimensions images of the sample surface. The piezoelectric scanner has been used for scanning in three directions, i.e. x, y, and z directions and framed the scanned images.

Atomic force microscopy (AFM) has been used for the detailed study of surface morphology of the film with the help of NT-MDT-NTEGRA PRIMA system. The images were acquired in air at room temperature in tapping mode of operation. It has been reported that consistent images results were obtained by scanning the surface of samples at four different points.

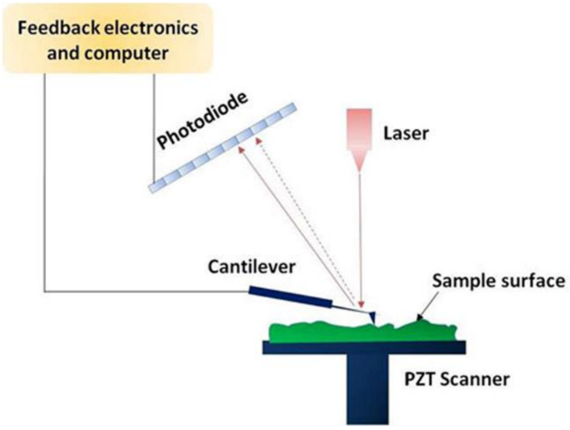

Fig. 2.3: Schematic of an AFM setup [130]

2.6.6 UV-Vis Spectroscopy

UV-Vis-NIR spectrometer was used to directly measure the reflectance and transmittance spectra of the thin films. The optical absorption coefficient α was estimated using the formula

$$\alpha = \frac{1}{d} \ln \left[\frac{(1-R)^2}{T}\right] \tag{2.3}$$

for the film of thickness d. The optical bandgap of the films can be determined from Tauc plot given in the equation

$$\alpha h\nu = A\,(\alpha h\nu - E_g)^m \tag{2.4}$$

where A is a constant, $h\nu$ is the incident photon energy and m defines the nature of the optical transition and can take values of 1/2, 3/2, or 2 for direct-allowed, direct-forbidden, and indirect-allowed transitions, respectively. The optical bandgap energy is obtained by considering a direct-allowed transition for CZTS (m = 1/2) and reading the intercept of the extended linear part of the $(\alpha h\nu)^2$ vs. $h\nu$ plot with the abscissa. Reflection and transmission measurements were done using a Shimadzu UV3600 spectrophotometer equipped with a 150 mm integrating sphere.

2.6.7 Electrical Properties

2.6.7.1 *I-V* Measurements

Current-voltage (*I-V*) measurements were done to estimate the solar cell electrical parameters. These were performed in a system that measures current and voltage. It uses a tungsten-halogen lamp to simulate the Sun’s light. The diode is then illuminated and the current is measured by varying the applied voltage, which gives the IV-curve. Additionally, the measurement was performed in dark as well. This gives us further insights about the diode characteristics. The voltage-current measurements were recorded with a Keithley 2400 source meter. For the photoresponse measurements, the light intensity was standardized to 100 mW cm^{-2} by using a Newport optical power meter.

2.6.7.2 Hall Measurements

Electrical resistivity of the samples was measured by the van der Pauw method. The voltage-current measurements were recorded with a Keithley 2400 source meter. For the Hall measurements, an in-house assembled system was used. The sample was attached with wires and was placed between the pole pieces of the electromagnets. A Gauss meter was used to measure the magnetic field. A Keithley 2400 source meter was used to the current and voltage measurement. In this method, four wires along with ammeter and voltmeter were attached to the sample as shown in the Fig.2.4a.

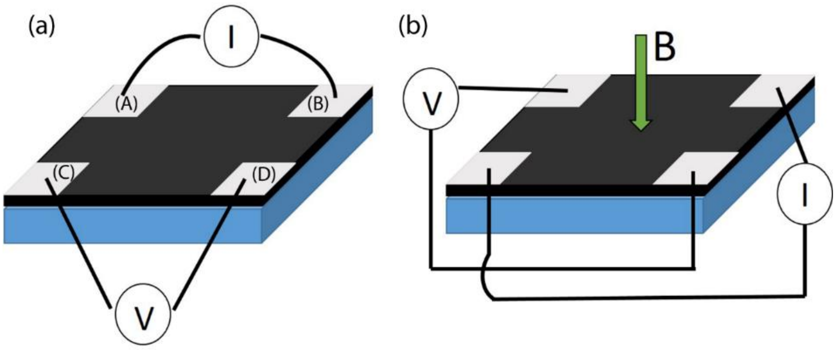

Fig. 2.4: Electrical characterization of samples using van der Pauw method for (a) resistivity and (b) Hall coefficient

The details of the procedure to calculate the resistivity of thin film samples are given explicitly elsewhere [131].

Hall measurements are done when ammeter and voltmeter are attached diagonally as shown in fig. 2.4b. The sample is then placed in the magnetic field. When the current is passed through the sample, the voltage drop is generated according to the equation:

$$\vec{\boldsymbol{E}} = q(\vec{\boldsymbol{v}} \times \vec{\boldsymbol{B}}) \tag{2.11}$$

where, E is electric field, q is the charge of electron, v is the velocity of the electron and B is the magnetic field. The Hall measurements were carried out using an in-house designed setup with a magnetic field strength of 0.23 T. The carrier concentration and mobility is then calculated using equations:

$$n = \frac{1}{qR_H} \;\; \& \;\; \mu = \frac{R_H}{\rho} \tag{2.12}$$

where, n is carrier concentration, R_H is Hall coefficient and μ is the mobility of the thin film. Hall coefficient can be calculated by:

$$R_H = \frac{tV_H}{HI_H} \tag{2.15}$$

where, V_H is the Hall voltage and I_H is the Hall current.

CHAPTER – 3

GROWTH AND CHARACTERIZATION OF CdS THIN FILMS

CdS, an II-VI compound semiconductor, has been widely studied owing to its optoelectronic properties suitable for a wide range of applications including infrared devices, electro-optic devices, photo detectors, photo catalysis etc. [132-134]. In recent years, the interest in CdS has deepened due to its proved suitability in the CZTS based heterojunction solar cells.

As mentioned in the experimental section, chemical bath deposition (CBD) technique offers a very simple and cost competitive approach for growth of CdS films on large area substrates. Moreover, CBD CdS films have been proven very beneficial in the CZTS based solar cells. In the CBD process, however, the properties of the films are strongly influenced by the bath temperature, composition of the precursor solution, pH of the solution and deposition time. Very few work has been done on the bath temperature dependent properties of CdS thin films grown from ammonia-free solutions and forms the basis of this chapter. In this work, the CdS films were prepared from ammonia-free solutions by the CBD process at bath temperatures of 40, 60 and 80 °C and the properties of the resulting films were investigated.

3.1 BATH TEMPERATURE DEPENDENT GROWTH RATE

The variation of film thickness as a function of deposition time at 40°, 60° and 80°C is presented in Fig. 3.1. As expected, the film thickness increased with the deposition time. At low temperature of 40 °C, thickness increases linearly for a deposition time as high as 180 min. However, the thickness tends to saturate early (~60 min) for the higher deposition temperatures. The decrease in the growth rate with increase in the deposition time is assigned to the depletion of Cd and S ions in the solution. Further, the increase in deposition rate with increase in the bath temperature suggests the enhancement of growth kinetics involved in the reaction.

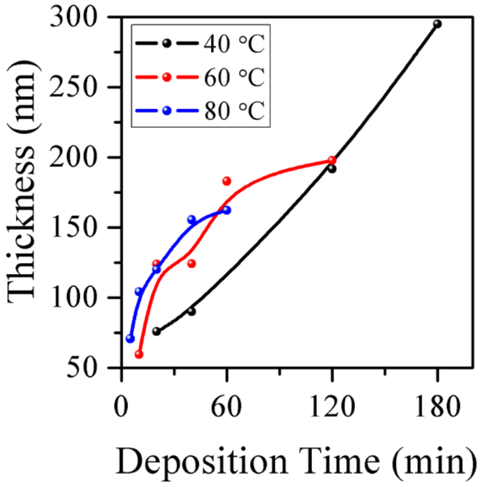

Fig. 3.1: Variation of film thickness with deposition time for films grown at a bath temperature of 40, 60 and 80 °C.

3.2 STRUCTURAL CHARACTERIZATION

Typical XRD patterns of the CDS thin films grown for different thickness at bath temperatures of 40, 60 and 80 °C are shown in Fig. 3.2. At initial stages of film growth, the films are amorphous and as the thickness increased, a lone peak at about 26.7° appeared, intensity of which increased with thickness. The peak was identified as (002) diffraction peak of hexagonal CdS phase, in accordance with JCPD card 00-041-1049. Lorentzian fitting to the diffraction peak in the XRD patterns was carried out to determine quantitative variation of peak width and peak height as a function of thickness for different bath temperatures. As shown in Fig. 3.3, the peak width monotonically decreased with the thickness for the films deposited at 40 and 60 °C. However, for the 80 °C deposition, the peak width decreased rapidly up to a thickness of 150 nm and marginally increased thereafter. On the other hand, the peak height continuously increased for the films deposited at 40 °C, suggesting increasing crystallinity of the films due to increasing thickness. However, for the films grown at 60 °C, the peak height increased and then saturated, whereas for that at 80 °C, the peak height decreased for larger thickness. The results suggest that the thickness increased very rapidly at higher bath temperatures and the structural quality of the films decreased, as evidenced from the increased peak width and decreased peak intensity for the films grown at 80 °C. It may be noted that the thickness of the CdS layer is required to be in the range of 40 - 60 nm for CZTS thin film solar cells. Considering the slow deposition rate and hence better control, deposition at 40 °C is believed to be suitable for solar cell applications and hence, considered further [135].

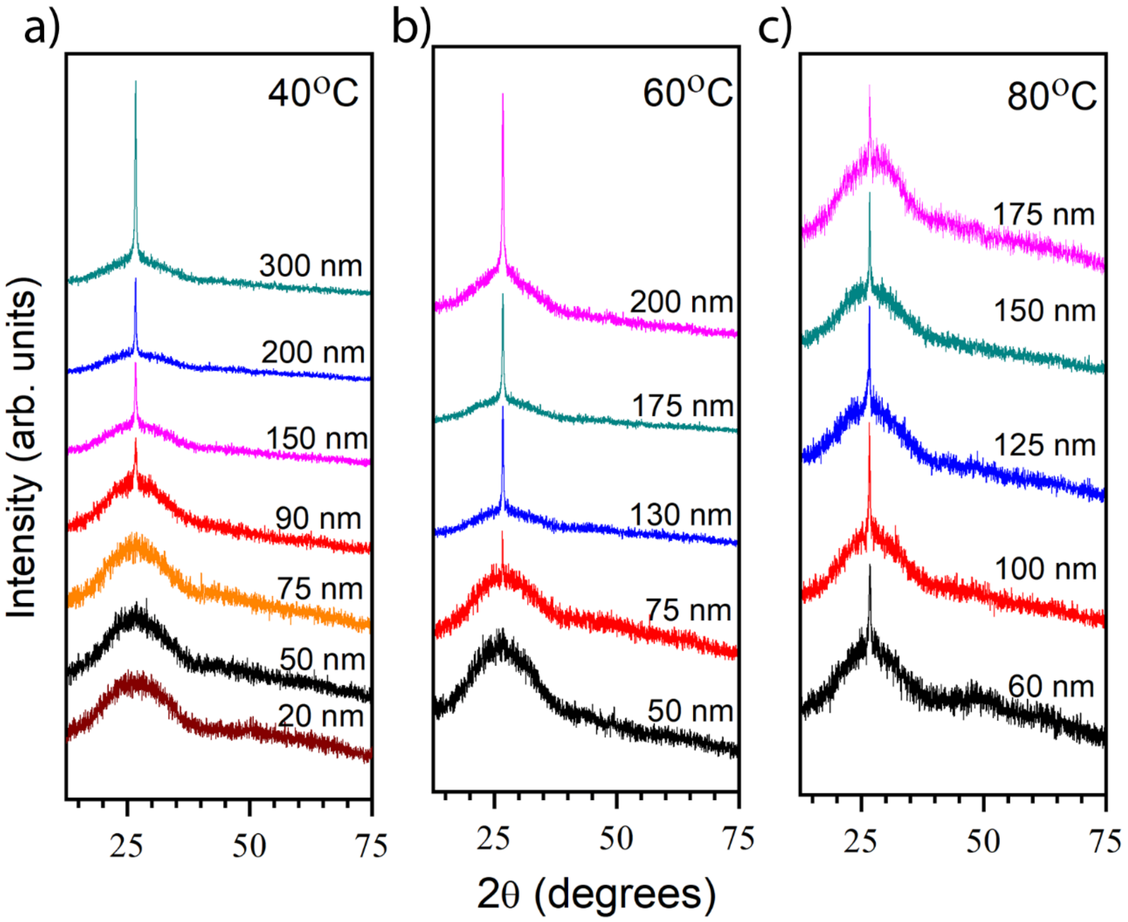

Fig. 3.2: Typical XRD patterns of the CdS thin films grown at bath temperature of (a) 40, (b) 60 and (c) 80 °C.

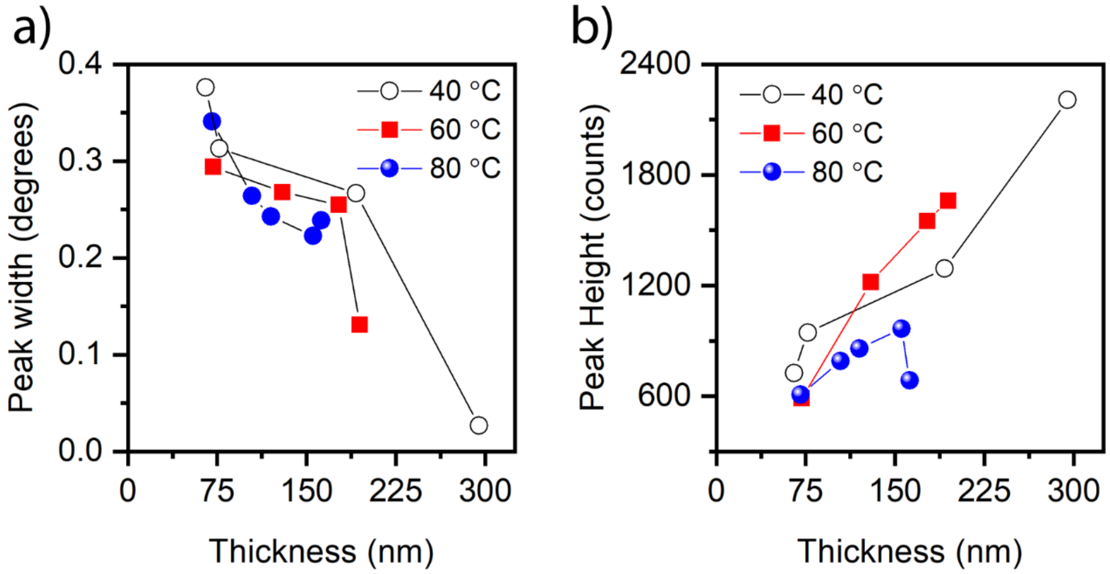

Fig. 3.3: Variation of the (a) peak width and (b) peak height of the (002) peak of the XRD patterns of the CdS thin films grown at bath temperature of (a) 40, (b) 60 and (c) 80 °C.

3.3 SURFACE MICROSTRUCTURE

The evolution of surface morphology of the films grown at 40, 60 and 80 °C is depicted in fig. 3.4. The corresponding cross-sectional FESEM images are given below. With increase in bath temperature, the uniformity of the surface of the films relatively increases. The amount of CdS particulates on the film surface decreased as the temperature was increased. Insets in the figure show that the thickness of the films increased with deposition time, consistent with the XRD results. It may be noted that the analysis of the grain size from the XRD peaks and that from the FESEM images yielded different results. For example, for the CdS films grown at 40 °C with a deposition time of about 60 min, calculations revealed a grain size of 30 nm from XRD while that from FESEM images was found to be of 100 nm.

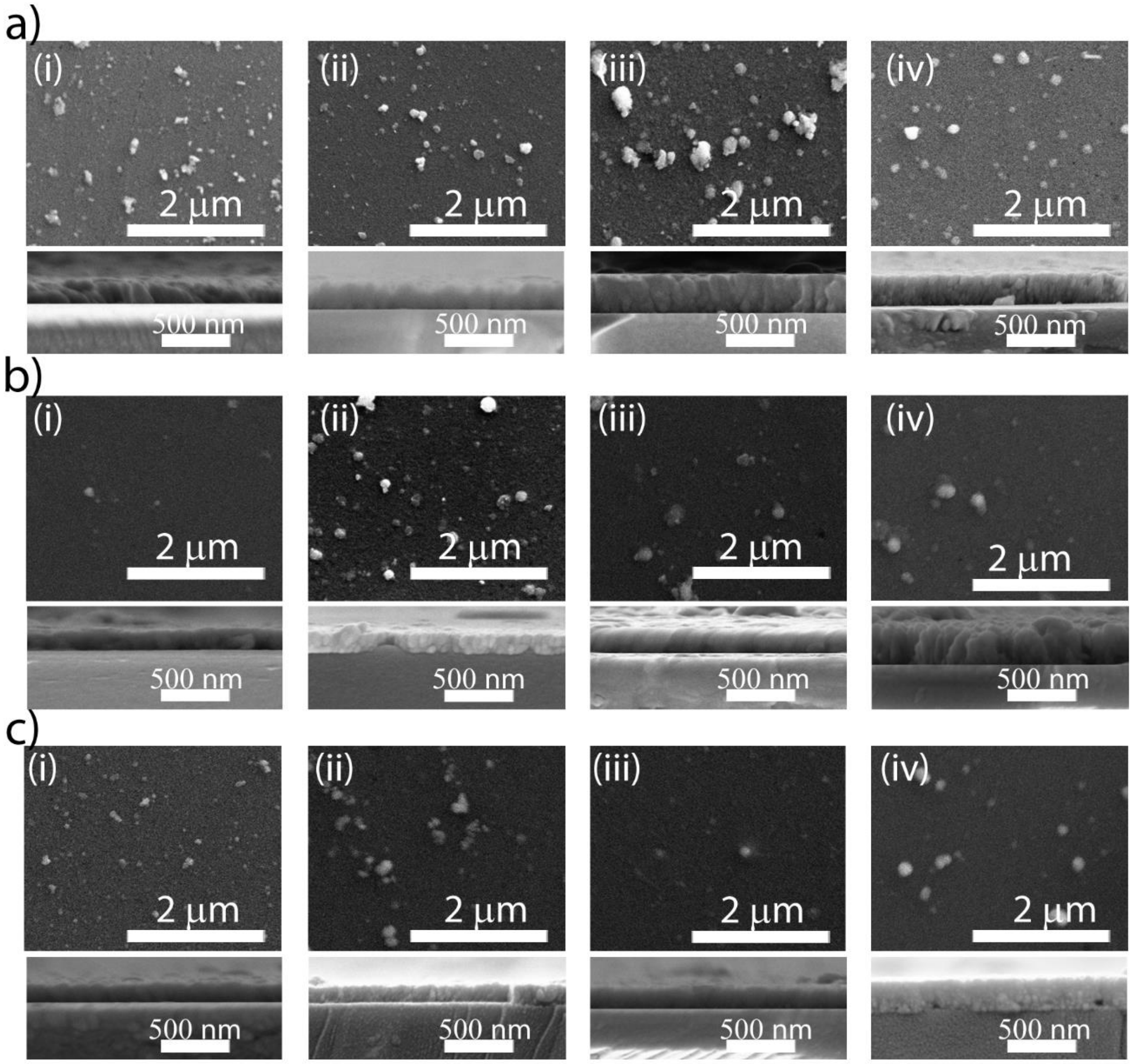

Fig. 3.4: Surface and cross-sectional SEM images of CdS films grown at bath temperatures of (a) 40 °C ((i) 50 nm, (ii) 75 nm, (iii) 200 nm, (iv) 300 nm), (b) 60 °C ((i) 50 nm, (ii) 75

nm, (iii) 175 nm, (iv) 200 nm) and (c) 80 °C ((i) 60 nm, (ii) 125nm, (iii) 150 nm, (iv) 175 nm).

3.4 OPTICAL TRANSMITTANCE AND BANDGAP

The films showed relatively high transparency ranged from 75 to 85 % in the UV-Visible range for all bath temperatures as shown in fig. 3.5. The optical bandgap E_g of the films was estimated from the plot of $(\alpha hv)^2$ as a function of photon energy hv, according to the Tauc formula for the direct bandgap semiconductor [136]. The absorption coefficient α was estimated from the formula $\alpha = (1/d) \ln (1/T)$, where d is the thickness of the film and T is the transmittance. As fig. 3.5d shows, the bandgap decreased with the thickness. The possible reasons of the decreasing bandgap with increase in thickness include many thickness dependent factors such as grain size, lattice strain, stoichiometric deviation, carrier concentration, etc.[137,138] Never the less, the results indicate that the bandgap of the films is similar to that required in solar cell applications (i.e., in the range of 2.3 - 2.6 eV).

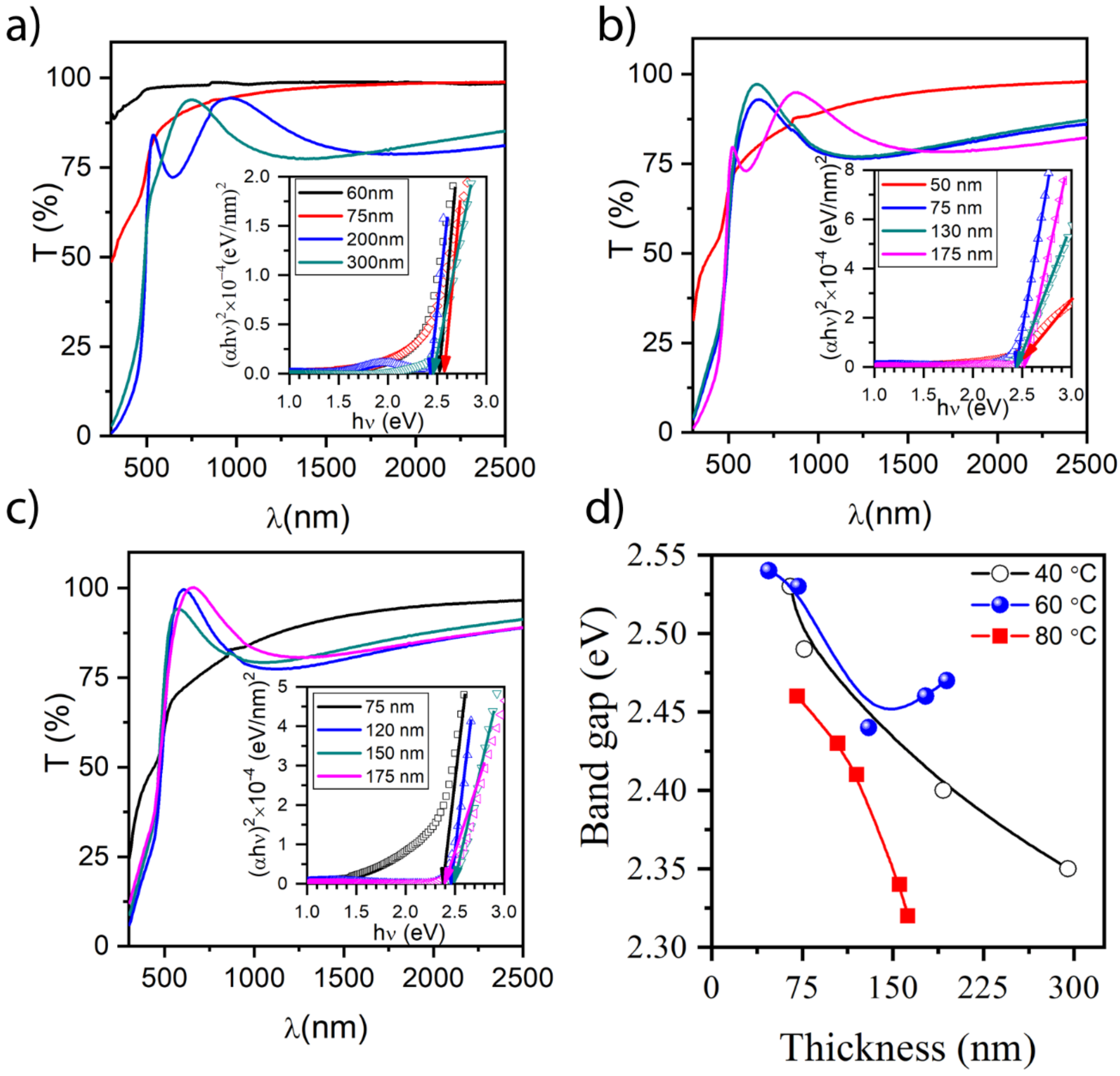

Fig. 3.5: Typical transmittance curves for the films deposited at bath temperature of (a) 40, (b) 60 and (c) 80 °C. (d) Variation of bandgap with thickness for different bath temperature.

3.5 SCALING OF SURFACE ROUGHNESS IN CdS FILMS

There has been great interest in studies on roughness evolution in thin films grown under far-from-equilibrium conditions using kinetic roughening theory [139-142]. The study of evolving surfaces provides insight to the fundamental growth dynamics and enables one to control the roughness of the films. Such a study is of high technological relevance in that roughness of thin films in multilayer structures affects electrical, optical, mechanical and catalytic properties, and hence, determines the eventual performance of devices [143-145].

Typically roughness of a surface evolves as a consequence of simultaneous atomic scale processes such as direct addition of atoms on the growing surface from the surrounding, removal of atoms from the surface and motion of atoms along the surface or diffusive mass transport due to an existing or increasing chemical potential gradient [146] The surfaces in many non-equilibrium growth models such as random surface recrystallization in the Eden model or ballistic aggregation are self-affining fractal which are described by the Kardar–Parisi–Zhang (KPZ) equation [147]

$$\frac{\partial h(x,t)}{\partial t} = \nu\nabla^2 h(x,t) + \frac{\lambda}{2}\left|h(x,t)\right|^2 + \eta \;\ldots\ldots\ldots\ldots\ldots\ldots\ldots\ldots\ldots\ldots\ldots\ldots (3.1)$$

where v accounts for the surface tension, λ is an "excess velocity" in the growth, and η is white noise. The self-affine patterns that the film surfaces develop into can be analyzed by the scaling properties of the surface fluctuations [148]. A number of applications of the KPZ equation were suggested based on the comparison of scaling exponents of surface roughness [139].

The self-affine roughness is widely characterized by engaging it to a dynamic scaling form wherein the root mean square of the fluctuations of the surface height i.e. "the interface width w defined as $w(r,t) = \left\langle \left(h(\vec{r},t) - \left\langle h(\vec{r},t)\right\rangle\right)^2 \right\rangle_{\vec{r}}^{1/2}$, where h is the surface height and $<\ldots>_{\vec{r}}$ is spatial averaging in a system of size L and $r \leq L$, evolves following a simple dynamic scaling known as Family-Vicsek relation":

$$w(r,t) = t^{\beta} f\left(\frac{r}{t^{\beta/\alpha}}\right) \qquad \ldots\ldots\ldots\ldots\ldots\ldots\ldots\ldots\ldots\ldots\ldots (3.2)$$

where the scaling function behaves as $f(\mathrm{u})$ = constant and u^{α} for $\mathrm{u} \gg 1$ and $\mathrm{u} << 1$, respectively, α and β are the roughness and growth exponents respectively. "The set of exponents corresponds to a specific universality class and is suggestive of the underlying mechanism that governs the evolution of roughness." Equation (3.2) suggests that for small r (i.e. $r << t^{\beta/\alpha}$), w is independent of deposition time t and scales as r^{α}, and independent of r for large r when it scales as t^{β}. "The crossover between these two behaviors occurs at $r = \xi$, the lateral correlation length, which signifies the distance at which the surface features are no longer correlated." The correlation length scales as $\xi \sim t^{1/z}$ where the dynamic exponent is defined as $z = \alpha/\beta$.

Although the roughening process during growth of thin films is microscopically diverse and complex in nature, a number of studies on growth of thin films have revealed that the interface roughness follows the Family-Vicsek scaling ansatz. However, in recent years, many experimental and theoretical studies have reported scaling patterns very different from that predicted by the Eq. (3.2) [149-160]. In such cases, "growth models with different exponents at long (global/saturated) and short (local) length scales have been suggested." While the global width $w(L,t)$ still follows the Family-Vicsek scaling relation (Eq. (3.2)), the local width is represented by the anomalous scaling ansatz:

$$w(r,t) \sim \begin{cases} t^{\beta^*} r^{\alpha_{loc}}, & if\ r << \xi << L \\ t^{\beta}, & if\ r >> \xi \end{cases} \qquad \text{……………………} (3.3)$$

"where α_{loc} is the local roughness exponent and β^* is the anomalous growth exponent indicating the time dependence of the local width at length scales smaller than ξ and is given by $\beta - \beta_{loc} = (\alpha - \alpha_{loc})/z$." The time dependence of $w(r,t)$ through the term t^{β^*} is the crucial signature of the anomaly in the scaling behaviour.

As mentioned earlier, deposition at 40 °C is believed to be suitable for solar cell applications due to the slow deposition rate and hence better control on the process. The scaling analysis was carried out for the films deposited at 40 °C. Figure 3.6 shows typical surface morphology of the films of increasing deposition times. A granular structure with even sized grains, typical of polycrystalline thin films is observed at all stages of film growth. From the images, both surface roughening and coarsening process are evident, which is supported from the time sequences of scanned profile of the surfaces wherein the vertical and lateral stretch of the particles increased with the increase in deposition time.

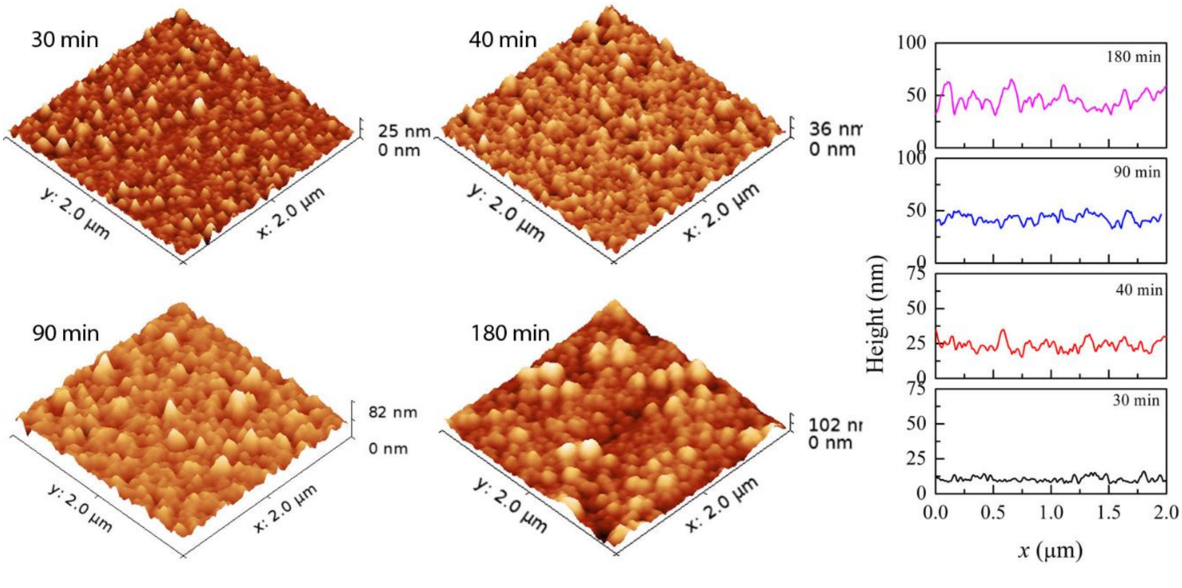

Fig. 3.6: 2 µm × 2 µm AFM images of CBD CdS thin films grown under identical experimental conditions for different durations and the corresponding line profiles across the scan areas.

The growth dynamics and whether roughening of the growth front follows any scaling pattern were assessed from the height-height correlation function $G(r,t)$ defined as $G(r,t) = \left\langle [h(\vec{r}_2,t) - h(\vec{r}_1,t)]^2 \right\rangle$ for each film, which are presented in Fig. 3.7. "$G(r,t)$ shows a power law dependence on r for small length scales and remains saturated at large r values for films of varying deposition times." More importantly, the curves were up-shifted as deposition time increased at all length scales. "This, however, is in contrast with the systems following the Family-Vicsek relation, wherein $G(r,t) \sim [w(r,t)]^2$ exhibit behaviors typical of self-affine interfaces: $G(r,t)$ scales as $G(r,t) \sim r^{2\alpha}$ for $r << \xi$ and becomes constant for $r >> \xi$. The up-lifting of the curves at small length scales indicates the time dependence of $G(r,t)$ and hence, the anomaly in the scaling pattern." Consequently, $G(r,t)$ is expected to follow the scaling relation as given in Eq (3.3), i.e.,

$$G(r,t) \sim w^2 \sim \begin{cases} r^{2\alpha_{local}} t^{2\beta^*} & if\ r << \xi \\ t^{2\beta} & if\ r >> \xi \end{cases} \qquad \text{……………………. (3.4)}$$

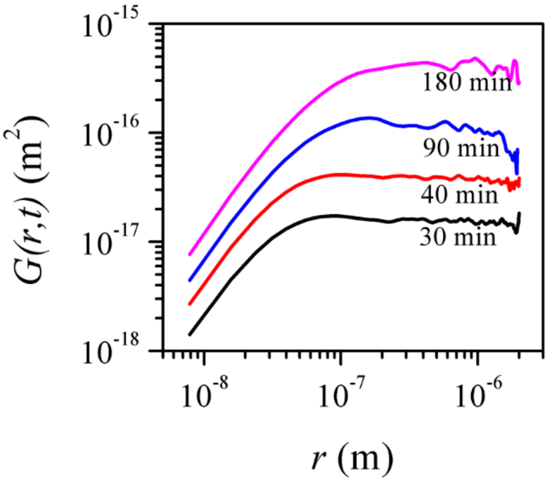

Fig. 3.7: Log-log plot of the height-height correlation function (HHCF) $G(r,t)$ estimated for the films of different deposition times.

The dynamic exponent z was estimated from the time dependent variation of the correlation length ξ, which was accurately determined from the relation $\Gamma(r = \xi)/\Gamma(r = 0) = e^{-1}$ after computing the auto-correlation function $\Gamma(r,t)$ from the AFM images corresponding to different deposition times (not shown here) [161]. The plot of the variation of ξ with deposition t (Fig. 3.8(a)) reveals the scaling of ξ as $\xi \sim t^{1/z}$ with $1/z = 0.46 \pm 0.06$. "The global and local surface widths were estimated from the height-height correlation functions as per Eq. (3.4) and are shown as function of deposition time in Fig. 3.8(b). Both global and local surface widths show a power-law dependence on growth time, typical of anomalous dynamic scaling patterns." The least-square linear fits to the data points yield that the global surface width grew with $\beta = 0.86 \pm 0.05$, much faster than the random deposition limit of stochastic roughening ($\beta = 0.5$). The local surface width, on the other hand increased less rapidly at $\beta_{loc} = \beta - \beta^* =$

0.43 ± 0.10. The fact $\beta^* \neq 0$ confirms the anomalous scaling pattern in the system. The global roughness exponent $\alpha = \beta z$ is calculated to be 1.87 ± 0.35. The observed rapid roughening of the CBD film surface characterized by a high β value is similar to the cases of films grown by sputtering [160].

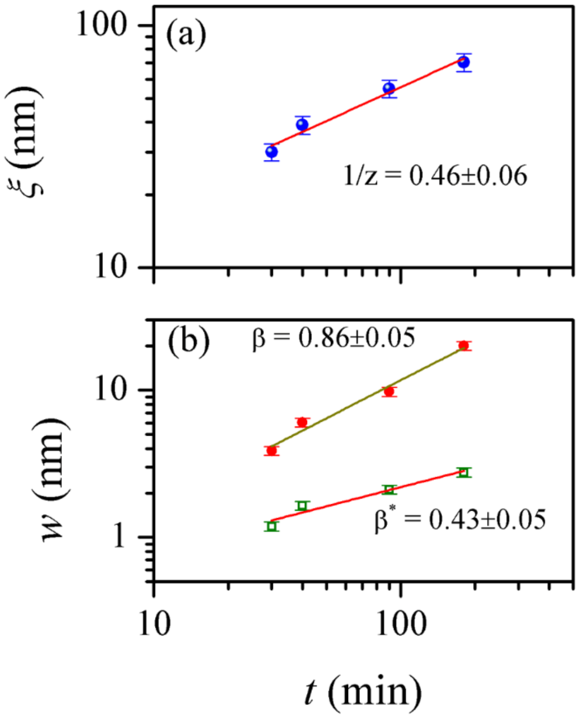

Fig. 3.8: Logarithmic plots of (a) lateral correlation length ξ and (b) interface width w versus deposition time. In the bottom panel, solid circles (●) and open squares (□) represent the data points corresponding to global width and the local width, respectively. Solid lines in both panels are the linear fits to the data. The values of the slopes are indicated.

The consistency of our analysis was verified by collapsing the height-height correlation functions obtained for films of different growth times. As Eq. (4) indicates, the plot of curves $G(r,t)/r^{2\alpha}$ versus $r/t^{\beta/\alpha}$ for all growth times should collapse, with the slopes in small and high arguments being equal to $m_1 = -2(\alpha - \alpha_{loc})$ and $m_2 = -2\alpha$, respectively. We show in Fig. 3.9 that all data points collapse into a single curve confirming the integrity of the general dynamic scaling theory as given in Eq. (3.4). The slope of the curve in small and high arguments was found to be $m_1 = -2.36$ and $m_2 = -3.79$, respectively. It is noted that $m_1 \neq 0$ implies $\alpha \neq \alpha_{loc}$, and therefore, the anomalous scaling behavior in our system. Using the values of m_1 and α, α_{loc} was calculated to be 0.69, which is close to the value 0.78 ± 0.07 calculated from the slope of the $G(r,t)$ vs r curves (Fig. 3.7) for $r << \xi$ as per Eq. (4).

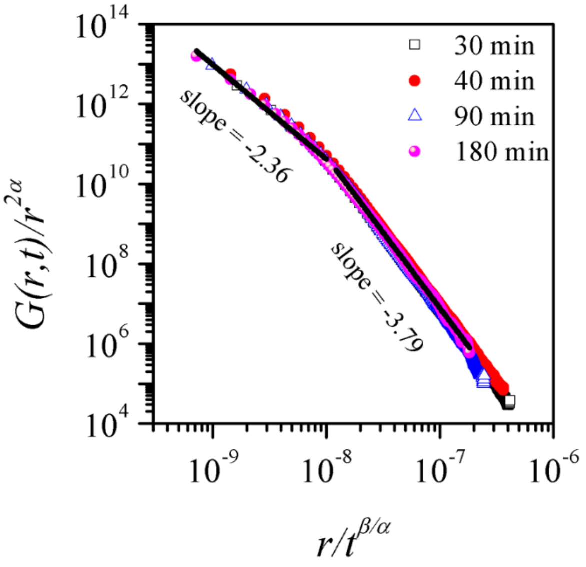

Fig. 3.9: Logarithmic plot of $G(r,t)/r^{2\alpha}$ versus $r/t^{\beta/\alpha}$ for different growth times showing a good data collapse of the height-height correlation function. The solid lines are linear fits to the data points.

More insight into the dynamics of the roughening process in our system was gained from the plot of the power spectral density (PSD) functions for films of different deposition times, as shown in Fig. 3.10. All PSD curves show two distinct regimes: the power law *k* dependence in the high-*k* regime crosses over to a *k*-independent regime at $k_c \sim 1/\xi$ as the surface features lose their correlation. The dynamic scaling behavior in a (2+1)-dimension system is manifested in the PSD as $S(k,t) \sim t^{(2\alpha+2)/z}$ in the low *k*-regime and as $S(k,t) \sim k^{-(2\alpha_s+2)} t^{2(\alpha-\alpha_s)/z}$ in the high *k*-regime for $k >> k_c$ where α_s is the spectral roughness exponent [153]. As seen from the figure, the vertical shift of the PSD curves, especially for high *k*-regime, as the deposition time increased suggests that $\alpha \neq \alpha_s$. The average value of the spectral roughness exponent was obtained as $\alpha_s = 1.49 \pm 0.22$ by measuring the slope of the *k*-dependent PSD plot in the high-*k* regime. The global roughness exponent α can be determined from the time dependence of $S(k,t)$ in the low *k*-regime, which is shown as inset to Fig. 3.10. From the slope, α is found to be 2.20 ± 0.08 which is close to the value independently determined from the scaling relation $\alpha = \beta z$, as discussed above, using the height-height correlation and autocorrelation functions.

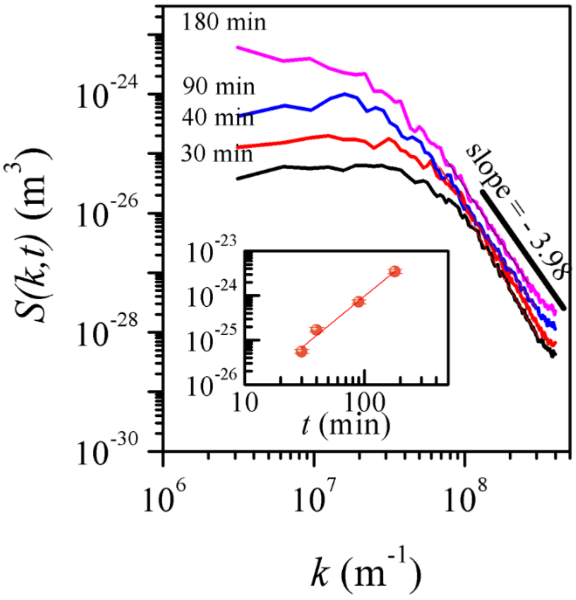

Fig. 3.10: Logarithmic plot of power spectral density function (PSDF) versus wave number k for different growth times. The slope of the PSDF curves for large k values is indicated. Inset: Time dependence curve of $S(k,t)$ in the low k-regime. The line denotes the linear fit to the data points.

The major objectives of the studies of scaling patterns include identification of universality classes and the roughness controlling mechanisms in the growth of thin films based on the evaluated scaling exponents. However, it has not been always straightforward to assign a universality class for films grown in a specific technique. In our case for the CBD CdS thin films, we find that the dynamic evolution of roughness follows a complex scaling behaviour characterized by exponents α_{loc}= 0.78 ± 0.07, α = 2.20 ± 0.08, α_s = 1.49 ± 0.22, $1/z$ = 0.46 ± 0.06, β = 0.86 ± 0.05 and β_{loc}= 0.43 ± 0.10. The scaling relationship $\alpha_{loc} \neq \alpha \neq \alpha_s$ does not belong to any of the known classes of interfacial growth [139,151,153] and indicates a new class [153].

Although the exact mechanism has not been well understood, some studies in recent years have proposed that the anomalous kinetic roughening of the surfaces with a high growth exponent arises as consequences of nonlocal effects [162]. Nevertheless, a clear universality class could not be defined yet. In the case of sputter-deposited thin films, shadowing arising due to the angular spread of the impinging particles works as a nonlocal effect, which led to rapid roughening of the surfaces (i.e., with a high β value) [154, 160, 163]. The shadowing effect, however, cannot be a possible explanation in the present study on CBD thin films.

In the case of solution based methods, which are technologically more attractive, the growth of thin films is inherently complex than the vacuum-based ones, for example MBE. In the few studies on films grown by electroless and electrodeposition techniques, the obtained values of the exponents indicate significant deviation from the universality class as predicted from the KPZ equation [164-168]. The exponents obtained in this work are similar to those found in Refs. [164-169], which suggests that a similar mechanism may govern the dynamic evolution of the roughness of the films studied here. In other words, these exponents might be associated with nonlocal bulk diffusion effects.

In summary, CdS thin films were grown by the CBD process using ammonia-free solutions in a single dip at various bath temperatures ranging from 40 - 80 °C. Bandgap of the films was in the range of 2.3 - 2.6 eV, suggesting their suitability for application CZTS based solar cells. While a higher bath temperature showed fast increase in the thickness, there was structural degradation for thicker films as evidenced from the analysis of the XRD patterns. In view of the slow deposition rate and hence better control, deposition at 40 °C is believed to be suitable for solar cell applications. In order to study the roughening of the films deposited at 40 °C, dynamic scaling theory was employed. The analyses revealed anomalous scaling of roughness with rapid roughening of the surfaces as a consequence of bulk diffusion instability. The characteristic exponents $\alpha_{loc} = 0.78 \pm 0.07$, $\alpha = 2.20 \pm 0.08$, $\alpha_s = 1.49 \pm 0.22$, $1/z = 0.46 \pm 0.06$, $\beta = 0.86 \pm 0.05$ and $\beta_{loc} = 0.43 \pm 0.10$ as determined using the real and Fourier space correlation functions cannot be related to any known universality classes based on local growth models, suggesting that nonlocal effect plays an important role in the evolution of growth front of the CBD thin films. In the light of previous studies on electroless and electrodeposited films, the present results indicate that nonlocal effects in the form of diffusional instability should be incorporated in the models to further our understanding of growth mechanism of the films.

CHAPTER - 4

ROLE OF COMPLEXING AGENT IN EVOLUTION OF SINGLE PHASE KESTERITE CZTS

As mentioned in Section 1.2.2.2, Chapter 1, finding an optimal, low-cost synthesis route having a better control over the composition and phase, while preserving the film quality has become a major challenge in the CZTS based device technology. Although the solution processes are traditionally considered to be one of the most viable approaches for large-scale production, it is important that only non-toxic and environment-friendly solutions are used. In this work, CZTS films were grown via dip coating of ethanol based homogeneous precursor solutions, as outlined in the experimental section (Chapter 2). Ethanol, besides being an environmentally friendly solvent, solvates many common inorganic salts and can evaporate quickly (boiling point is ~78.5 °C) which can minimize residual carbon and/or oxygen related impurities in the films [170]. Among various process parameters that affects the reaction pathway, complexing agents are associated with the release rate of ions and the kinetics of the reaction. This chapter describes the role of a very popular complexing agent, MEA in the growth of phase pure CZTS thin films and demonstrates how by tuning the composition of complexing agent, the formation of binary and ternary sulfide phases can be favored or suppressed.

` As described in the experimental section, 10 ml solutions each of 0.75M of $CuCl_2$, 0.375M of $ZnCl_2$ and 0.375M of $SnCl_2 \cdot 2H_2O$ and 20 ml solution of 3M of TAA in ethanol were prepared separately under constant magnetic stirring at room temperature until the solid salts were completely dissolved. Separately, MEA solutions in ethanol of varying molarity was prepared. To every 10 ml of cationic solution, 10 ml of MEA solution was added making each cationic solution of 20 ml. Finally, the cationic solutions were added sequentially with constant magnetic stirring and the temperature was increased to 60 °C. The cleaned glass slide was vertically dipped in the cationic precursor solution. Afterwards, the anionic solution (TAA solution) was added and continuously stirred for 60 min. After 60 min, the coated substrate was baked in a hot air oven at 130 °C for 10 min. The CZTS precursor thin films were then sulfurized in a tubular furnace with 1 g of sulfur at different temperatures from 300 to 500 °C in the presence of Ar gas. The samples was then naturally cooled down to room temperature under Ar atmosphere.

4.1 FILMS GROWN WITH COMPLEXING AGENT MEA

Figure 4.1 shows photographs of the individual cation solutions prepared with the complexing agent MEA (4 mM) in each and the anion precursor solution. When the Cu, Zn, and Sn solutions were mixed with constant stirring, a milky-green colour slurry was obtained, which latter turned transparent yellow upon addition of the TAA solution. For ethanol based solutions, it is expected that Cu^{2+} and Sn^{2+} will undergo reduction-oxidation reaction through [52,171]

$$2Cu^{2+} + Sn^{2+} \xrightarrow{redox} 2Cu^{+} + Sn^{4+} \tag{4.1}$$

Following reaction (4.1), on mixing the Cu (bright green) and Sn (colourless) solutions, the resultant slurry is believed to be milky-white [171] as the colors of Cu^{+} and Sn^{4+} ions in ethanol are white, and colourless, respectively. However, in this work the colour of the slurry was observed to be milky-green (Fig. 4.1d) which might be due to the simultaneous presence of Cu^{2+} and Cu^{+}, as a consequence of incomplete reduction and oxidation of the Cu^{2+} and Sn^{2+}, respectively due to the MEA-assisted formation of complexes. This was also supported by the Raman and XPS spectra, as discussed in the followings. As part of additional experiments, we found that there was no further change in the colour of the slurry even after 60 min which suggest that the reaction has been completed immediately after addition of the two solutions and there was no further reduction/oxidation. Furthermore, the colour of the slurry was stable when we increased the temperature up to about 80 °C (the boiling point of ethanol is ~78 °C).

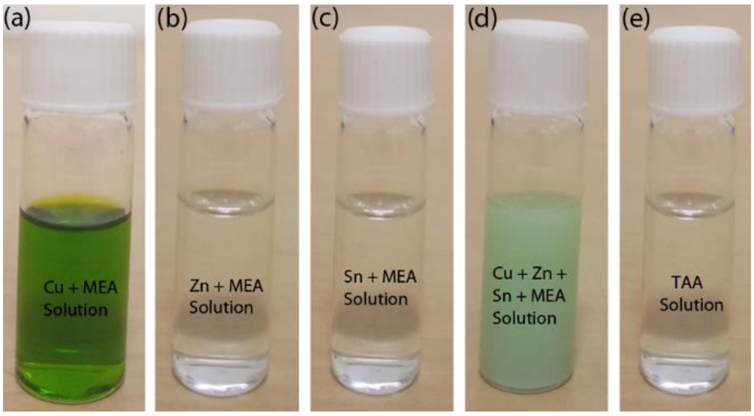

Fig. 4.1: Photographs of the cationic and anionic precursor solutions in each step. Note the colour of the Cu, Zn, Sn and MEA solutions. The milky-green slurry in (d) is thought to arise from incomplete reduction (oxidation) of Cu^{2+} (Sn^{2+}).

The film dip-coated from the above precursor solution and dried at 130 °C for 10 min had a black coloured appearance (Fig. 4.2a). The XRD measurement of this film showed a featureless pattern (Fig. 4.2b) while the Raman spectrum (Fig. 4.2c) is characterized by a broad hump superimposed with a peak at 468 cm^{-1} corresponding to the $Cu_{2-x}S$ phase [172]. This peak associated with the $Cu_{2-x}S$ phase indicates the presence of the Cu^{2+} in the precursor solution, as discussed above. Figure 4.2d shows the core level Cu spectrum which exhibits two prominent peaks centered at ~932.3 and 952.2 eV and a broader one at ~946.2 eV. The former two with a splitting of 19.9 eV are indicative of +1 oxidation state and correspond to the Cu $2p_{3/2}$ and $2p_{1/2}$ peaks, respectively. On the other hand, the peak at ~946 eV is a satellite feature arising due to the presence of Cu^{+2} species [173,174]. The results clearly indicate the simultaneous presence of species with Cu +1 and +2 states, supporting the above discussion.

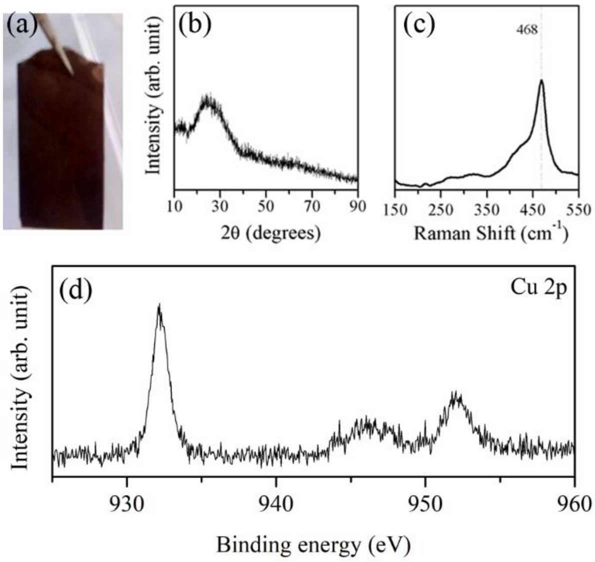

Fig. 4.2: (a) Photograph, (b) XRD pattern, (c) Raman spectrum and (d) core-level Cu 2p XPS spectrum of the film dip-coated from CZTS precursor solution with 4 mM MEA and baked at 130 °C for 10 min.

The above obtained precursor film was sulfurized at various temperature ranging up to 500 °C and the reaction pathway leading to the kesterite phase was ascertained from the detailed XRD and Raman measurements. For the post-sulfurization temperature up to 300 °C, no Bragg peak was observed, which indicates that although the coordination bonds between the sulfur and nitrogen atoms and Cu^{+}, Zn^{+2} and Sn^{4+} ions could have weakened in the metal - TAA complexes [94], it was not sufficient enough to lead to the formation of any crystalline phase. In the XRD pattern of the film sulfurized at 300 °C (Fig. 4.3a), two peaks at about 14.94° and 28.54° appeared. The peak at 14.94° can be identified with the (002) plane of SnS_2 (JCPDS file: 1-89-3198) or (006) plane of $Cu_4S_7S_{16}$ (JCPDS file: 51-932) while the peak at 28.54°

corresponds to the (112) peak of CZTS (JCPDS file: 26-575), (111) peak of ZnS (JCPDS file: 3-65-5476), (111) of cubic Cu_2SnS_3 (JCPDS file: 1-89-2877) or (111) peak of SnS (JCPDS file: 1-89-2755). On increasing the sulfurization temperature to 350 °C, there is no notable difference. When the temperature was further increased to 400 °C, additional peaks at 41.52° and 56.17° was observed. As listed in Table 4.1, the peak at 41.52° corresponds to the (104) peak of SnS_2 and the 56.17° peak is close to the (312) peak of kesterite CZTS, (311) peak of ZnS, and (311) peak of cubic Cu_2SnS_3. Similar to the previous reports, unique identification of the Bragg reflections during growth of the CZTS films is not possible since the peaks appear at close proximity to each other (Table 4.1). For the sulfurization temperature of 450 °C, four more peaks with very low intensity were observed, namely at 22.26°, 29.24°, 45.32° and 47.33°. The peaks at 22.26° and 45.32° correspond to (009) and (21 10) planes of $Cu_4Sn_7S_{16}$ phase (JCPDS file: 51-932), respectively; the peak at 29.24° is close to that due to (101) plane of SnS_2 phase and the peak 47.33° came from the (220) peak of kesterite CZTS, ZnS, and cubic Cu_2SnS_3 [175]. However, for the highest temperature of sulfurization, i.e., 500 °C, all peaks except the ones at 14.94°, 28.54°, 47.33° and 56.17° disappeared. The ions Cu^+ and Zn^{2+} have the same number of electrons and these elements are neighbors in the periodic table. Their atomic scattering factor, which is proportional to the measured intensity in an X-ray diffraction experiment, is identical. Hence these ions are not distinguishable by conventional XRD [176].

Table 4.1: Selected Bragg peak positions and corresponding diffracting planes of various phases in the Cu-Zn-Sn-S system

CZTS (JCPDS File: 26575)		$Cu_4Sn_7S_{16}$ (JCPDS File: 51932)		ZnS (JCPDS File: 3655476)		Cu_2SnS_3 (JCPDS File: 1892877)		SnS (JCPDS File: 1892755)		SnS_2 (JCPDS File: 1893198)	
2θ (°)	Hkl	2θ (°)	hkl	2θ (°)	hkl	2θ (°)	hkl	2θ (°)	hkl	2θ (°)	Hkl
-	-	14.79	006	-	-	-	-	-	-	14.99	002
-	-	22.26	009	-	-	-	-	-	-	-	-
28.53	112	-	-	28.58	111	28.44	111	28.36	111	-	-
-	-	-	-	-	-	-	-	-	-	29.25	101
-	-	-	-	-	-	-	-	-	-	32.17	102
-	-	-	-	-	-	-	-	-	-	41.84	104

-	-	45.33	2110	-	-	-	-	-	-	-	-
47.33	220	-	-	47.55	220	47.31	220	47.17	220	-	-
56.17	312	-	-	56.42	311	56.13	311	-	-	-	-

Further analysis of the crystalline phases in the samples was carried out using Raman measurements (Fig. 4.3b). When the films underwent sulfurization at 300 °C, a peak centered at 315 cm^{-1} and a broad hump at ~354 cm^{-1} appeared corresponding to SnS_2 and cubic Cu_2SnS_3 phase, respectively [177,178]. The absence of the CuS peak (present in the as-deposited film, Fig. 4.2c) implies its reaction with the Sn^{4+} and S^{2-} to form SnS_2 and Cu_2SnS_3, as indicated from both XRD and Raman studies. As the sulfurization temperature was increased to 450 °C, the peak at 354 cm^{-1} disappeared and the intensity of the 315 cm^{-1} peak increased. For the 500 °C sulfurized sample, two relatively broad peaks at 305 and 348 cm^{-1} appeared, which are identified with the $Cu_4Sn_7S_{16}$ [179]. It may be noted that a peak at ~348 cm^{-1} is expected for ZnS in resonant Raman measurements [180]. This suggests that the cubic Cu_2SnS_3 reacted with SnS_2 resulting in the formation of the $Cu_4Sn_7S_{16}$ phase.

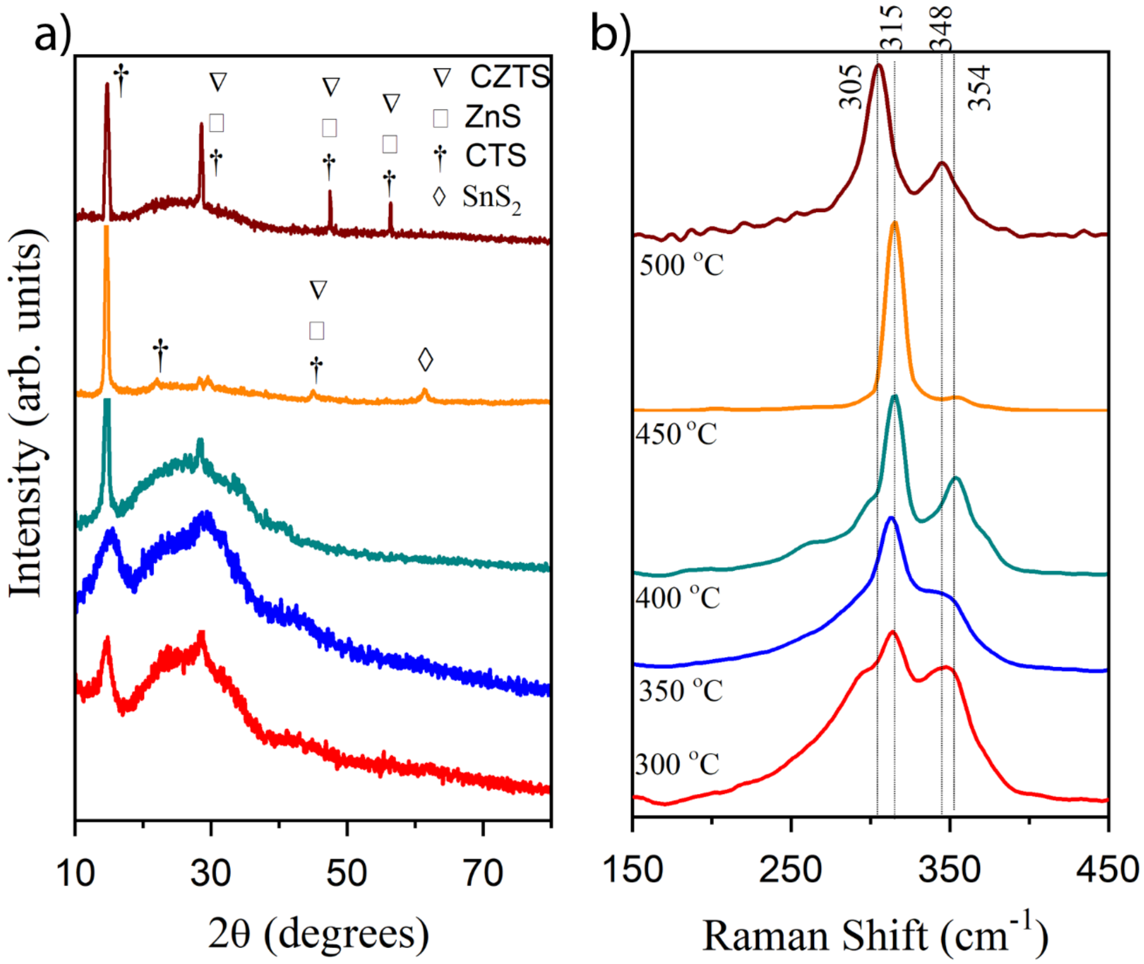

Fig. 4.3: Typical (a) XRD patterns and (b) Raman spectra of film deposited using 4 mM MEA and sulfurized at various temperatures ranging from 300 to 500 °C. The main peaks in both the panels are marked.

Based on the above analysis of the XRD and Raman data, we propose the following reaction pathway during the post-sulfurization of the films prepared from the ethanol based solution:

$$Cu^{2+} + S^{2-} \rightarrow CuS \qquad (130\ °C) \qquad (4.2)$$

$$2CuS + 2Sn^{4+} + 3S\ (g) \rightarrow SnS_2 + Cu_2SnS_3 \qquad (300\ °C) \qquad (4.3)$$

$$5SnS_2 + 2Cu_2SnS_3 + ZnS \rightarrow ZnS + Cu_4Sn_7S_{16} \qquad (500\ °C) \qquad (4.4)$$

Although the experimental evidences of the above reactions could be provided, we failed in preparing phase-pure CZTS films even at a reasonably high temperature of 500 °C. It appears that the failure of interaction between the metal complexes, especially of Zn with others, could be the primary reason for the same. When we reduced the MEA concentration by an order to 0.4 mM, the XRD patterns for the films (Fig. 4.4a) were similar to that for the films grown with 4 mM MEA concentration (Fig. 4.3a). However, there were a few notable differences in the Raman spectra between these two sets of films. For instance, instead of a lone peak at 305 cm^{-1} (Fig. 4.3b), two superimposed peaks centered at 289 and 298 cm^{-1} (identified with CZTS and Cu_2SnS_3 phases, respectively) and a sharper peak at ~348 cm^{-1} (corresponding to $Cu_4Sn_7S_{16}$ and/or ZnS phase) were observed (Fig. 4.4b) for the sulfurization temperature of 500 °C. Based on these observations, the plausible reaction leading to the products at 500 °C may be given by reaction (4.5).

$$5SnS_2 + 3\mathrm{Cu_2SnS_3} + 2S(\mathrm{g}) + 2Zn^{+2}$$
$$\rightarrow ZnS + Cu_2ZnSnS_4 + Cu_4Sn_7S_{16} \qquad (500\ ^{\circ}\mathrm{C}) \qquad (4.5)$$

This suggests that the reduction of the MEA concentration modified the reaction pathway that resulted in the formation of CZTS phase along with the other phases.

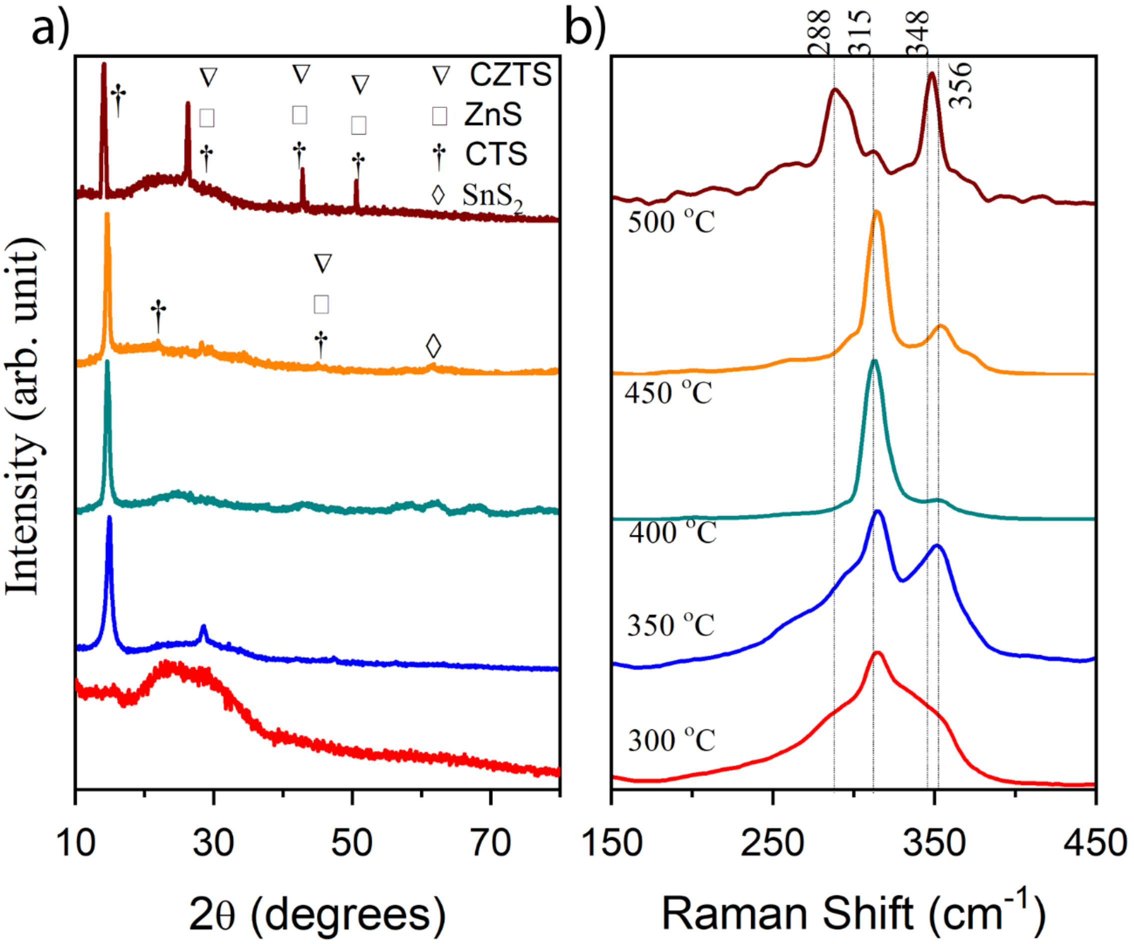

Fig. 4.4: Typical (a) XRD patterns and (b) Raman spectra of film deposited using 0.4 mM MEA and sulfurized at various temperatures.

4.2 FILMS GROWN WITHOUT COMPLEXING AGENT MEA

4.2.1 Evolution of Phase

The results, however, were very contrasting when the films were grown without the complexing/chelating agent MEA. As shown in fig. 4.5a, a milky-white slurry was obtained when the Cu and Sn precursor solutions were mixed against the milky-green slurry observed for the MEA containing solutions (Fig. 4.1). This clearly indicates the reduction of Cu^{2+} to Cu^{+} and oxidation of Sn^{2+} to Sn^{4+}. The XRD pattern, Raman spectrum and the high resolution core level Cu curve of the film dried at 130 °C are shown in Figs. 4.5b, 4.5c and 4.5d, respectively. Compared to the films with MEA (Fig. 4.2), there was no difference in the XRD pattern; however, the peak at ~468 cm^{-1} observed in the Raman spectrum (Fig. 4.2c) was absent. The Cu 2p spectrum showed two clear peaks with a splitting of ~19.8 eV corresponding to the Cu $2p_{3/2}$ and $2p_{1/2}$ peaks. More importantly, the satellite feature corresponding to +2 oxidation state of Cu (as observed in fig. 4.2d) completely disappeared, which supports the above argument of reduction of Cu^{2+} to Cu^{+} facilitated by the absence of MEA. For the increased sulfurization temperature of 300 °C (Fig. 4.6a), clear Bragg peaks at 22.26°, 28.54° and 32.11° were observed. The peak at 22.26° peak may correspond to $Cu_4Sn_7S_{16}$ (009) plane, JCPDS file: 51-932) phases while the peak at 28.54° may be identified with CZTS ((112) plane, JCPDS file: 26-575), ZnS ((111) plane, JCPDS file: 3-65-5476), Cu_2SnS_3 ((111) plane, JCPDS file: 1-89-2877) and SnS ((111) plane, JCPDS file: 1-89-2755) and the peak at 32.11° may belong to SnS_2 ((102) plane, JCPDS file: 01-089-3198), as listed in Table 4.1. Interestingly, the peak at 22.26° converted to a broad shoulder and the peak at 28.54° became prominent for the increase in the sulfurization temperature to 350 °C. There were two extra small peaks at 47.33° and 56.17° which may belong to CZTS, ZnS, Cu_2SnS_3 and SnS, as entered in Table 4.1. The intensity of these peaks continuously increases for higher sulfurization temperatures up to 500 °C. At the highest temperature of sulfurization, i.e., 500 °C, the film is characterized by three intense peaks at 28.54, 47.33 and 56.17°.

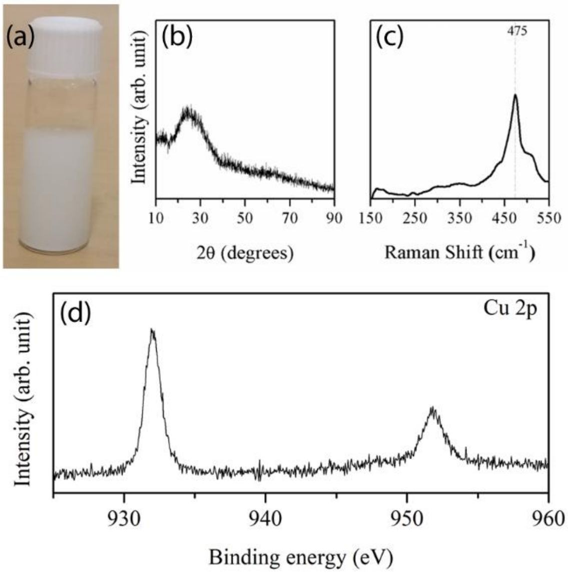

Fig. 4.5: (a) Photograph of milky-white slurry obtained in mixing Cu, Zn and Sn precursor solutions. Note the difference in colour compared to Fig. 4.1(d) due to absence of MEA leading to the complete reduction (oxidation) of Cu^{2+} (Sn^{2+}); (b) XRD pattern, (c) Raman spectrum and (d) core-level Cu 2p XPS spectrum of the film dip-coated from CZTS precursor solution without MEA and baked at 130 °C for 10 min.

Figure 4.6b shows the typical Raman spectra of the films sulfurized at various temperatures. For the sample sulfurized at 300 °C peaks at 298, 315 and 354 cm^{-1} appeared, which may be identified with the $Cu_4Sn_7S_{16}$, ZnS and SnS_2, respectively as given in Eq. (4.6) below [177,179,180]. A peak at 338 cm^{-1} (corresponding to the CZTS phase) in addition to the other peaks appeared when the sulfurization temperature was increased to 350 °C indicating the initialization of the formation of the CZTS phase. A similar trend was observed for the increase in the sulfurization temperature up to 450 °C. At 450 °C, partial decomposition of $Cu_4Sn_7S_{16}$ leading to the formation of Cu_2S and SnS_2 (Eq. 4.7) was observed in the form of re-appearance of the Raman peaks. When the temperature was further increased to 500 °C, the undesirable peaks disappeared accompanied by the increase in the intensity of the peak 338 cm^{-1} and appearance of a new peak at 288 cm^{-1} which is consistent with the previously reported CZTS Raman spectral data [181]. The presence of these two sharp peaks confirms the formation of phase pure CZTS films. The possible reactions in this case are proposed to be:

$$2Cu^{+} + S^{2-} \rightarrow Cu_2S \qquad (130\ ^\circ\mathrm{C}) \qquad (4.6)$$

$$2Cu_2S + 8SnS_2 + Zn^{+2} + S(g) \rightarrow Cu_4Sn_7S_{16} + ZnS + SnS_2 \qquad (300\ ^\circ\mathrm{C}) \qquad (4.7)$$

$$Cu_4Sn_7S_{16} \rightarrow 2Cu_2S + 7SnS_2 \qquad (450\ ^\circ\mathrm{C}) \qquad (4.8)$$

$$Cu_2S + ZnS + SnS_2 \rightarrow Cu_2ZnSnS_4 \qquad (500\ ^\circ\mathrm{C}) \qquad (4.9)$$

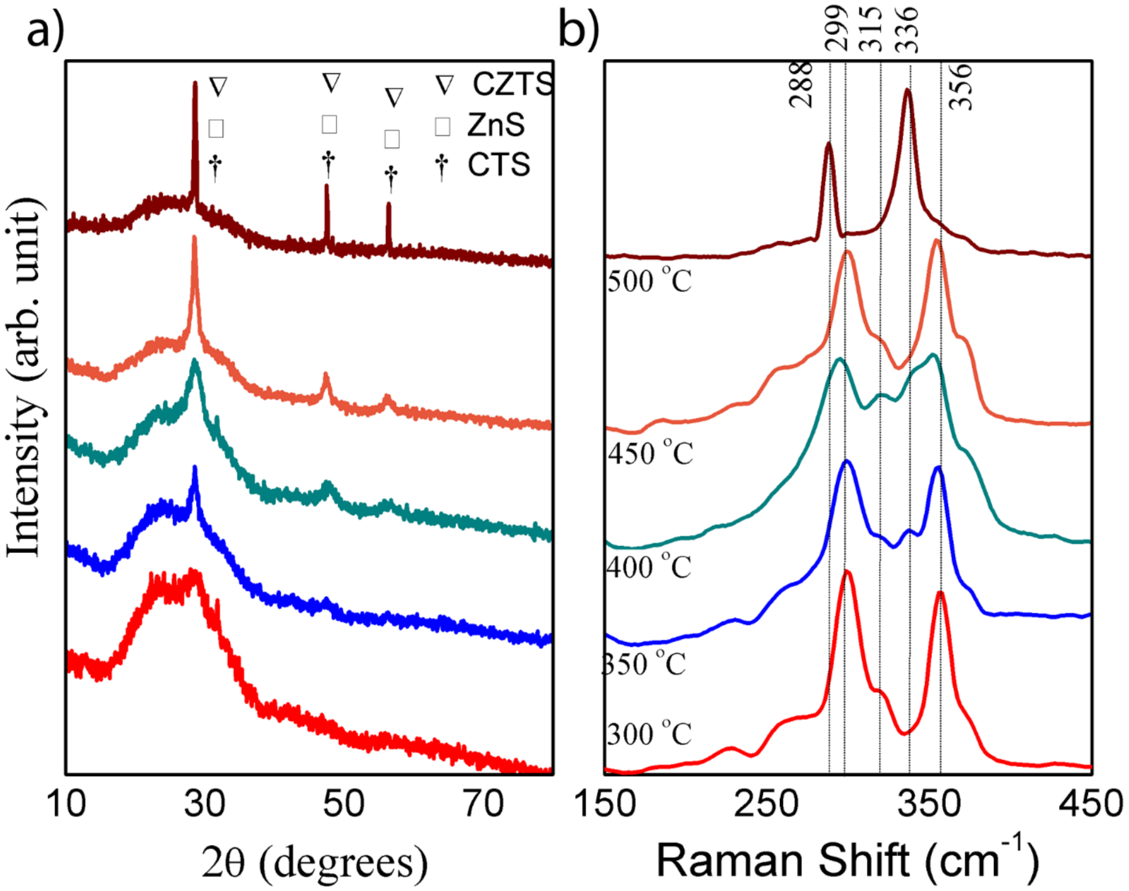

Fig. 4.6: Typical (a) XRD patterns and (b) Raman spectra of film deposited from solution without MEA and sulfurized at various temperatures.

The typical high resolution core level spectra acquired in the Cu 2p, Zn 2p, Sn 3d and S 2p regions for the sample grown without MEA and sulfurized at 500 °C are presented in Fig. 4.7. The Cu 2p spectrum is characterized by two symmetric peaks corresponding to Cu $2p_{3/2}$ and $2p_{1/2}$ separated by 19.9 eV, consistent with the reported values for CZTS [182,183]. The Zn 2p core level spectrum showed the Zn $2p_{3/2}$ and Zn $2p_{1/2}$ peaks at 1021.3 and 1044.3 eV, respectively with a peak splitting of 23 eV, confirming the +2 state of Zn. In the Sn 3d region, the peaks corresponding to $3d_{5/2}$ and $3d_{3/2}$ were observed at 485.8 and 494.3 eV, respectively. With the separation between the peaks of about 8.5 eV, the +4 state of Sn species is established [184,185]. The core spectrum of the S 2p showed binding energies for S $2p_{3/2}$ and S $2p_{1/2}$ peaks of 161.4 and 162.5 eV, which is in agreement with the 160-164 eV range expected for S in the sulfide phase [184,185]. The binding energy values for Cu, Zn, Sn and S agrees well with those reported previously [182-185].

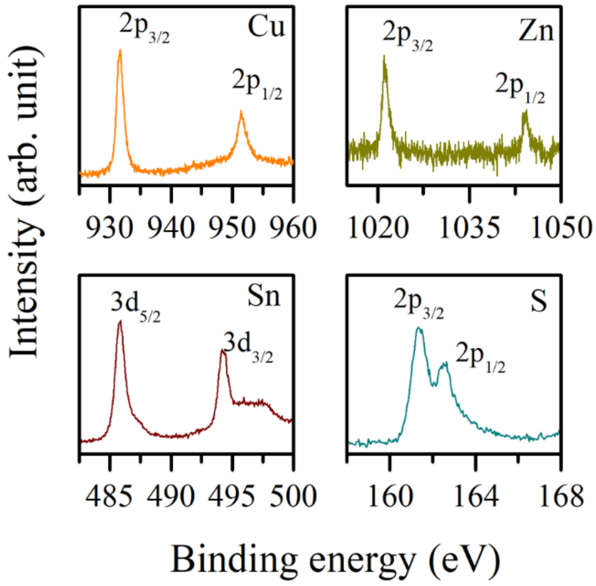

Fig. 4.7: Typical core level spectra for Cu 2p, Zn 2p, Sn 3d and S 2p of the CZTS film grown from solutions without MEA and sulfurized at 500 °C.

Based on the Raman studies in conjunction with the XRD measurements, it is revealed that for these films the reaction pathway followed from the consequence of post-sulfurization treatment is very different from that of the films grown with MEA and is summarized schematically in Fig. 4.8. For the films grown with complexing agent MEA, at 130 °C, CuS is formed which is a consequence of incomplete reduction and oxidation of the Cu^{2+} and Sn^{2+}. When the films underwent sulfurization at 300 °C, the CuS present in the as-deposited film reacted with the Sn^{4+} and S^{2-} to form SnS_2 and Cu_2SnS_3, as indicated from both XRD and Raman studies. When the sulfurization temperature was increased to 500 °C $Cu_4Sn_7S_{16}$ and ZnS phases were present. It appears that the failure of interaction between the metal complexes, especially of Zn with others, could be the primary reason for the same. However, at same temperature with reduced MEA concentration the reaction pathway was modified that resulted in the formation of CZTS phase along with the other phases.

On the other hand, the absence of the complexing/chelating agent facilitates early formation of the CZTS phase, which suggests a smaller activation energy for the decomposition of the precursor complex. Furthermore, the amorphous compound formed from drying the original precursor solution, which is a mixture of three metal–TAA complexes, readily decomposes into the sulfide phases at relatively low temperature (for example, the formation of Cu_2S at 130 °C). This is different to the other liquid based methods that requires dispersing agents to suspend nano- or micro-scale particles at elevated temperature [22]. When the films underwent sulfurization at 300 °C, Cu_2S presumably reacted with SnS_2, Zn^{2+} and S^{2-} to yield

$Cu_4Sn_7S_{16}$, ZnS and SnS_2. At 500 °C, CZTS phase was obtained, suggesting completion of the reaction among various phases.

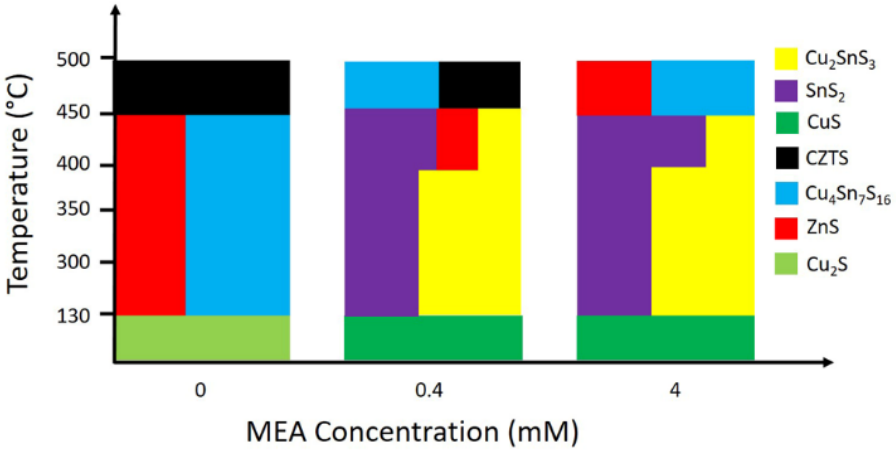

Fig. 4.8: Summary of the stable phase evolution as a function of post-sulfurization temperature and MEA concentration. The results were derived from the detailed analyses of XRD and Raman data.

4.2.2 Surface features

We then evaluated various properties such as microstructure, optical bandgap and photo-responsive properties of the phase-pure CZTS samples (grown with no MEA and post-sulfurized at 500 °C). Figure 4.9 shows a representative FESEM images of surface and cross-sectional view (inset) of the films, wherein a uniform dense microstructure without any visible cracks or pin-holes was observed. The thickness of the films grown from the single dip scales about 200 nm, suggesting the requirement for multiple dips for the reasonable 1 μm thickness required for the photovoltaic device fabrication. Nevertheless, the compact microstructure, a prerequisite for better efficiency, has been achieved.

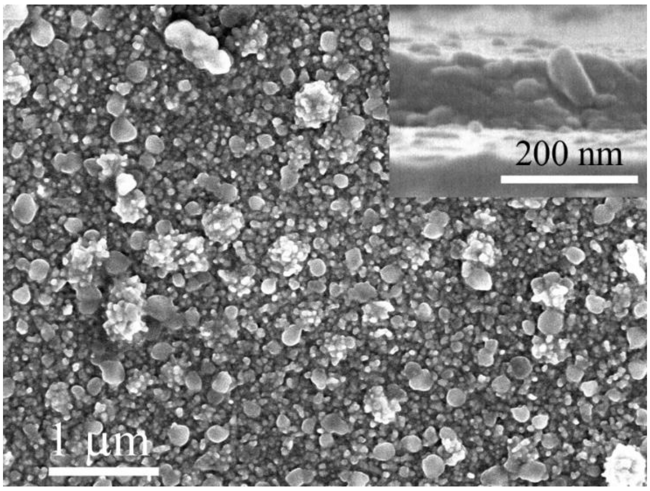

Fig. 4.9: Typical FESEM image of surface and cross sectional view (in set) of the phase-pure CZTS film grown from solutions without MEA and sulfurized at 500 °C.

4.2.3 Optical bandgap

Figure 4.10a shows the typical UV-visible-NIR reflectance (*R*) and transmittance (*T*) curves of the above film. As evidenced from the figure, the typical smaller values of *R* and *T* suggest strong absorption of the incident radiation in the range of 300 - 950 nm. The optical absorption coefficient α estimated using the formula $\alpha = (1/d) \ln [(1-R)^2/T]$ for the film of thickness *d,* was the order of 10^5 cm^{-1}. Such a high of absorption coefficient is highly favorable for efficient photon absorption and generation of electron-hole pairs [186]. The direct optical bandgap E_g of the films was evaluated to be 1.44 eV from the plots of $(\alpha h\nu)^2$ vs photon energy hν, as shown in Fig. 4.10b. The observed value of the bandgap of the CZTS films is similar to the values reported by several earlier researchers [22, 80,187-189].

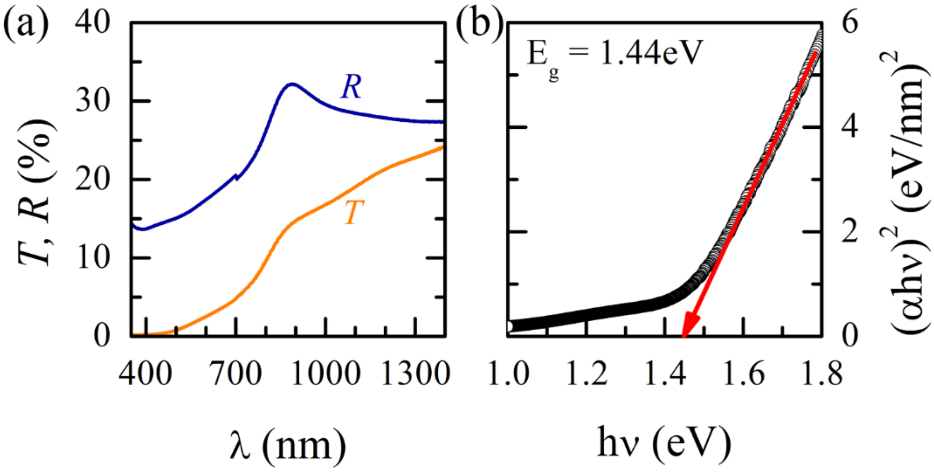

Fig. 4.10: (a) The UV-Vis-NIR reflectance and transmittance curves, and (b) Tauc plot of $(\alpha h\nu)^2$ vs hν for the phase pure CZTS films grown from solutions without MEA.

4.2.4 Electrical properties

The results of the Hall measurement revealed the p-type conductivity of the above sample (i.e., the phase pure sample grown with solutions without MEA and sulfurized at 500 °C). The carrier concentration, resistivity and Hall mobility of the film were determined to be ~4.1×10^{19} cm^{-3}, 4.22×10^{-2} Ω.cm and 3.61 cm^2 V^{-1} s^{-1}, respectively.. The obtained values are similar to the ones reported in literature [97,190,191]. In CZTS films, the electrical properties of the CZTS films are reportedly governed by the native defects and are strongly influenced by the processing of the films [191-193]. In particular, the high concentration in CZTS films has been attributed to the Cu-poor and Zn-rich composition [191-193].

The semi log-linear voltage - current characteristics of the phase CZTS films under dark and white light (AM 1.5G, 100 mW/cm^2) illumination are presented in Fig. 4.11a. The change in current with respect to the dark current ($\Delta I\ (\%) = [(I_{light} - I_{dark}) / I_{dark}] \times 100$) is shown in Fig. 4.11b as a function of bias. The inset to the figure (Fig. 4.11b) shows the device configuration. The films showed huge increase in current (better than 275% at 6 V bias) under illumination indicating a promising photoresponse performance of the films, as expected from an absorber layer to be potentially used in photovoltaic devices. The enhanced photocurrent is related to the absorption of the incident radiation followed by generation and dissociation of the exciton [194]. The non-linear behavior of the curves (Fig. 4.11a) is attributed to the thermionic emission associated with the two back-to-back Schottky junctions (Al-CZTS) connected through a resistance [195-197]. In the dark condition, the Fermi level of CZTS film is aligned with that of Al contacts and when a bias is applied, one junction becomes forward biased while the other one is reverse biased. Assuming that the barrier heights at both contacts remain the same, a symmetric *V-I* (in first and third quadrant) is expected. On the other hand, under stable illumination, absorption of photons with energy higher than E_g of the CZTS film results in the creation of electron-hole pairs. These additional carriers cause the split of the Fermi level into quasi-Fermi levels and consequently, affect the barrier heights and the carrier transport dynamics. As reported earlier [196], lowering of the barrier height favors a higher current density, symmetric in nature for the forward and biased regimes, which may be the case for the work presented here.

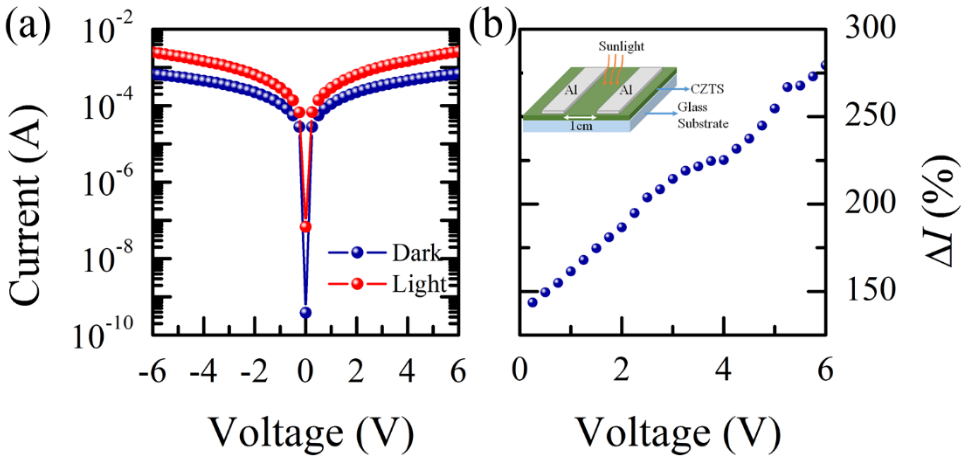

Fig. 4.11: (a) Voltage - current characteristics under dark and light illumination of the phase pure CZTS film grown from solutions without MEA and sulfurized at 500 °C; (b) Plot of change in current with respect to the dark current (ΔI (%) = $[(I_{light} - I_{dark}) / I_{dark}] \times 100$) versus bias voltage. Inset shows the device configuration.

In summary, the reaction mechanisms in transformation from precursor solution to CZTS phase via intermediate solid state binary and ternary compounds during deposition and the subsequent sulfurization treatment in the ethanol based solution process has been elucidated. In the initial stage of solution mixing, the presence of the complexing agent MEA inhibited the complete reduction of Cu^{2+} to Cu^{+} and oxidation of Sn^{2+} to Sn^{4+}, which subsequently affected the reaction pathway resulting in undesirable secondary phases. Contrastingly, the absence MEA facilitated early formation of the CZTS phase revealing a smaller activation energy for the decomposition of the precursor complex. The reaction pathway is demonstrated to be different to the other liquid based methods that requires dispersing agents to suspend nano- or micro-scale particles at elevated temperature. The phase pure CZTS films had a bandgap of 1.44 eV and showed highly promising photoresponse behavior in that there was ~ 275% change in current upon white light illumination at a bias of 6 V.

CHAPTER – 5

IMPACT OF HIGH TEMPERATURE ANNEALING CONFIGURATION ON PHASE EVOLUTION OF CZTS FILMS

While studying the phase evolution in the films grown by direct deposition of solutions via dip coating, it was established that MEA, a very popular complexing agent, inhibited the complete reduction (oxidation) of Sn^{2+} (Cu^{2+}) which in turn led to impurity phases. On the other hand, solutions without MEA yielded phase pure kesterite CZTS for a post-sulfurization at 500 °C. As shown in the previous chapter sulfurization temperature is a critical parameter that determines the phase of the films. As outlined in Section 1.2.2.2, Chapter 1, HTA forms a very critical process step in fabrication of single phase CZTS thin films. Uncontrolled loss of volatile element during HTA may result in compositional variation in sulfurized CZTS films that hampers the performance of CZTS solar cells. While studying the stability of the CZTS thin films during sulfurization process, Scragg et al. have reported the critical role of increased sulfur pressure in reducing the loss of volatile element and thereby improving stability of the CZTS films [37]. Furthermore, it has been shown that the chemical path of material formation and the material properties are strongly dependent on the rate of temperature rise [180, 198,199]. This highlights the role of HTA settings in growth of phase pure CZTS thin films. While, a HTA strategy that is simpler and avoids overly-critical configurations is highly preferred, it is necessary to ascertain the influencing mechanisms of the same and rationalize the growth patterns for reliable reproduction of the CZTS films. In this chapter, an elaborate comparative study of geometry-controlled HTA settings including systematic variations in the ramp rate, sulfur source temperature and the reaction temperature is presented. Based on the results we propose a strategy for facile synthesis of phase-pure kesterite CZTS thin films from environment-friendly ethanol based solutions by direct deposition of the solution via dip coating.

The precursor film was grown as per the recipe given in the previous chapter. Briefly, a mixture of separately-prepared clear and transparent cationic solutions in ethanol (0.75M of $CuCl_2$, 0.375M of $ZnCl_2$ and 0.37M of $SnCl_2{\cdot}2H_2O$) was prepared. In this mixture solution, a glass slide was vertical dipped and the TAA solution (3.0 M) was added. The precursor solution temperature was kept at 60 °C. After 60 min, the glass slide was removed from the solution and was baked in a hot air oven at 130 °C for 10 min. The thus prepared precursor films on the substrates were then sulfurized in a tube furnace with different HTA settings as illustrated in fig. 5.1. In configuration -I (Fig. 5.1a), the sulfur source and precursor film (i.e., the reaction zone) were maintained at different temperatures (the precursor films was held vertical facing the in-coming sulfur vapor), typical of two-zone sulfurization process whereas in configuration-II (Fig. 5.1b), the precursor film and sulfur flakes (film was placed horizontally facing down the flakes taken in an alumina crucible) were kept at same temperature. In all cases, elemental sulfur flakes was used as source to provide the sulfur vapor during HTA. The temperature profile of the reaction zone for both the configurations is depicted in Fig. 5.1c. Please note that for configuration-I, the temperature profile of the sulfur source was similar to that of the reaction zone except that the maximum temperature was 300 °C.

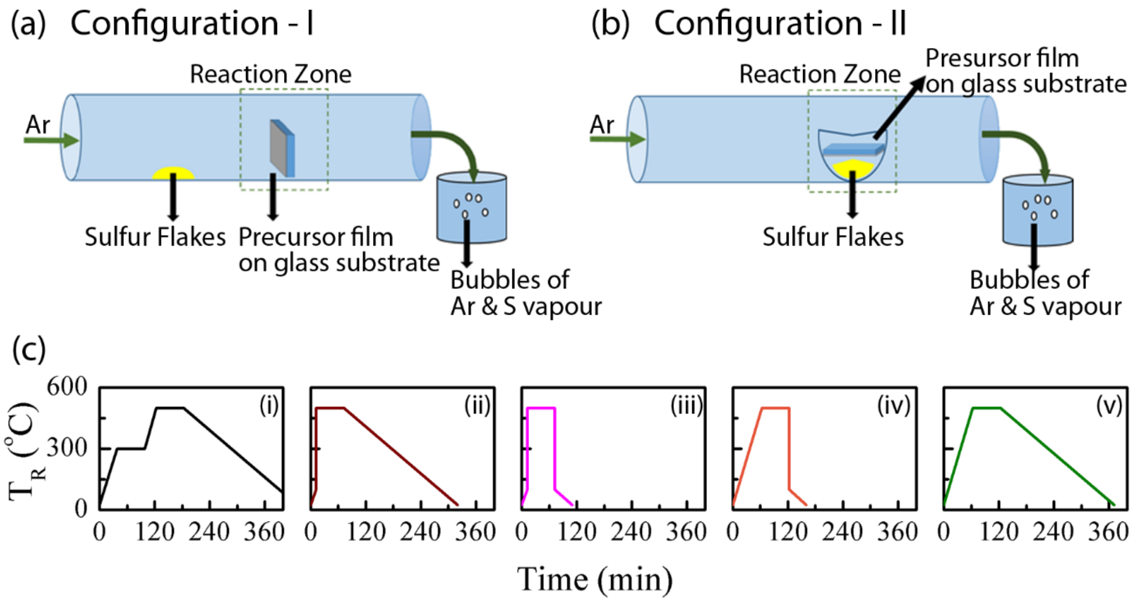

Fig. 5.1: Schematic diagram of (a) Configuration-I, (b) Configuration-II and (c) Temperature profile of the reaction zone during HTA; (i) two-step sulfurization for 60 min at each step, (ii) Rapid heating and normal cooling, (iii) Rapid heating and rapid cooling, (iv) Normal heating and rapid cooling, (v) Normal heating and cooling. Normal heating and normal cooling refers to heating at the rate of 8 °C/min and furnace cooling.

5.1 CHARACTERIZATION OF FILMS GROWN VIA CONFIGURATION I

5.1.1 Determination of Phase

Figure 5.2 shows typical XRD patterns of the films grown via Configuration - I. For the film grown by two-step annealing, i.e., 300 °C for 60 min followed by 500 °C for 60 min (profile (i) in Fig. 5.1c) Bragg reflections at 18.09, 28.54, 47.33 and 56.17° were observed (Fig. 5.2a). The peak at 18.09° correspond to $(\bar{1}\bar{1}3)$ plane of anorthic Cu_2SnS_3 phase (JCPDS file: 27-198) while the peaks at 28.54, 47.33 and 56.17° may correspond to the (112), (220) and (312) planes of CZTS (JCPDS file: 26-0575), or (111), (220) and (311) planes of ZnS (JCPDS file: 3-65-5476), or (111), (220) and (311) of cubic Cu_2SnS_3 (JCPDS file: 1-89-2877). The result thus suggests that the intermediate annealing helped in avoiding the loss of Sn from the sample, as indicated by the formation of CZTS phase [200,201]. However, due to the longer annealing time, Cu_2SnS_3 formed first and possibly, prevented the reaction to proceed further for the growth of pure CZTS [202].

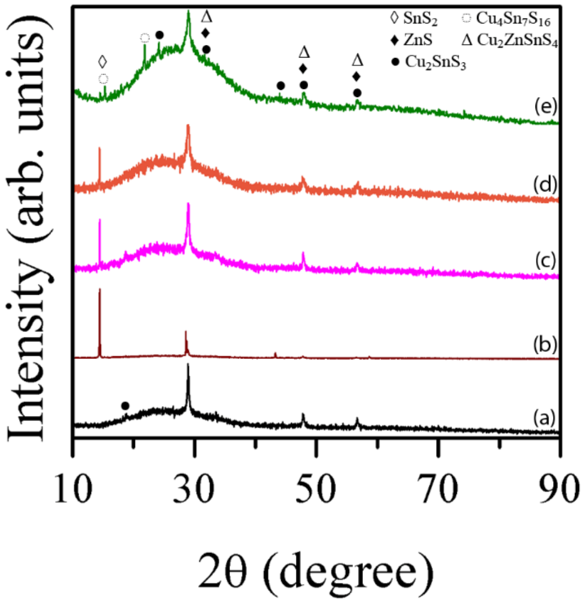

Fig. 5.2: Typical XRD pattern of the films prepared by HTA via Configuration-I with (a) two - step sulfurization for 60 min at each step, (b) Rapid heating and normal cooling, (c) Rapid heating and rapid cooling, (d) Normal heating and rapid cooling, (e) Normal heating and cooling. Normal heating and normal cooling refers to heating at the rate of 8 °C/min and furnace cooling.

Considering that the reaction pathway in the Cu-Zn-Sn-S system is influenced by the ramp rate [180,198,199], we have examined next whether rapid heating and/or rapid cooling of the precursor film assists in avoiding the formation of any stable intermediate compound and in producing single phase CZTS. The temperature profiles (ii), (iii) and (iv) in Fig. 5.1c highlight these efforts. As seen from profile (ii) in Fig. 5.1c, we modified the ramp rate such that the temperature of the reaction zone reached 500 °C from 100 °C in 5 s (and correspondingly, the temperature of sulfur source increased from 50 to 300 °C) followed by furnace cooling. The Change in the HTA setting clearly affected the phase of the film as evidenced in Fig. 5.2b. The pattern showed the evolution of two additional peaks (a very intense one at 14.94° and another at 43.94°) and disappearance of the peak at 18.09°, compared to pattern observed in Fig. 5.2a. The peak at 14.94° may be identified with the (002) plane of SnS_2 (JCPDS file: 1-89-3198) or (006) plane of $Cu_4Sn_7S_{16}$ (JCPDS file: 51-932), whereas the peak at 43.94° corresponds to the $(\bar{2}\bar{1}9)$ plane of anorthic Cu_2SnS_3. The clear presence of the secondary phases suggests that a high heating rate followed by furnace cooling in the given experimental conditions did not favor the formation of the phase pure kesterite CZTS.

Our experiments with the other HTA settings with rapid heating and rapid cooling (profile (iii) Fig. 5.1c), and normal heating at a rate of 8 °C/min followed by rapid cooling (profile (iv) Fig. 5.1c) yielded marginally different XRD patterns as presented in Figs. 5.2c and 5.2d. Compared to Fig. 5.2b, we found that the intensity of the peak at 28.54° has improved than that of the peak at 14.94°. Furthermore, the peak corresponding to Cu_2SnS_3 phase (observed at 43.94° in Fig. 5.2b) disappeared. Nevertheless, the eventual films are of mixed phases. For the temperature profile (v) in Fig. 5.1c in Configuration - I, wherein a heating rate of 8 °C/min followed by natural cooling was employed, two new peak at 22.60 and 24.44° appeared in addition to the peaks already observed in Fig. 5.2d. These peaks are identified with the (009) plane of $Cu_4Sn_7S_{16}$ phase and $(\bar{1}\bar{1}5)$ plane of anorthic Cu_2SnS_3 phase respectively, suggesting the growth of mixed phases.

It has been previously reported that the surface of the CZTS films deteriorates and decomposes at elevated temperature in the absence of sulfur [41, 203, 204] suggesting the forward reaction in Eq. (5.1).

$$Cu_2ZnSnS_4\ (s) \Leftrightarrow Cu_2S\ (s) + ZnS\ (s) + SnS\ (s) + \tfrac{1}{2}\, S_2\ (g);\ SnS\ (s) \Leftrightarrow SnS\ (g) \quad \ldots. \quad 5.1$$

A similar mechanism may be operational in the present case as evidenced from the growth of the films with mixed phases despite the varied temperature profiles employed in Configuration - I. It might be plausible that the sulfur vapor is more likely to condense at regions of lower temperature nearer to the sulfur source inside the quartz tube compared to its forward flow towards the reaction zone (at higher temperature). This, in turn, would create a sulfur-deficient environment in the reaction zone. Furthermore, EDS measurements revealed significant Zn loss in these films. The Zn/Sn ratio in all these samples was about 0.61 while the Cu/(Zn+Sn) ratio was ~1.30. These values are considerably different from those desired for photovoltaic applications, i.e., the ratio of Zn/Sn and Cu/(Zn+Sn) to be ~1.2 and 0.8, respectively [49, 62, 63, 205, 206]. The loss of Zn in the sample during sulfurization may be either due to the time taken by the sulfur to reach the sample or due to the loss of sulfur because of the condensation of the sulfur vapors at lower temperature.

5.1.2 Surface microstructure

Figure 5.3 shows representative FESEM surface and cross-sectional images of the films grown in Configuration - I with different annealing profiles. As expected, each of the profiles resulted in distinct features of the film microstructure. The film grown from two-step annealing (profile (i) in Fig. 5.1c) showed a porous structure and the film surface was covered with particulates of arbitrary sizes and shapes (Fig. 5.3a). Contrastingly, for the films grown by rapid heating and furnace cooling (profile (ii) in Fig. 5.1c) of the precursor film, a microstructure characterized by agglomeration of nanoscale particles is observed (Fig. 5.3b). Although, the grain growth has been reported to take place during rapid heating [37], the strong presence of SnS_2 might inhibit the growth of larger grains and might cause the cracks, as observed. A similar microstructure was observed for the films prepared by rapid heating followed by rapid cooling (profile (iii) in Fig. 5.1c) as noted from Fig. 5.3c. However, a compact microstructure albeit surface voids of arbitrary shapes and sizes (Fig. 5.3d) was observed when the films were grown by normal heating and rapid cooling (profile (iv) in Fig. 5.1c). It might be due to the diminishing of the SnS_2 phase as revealed from the corresponding XRD pattern. On the other hand, as the contribution of the SnS_2 phase further decreased as a consequence of normal heating and furnace cooling (profile (v) in Fig. 5.1c) of the precursor film, the number density of the surface voids increased resulting in a connected network of voids (Fig. 5.3e).

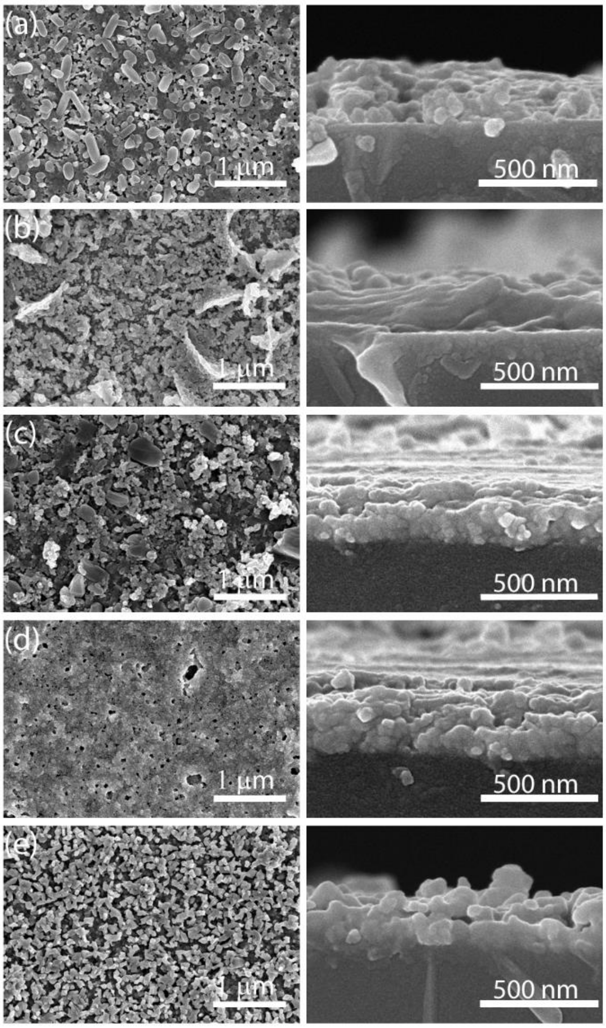

Fig. 5.3: Representative FESEM surface and corresponding cross sectional view of the films prepared by HTA via Configuration-I with (a) 2 step sulfurization for 60 min at each step, (b) Rapid heating and normal cooling, (c) Rapid heating and rapid cooling, (d) Normal heating and rapid cooling, (e) Normal heating and cooling. Normal heating and normal cooling refers to heating at the rate of 8 °C/min and furnace cooling.

5.2 CHARACTERIZATION OF FILMS GROWN VIA CONFIGURATION II

5.2.1 Determination of Phase

The above results show that although the HTA Configuration - I can be thought to be a simple and conventional one to implement, the amount of sulfur vapor at the reaction zone (i.e., precursor film at a temperature as high as 500 °C) remained, more likely, inefficient to yield phase pure kesterite films in spite of a variety of heating and cooling profiles. In order to overcome this issue, we have designed Configuration - II, wherein the reaction zone houses both sulfur flakes as well as the precursor film, as illustrated in Fig. 5.1b. The other HTA setting parameters including Ar flow rate, amount of sulfur flakes, and the heating and cooling profiles of the reaction zone remained the same. The typical XRD patterns of the films grown via

Configuration - II with different heating and cooling profiles are presented in Fig. 5.4. The XRD pattern of the film grown by two-step annealing (Fig. 5.4a) is characterized by an intense peak at 28.54° and minor peaks at 14.94, 32.99, 47.33 and 56.17°. As described earlier, the peak at 14.94° corresponds to the (002) plane of SnS_2 (JCPDS file: 1-89-3198) or (006) plane of $Cu_4Sn_7S_{16}$ (JCPDS file: 51-932). The peak at 32.99° may be identified with the reflections from (200) plane of CZTS. On the other hand, the peaks at 28.54, 47.33 and 56.17° can be attributed to either (112), (220) and (312) planes of CZTS, or (111), (220) and (311) plane of ZnS, or (111), (220) and (311) of cubic Cu_2SnS_3. This clearly indicates the presence of the secondary phases along with the CZTS phase. Similar XRD patterns (Fig. 5.4b and 5.4c) were obtained for the samples grown by rapid heating and normal cooling (profile (ii) in Fig. 5.1c), and by rapid heating and rapid cooling (profile (iii) in Fig. 5.1c), respectively, with appearance of an extra peak at 18.09° corresponding to $(\bar{1}\bar{1}3)$ plane of anorthic Cu_2SnS_3 phase and disappearance of the peak at 14.94° in Fig. 5.4c, suggesting the growth of films of mixed phases. On the other hand for the film grown by normal heating (rate of 8 °C/min) and rapid cooling, three additional peaks appeared at 27.12, 32.15 and 52.63°. The peak at 27.12 and 52.63° can be identified with reflections from (100) and (108) plane of CuS (JCPDS file: 1-1240) respectively, whereas the peak at 32.15° corresponds to (102) reflection of SnS_2 phase. However, when the heating rate was 8 °C/min followed by furnace cooling (profile (v) in Fig. 5.1c), all other peaks disappeared except the ones at 28.54, 47.33 and 56.17°, which may, respectively, correspond to the (112), (220) and (312) planes of CZTS, or (111), (220) and (311) plane of ZnS, or (111), (220) and (311) of cubic Cu_2SnS_3. As reported by many research groups, due to the analogous diffraction patterns of ZnS, Cu_2SnS_3, and CZTS phases, it may not be possible to establish the phase purity of the films by only by XRD measurements [49, 62, 63, 205, 206]. The Raman data have been required to substantiate the XRD results. The Raman spectrum of this film, shown in Fig. 5.5, is characterized by two intense peaks at 288 and 336 cm^{-1}. These two peaks matches well with the previously reported Raman spectral data [49, 62, 63, 205, 206] and correspond to the kesterite CZTS phase.

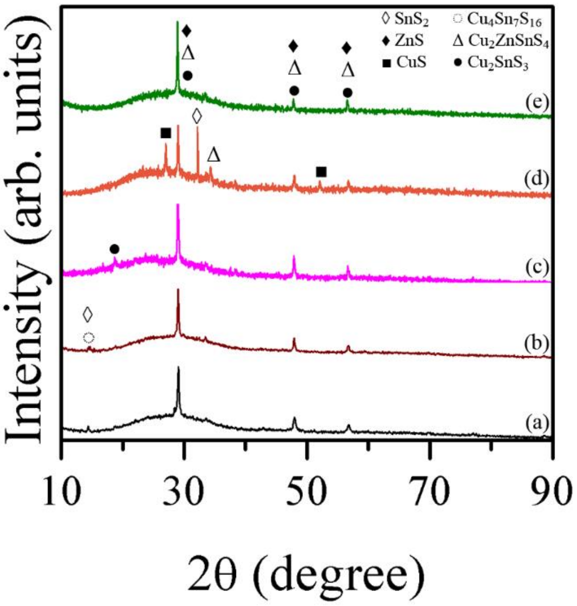

Fig. 5.4: Typical XRD pattern of the films prepared by HTA via Configuration-II with (a) two - step sulfurization for 60 min at each step, (b) Rapid heating and normal cooling, (c) Rapid heating and rapid cooling, (d) Normal heating and rapid cooling, (e) Normal heating and cooling. Normal heating and normal cooling refers to heating at the rate of 8 °C/min and furnace cooling.

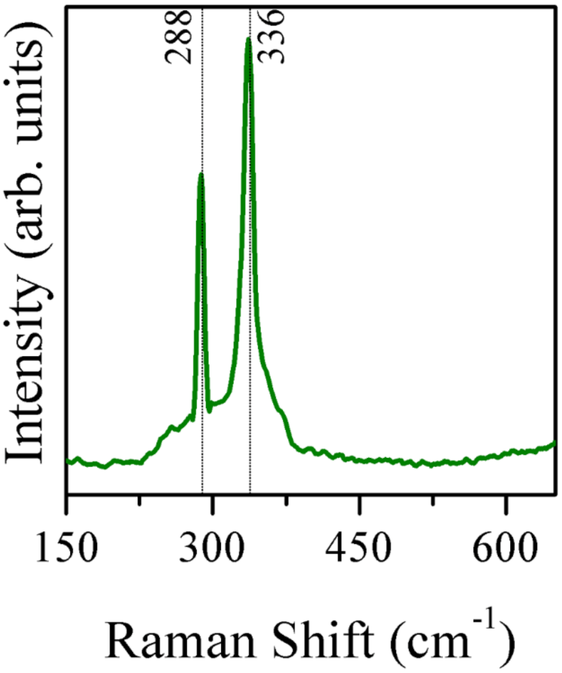

Fig. 5.5: Typical Raman spectrum of the film prepared by HTA via Configuration II with heating at the rate of 8 °C/min followed by furnace cooling. The temperature profile of the reaction zone is given as profile (v) in Fig. 5.1c.

5.2.2 Surface Morphology

Representative surface and cross-sectional electron micrographs of the films prepared in Configuration - II at different heating and cooling rates are presented in Fig. 5.6. It is found that for films grown by two-step annealing (Fig. 5.6a), or by rapid heating and slow cooling (Fig. 5.6b) and by rapid heating and rapid cooling (Fig. 5.6c) are characterized by a very porous microstructure. On the hand, a dense and smooth microstructure consisting of fine grains (Fig. 5.6d) is observed for the film grown by heating at 8 °C/min followed by rapid cooling. The grain structure dramatically changed, as evidenced in Fig. 5.6e, when normal heating (8 °C/min) and normal cooling was followed (the film was phase pure CZTS as confirmed by XRD and Raman measurements). The thickness of this film grown from a single dip scales about 200 nm, suggesting the requirement for multiple dips for the reasonable 1 μm thickness required for the photovoltaic device fabrication. Nevertheless, the compact microstructure without any visible cracks or pin-holes, a prerequisite for better efficiency, has been achieved. The results of further characterization including Hall measurement, X-ray photoelectron spectroscopy, UV-visible spectroscopy and photoresponse studies of this film, i.e., the one grown by heating at 8 °C/min followed by furnace cooling (profile (v) in Fig. 5.1c) have been reported previously [207]. The films were found to be of p-type having a bandgap of 1.44 eV, typical of CZTS thin films available in literature [49, 62, 63, 205,206] .

The results presented in the preceding paragraphs clearly shows that the HTA via Configuration - II yields the single phase CZTS thin films, most likely due to enhanced sulfur vapor flux facilitated by the geometry of the sulfurization. It may be noted that although the precursor film was placed in the crucible above the sulfur flakes, it did not completely cover the crucible implying significant escape of the sulfur vapor and thereby, suggesting a non-equilibrium HTA process. Nevertheless, the confinement of the vapor flux nearer to the reacting surface of the precursor film creating a sufficiently high partial pressure of sulfur is believed to prevent the decomposition reaction of the CZTS at elevated temperatures [41, 203, 204].

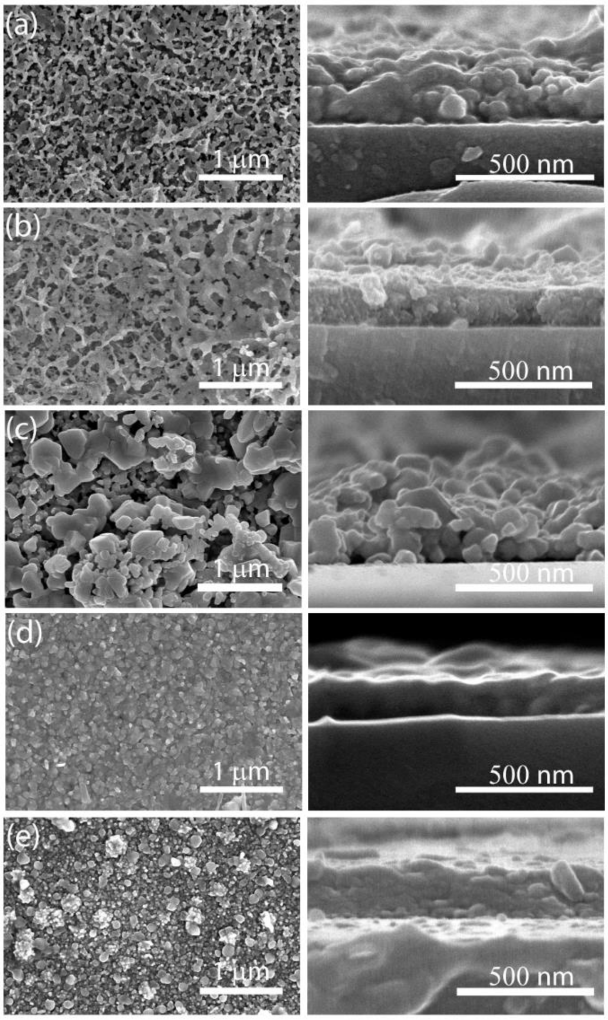

Fig. 5.6: Representative FESEM surface and corresponding cross sectional view of the films prepared by HTA via Configuration-II with (a) two - step sulfurization for 60 min at each step, (b) Rapid heating and normal cooling, (c) Rapid heating and rapid cooling, (d) Normal heating and rapid cooling, (e) Normal heating and cooling. Normal heating and normal cooling refers to heating at the rate of 8 °C/min and furnace cooling.

In summary, from the comparative investigation of the HTA settings including systematic variations in the ramp rate, sulfur source temperature and the reaction temperature, the influencing mechanisms of phase evolution are explained. The results elucidate the critical dependence of the HTA setting, in particular of the sulfur vapor flux constrained by the geometry of the placement of sulfur flakes, on the phase evolution of the films and highlight the promise of the approach including the proposed HTA strategy for reproducible growth of phase pure kesterite CZTS films. We find that configuration II offers a facile strategy to prepare phase pure CZTS films.

CHAPTER – 6

EFFECT OF PRECURSOR SOLUTION CONCENTRATION ON PROPERTIES OF CZTS FILMS

In the typical direct solution coating approach, depending upon the solubility product of cation and anion at a given temperature, and due to the constraints of limited availability of reacting species, the deposition rate asymptotically saturates [208]. The requirement of CZTS films of thickness > 1 μm for efficient photon absorption and subsequent, charge dissociation, is generally overcome by multiple dipping cycles followed by an eventual sulfurization [52, 88, 94, 95, 97, 209-212]. However, increased dipping cycles have been found to introduce voids, carbon contamination, poor crystallinity and possibly, spurious secondary phases in the eventual films [209] which are detrimental for photovoltaic performance. Despite the simplicity, low-cost and up-scalability potential of the approach, elaborate efforts for conformal deposition of micrometer thick phase-pure CZTS films from ethanol based solutions via dip-coating with minimum process steps, required to minimize the aforementioned issues are scarce. This chapter presents a detailed study of growth mechanism of phase pure CZTS thin films by a direct solution approach (via dip-coating) from ethanol based true solutions of common salts of $CuCl_2$, $SnCl_2$, $ZnCl_2$ and TAA.

As outlined in the previous chapters, we have prepared the films without using any complexing/chelating agent. The total volume of the precursor solution was kept constant (80 ml), and the concentration of the cations and anions was varied to reasonably illustrate the concentration driven evolution of film properties including phase and microstructure. The HTA was carried out via configuration II, as discussed in Chapter 5.

6.1 EFFECT OF PRECURSOR CONCENTRATION

6.1.1 Films grown using 0.25M Cu concentration

Figure 6.1a shows a typical XRD pattern of the sulfurized film coated from a single dip in the precursor solution having 0.25 M $CuCl_2$. The pattern is characterized by three sharp peaks at 28.54°, 47.34°, and 56.83°, suggesting well-crystallized nature of the films. Considering that some of the binary (i.e., ZnS) and ternary (i.e., Cu_2SnS_3) compounds have very similar lattice parameters or analogous pattern features compared to CZTS, identification of the phase of the films is rather difficult on the basis of XRD pattern alone [31-33]. For instance, these three peaks can be attributed respectively to either (1 1 2), (2 2 0) and (3 1 2) planes of CZTS (JCPDS file: 26-0575), or (111), (220) and (311) peak of ZnS (JCPDS file: 3-65-5476), or (111), (220) and (311) of cubic Cu_2SnS_3 (JCPDS file: 1-89-2877). Reportedly, Raman measurements have been required, in addition to the XRD patterns, to establish the phase purity of the films [213,214]. The Raman spectrum of the film (Fig. 6.1b) showed an intense peak at 336 cm^{-1} and a small hump at 288 cm^{-1} which correspond to the kesterite CZTS phase, consistent with the previously reported Raman spectral data [183,215].

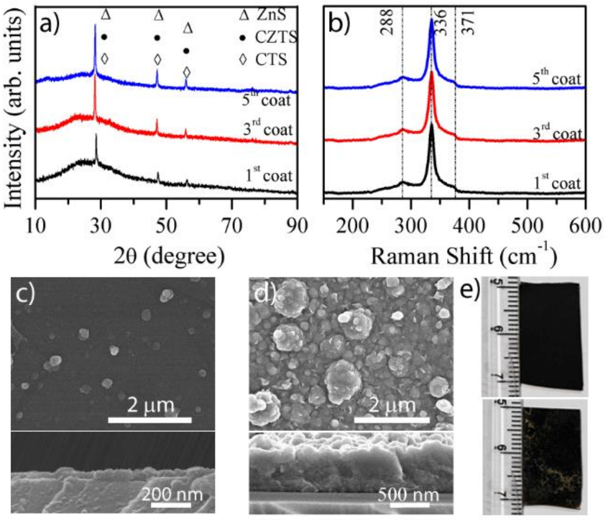

Fig. 6.1: Typical (a) XRD patterns and (b) Raman spectra of film deposited using 0.25M $CuCl_2$ solution with one, three and five coats followed by sulfurization 500 °C. The main peaks in both the panels are marked; Corresponding representative surface and cross-sectional FESEM images of the films of one coat (c) and five coats (d); (e) Photographs of the as-deposited films with 5 dip cycles (top) and 6 dip cycles (bottom) showing a very patchy appearance after the 6th dip cycle.

Although we were successful in preparing phase pure CZTS thin films using non-toxic solutions, the films were extremely thin (~50 nm) as evidenced from the cross-sectional FESEM image (Fig. 6.1c). Thus, multiple dipping cycles were necessitated in order to improve the thickness of the films. In fact, after five dipping cycles followed by sulfurization, films of thickness of ~600 nm (Fig. 6.1d) were obtained. The XRD and Raman measurements (as shown in Figs. 6.1a and b) confirmed the kesterite phase of the films. These films exhibited a bandgap of ~1.48 eV, as determined from the analysis of the UV-visible reflectance and transmittance data (Fig.6.2). However, further attempt to increase thickness by another dipping cycle met with limited success. After the sixth dipping cycle, the as-deposited film had a very patchy appearance (Fig. 6.1e), possibly due to non-uniform deposition and/or partial dissolution of the film.

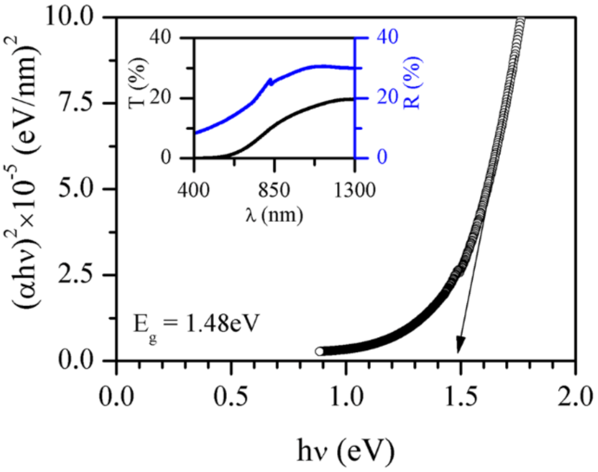

Fig. 6.2: Tauc plot of $(\alpha h\nu)^2$ vs hν and the typical reflectance and transmittance curves (inset) for the phase pure CZTS films grown from solutions using 0.25M $CuCl_2$ solution with five dipping cycle and sulfurized with 1 g of sulfur at 500 °C.

6.1.2 Films grown using 0.5M Cu concentration

As discussed earlier, unlike the typical vacuum based techniques wherein the supply of the depositing species is unlimited, in the solution based approaches the absolute amount of the reacting species is limited by the amount of the starting reagents. The molar concentration of the cationic and anionic solutions in this approach is a key process parameter in that it directly contributes to the control of nucleation of solid phase at the initial stage and subsequently to the crystal lattice imperfections and crystallinity [88, 211, 212]. Thus, a higher molarity of the cation and anion salts corresponds to increased availability of cations and anions, which may possibly improve thickness of the deposited film in a single dipping cycle [209, 210]. Accordingly, we have increased the concentration of the salts and evaluated the properties of the films. Figure 6.3a shows the XRD pattern of a film prepared by a single-dip coating from the precursor solution containing 0.5M $CuCl_2$. Apparently, the pattern is very similar to the ones observed for films grown from solution with lower concentration of 0.25 M $CuCl_2$ (shown in Fig. 6.1a). However, the surface of the films (Fig. 6.3b) was found to be different from those of the films prepared with lower concentration of reagents and was densely covered by crystallites. On the other hand, thickness of the films was improved to ~150 nm (Fig. 6.3b) as expected. To further increase the thickness of the films, we have increased the number of dipping cycles. However, films prepared with two dipping cycles followed by sulfurization clearly showed the presence of secondary phases in the form of CTS (JCPDS file: 51-932), SnS_2 (JCPDS file: 1-89-3198) and SnS (JCPDS file: 1-89-2755). This is also corroborated from the corresponding Raman spectra as shown in Fig. 6.4.

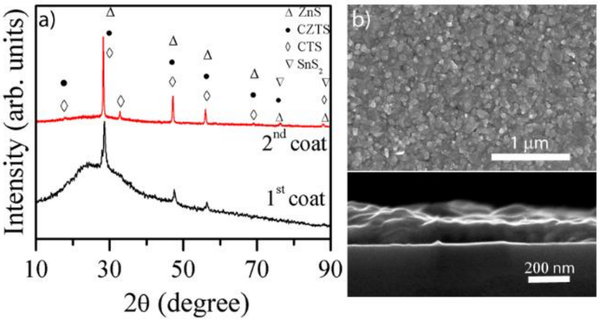

Fig. 6.3: (a) Typical XRD patterns of the film deposited with one and two dipping cycles, and (b) Surface and cross sectional FESEM images of the film deposited using 0.5M $CuCl_2$ solution by a single dip.

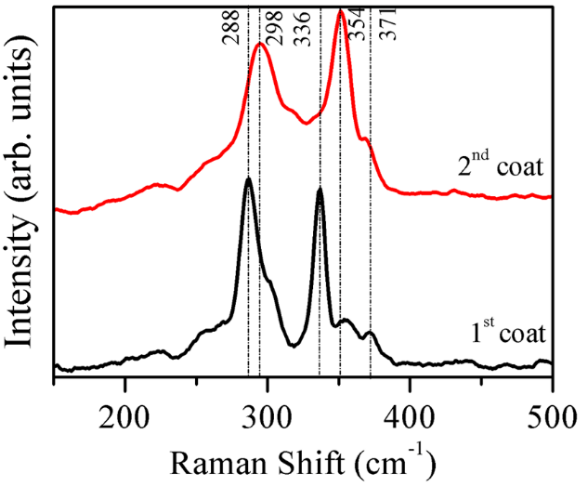

Fig. 6.4: Typical RAMAN spectrum of the film deposited using 0.5M $CuCl_2$ solution with one and two dipping cycles

6.1.3 Films grown using 0.75M Cu concentration

The results of the attempts to prepare thicker and phase pure CZTS films using higher concentration of the solution were similar to the case presented in Fig. 6.3. Figure 6.5a shows the XRD pattern of the film growing by a single dip coating from solutions with 0.75 M $CuCl_2$. The pattern was similar to that observed for the single dip-coated film from 0.5 M $CuCl_2$ solution (Fig. 6.3a) and from 0.25 M $CuCl_2$ solution (Fig. 6.1a). The thickness of the film as assessed from the cross-sectional SEM image (inset to Fig. 6.5b) was about 180 nm. For the film grown with two dipping cycles, the XRD pattern clearly showed the presence of secondary phases. For example, additional peaks, not corresponding to the kesterite CZTS phase, at 2θ values of 14.94°, 32.53°, 38.69°, 71.84° and 87.71° appeared in the pattern. The peak at 14.94° is identified with (002) plane of SnS_2 (JCPDS file: 1-89-3198) or (006) plane of $Cu_4Sn_7S_{16}$

(JCPDS file: 51-932), whereas the peaks at 32.53, 38.69, 71.84 and 87.71° are attributed to the$(0\bar{4}2)$ plane of Cu_2SnS_3 (JCPDS file: 27-198), (1112) plane of $Cu_4Sn_7S_{16}$ (JCPDS file: 51-932), (205) plane of SnS_2 (JCPDS file: 1-89-3198) and (422) plane of SnS (JCPDS file: 1-89-2755), respectively. This is further supported by the Raman spectra (Fig. 6.6).

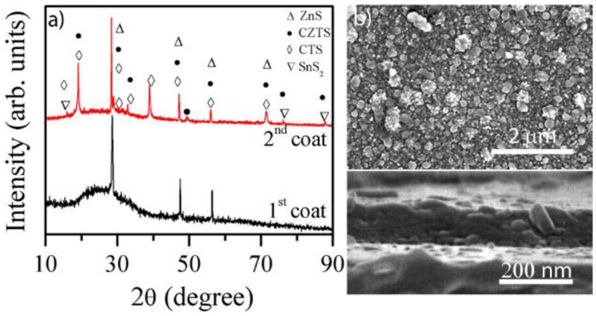

Fig. 6.5: (a) Typical XRD patterns of the film deposited with one and two dipping cycles, and (b) Surface and cross sectional FESEM images of the film deposited using 0.75M $CuCl_2$ solution by a single dip.

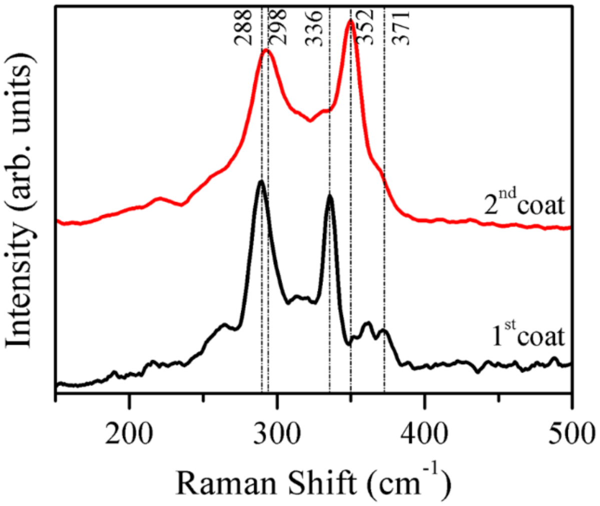

Fig. 6.6: Typical RAMAN spectrum of the film deposited using 0.75M $CuCl_2$ solution with one and two dipping cycles

The results presented in the preceding sections reveal that although the single coating of films from solutions with 0.5 M and 0.75 M $CuCl_2$ yielded phase pure kesterite CZTS, the films were very thin and another coating resulted in growth of undesirable secondary phases.

Figure 6.7 shows the variation of the thickness of the sulfurized films grown by single-dip coating from solutions of varying reagent concentration. As inferred from the figure, it is expected that a significantly thicker film can be prepared by single coat from a solution with higher concentration (i.e., with 1.0 M $CuCl_2$).

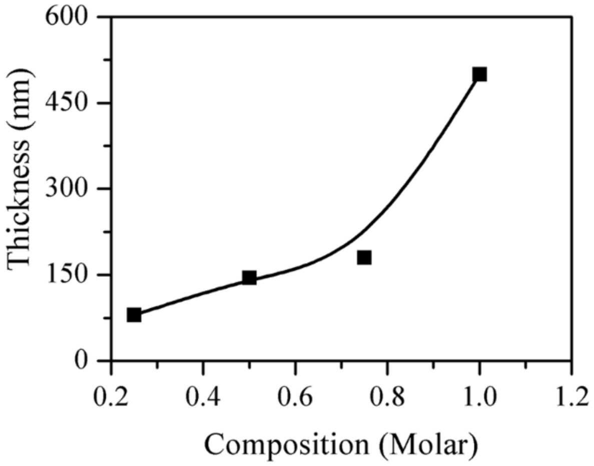

Fig. 6.7: The variation of the thickness of the sulfurized films grown by single-dip coating from solutions of varying reagent molar concentrations.

6.1.4 Films grown using 1M Cu concentration

Figure 6.8a shows the surface and cross-sectional FESEM images of the film grown from the precursor solution containing 1.0 M $CuCl_2$ and sulfurized at 500 °C for 60 min. The images suggest the growth of films of thickness >500 nm, consistent with the linear variation predicted in Fig. 6.7. However, analysis of the phase of the films by both XRD and Raman measurements (shown in Figs. 6.8b and 6.8c, respectively) revealed the presence of the secondary phases. For instance, in the XRD pattern, the peak with the highest intensity (i.e., at 14.94°) is identified with the (002) plane of SnS_2 (JCPDS file: 1-89-3198) or the (006) plane of $Cu_4Sn_7S_{16}$ (JCPDS file: 51-932). The presence of the Raman peaks at 292, 344 and 495 cm^{-1} along with a shoulder at 333 cm^{-1} confirmed the presence of secondary phases along with the CZTS phase. It may be highlighted that single phase CZTS films with single dip-coating were obtained from solutions with lower concentration of reagents (for example with 0.25, 0.5 and 0.75 M $CuCl_2$) whereas a similar processing with 1.0 M $CuCl_2$ solution yielded phase impure film. This contrast might stem from the decomposition of CZTS at elevated temperature in view of the increased mass/volume of the as-deposited film and the insufficient sulfur vapor limited by the initial sulfur amount placed in the sulfurization chamber [35-37]. The role of sulfurization duration is ruled out by performing additional experiments of sulfurization of 120 min. Despite such a long heat treatment, the films were of multiple phases as indicated by the XRD and Raman measurements shown in Fig. 6.9. Sufficiently high partial pressure of sulfur and SnS are suggested to inhibit potential decomposition reaction of CZTS at higher temperature through a reversible reaction at the film surface [35-37]. Hence it is believed that in the present experimental setting, although further increase in the molarity would yield higher film thickness, phase purity of the films would remain elusive, and hence, the sulfurization ambience in the present case should be suitably modified for a thicker as-deposited precursor film.

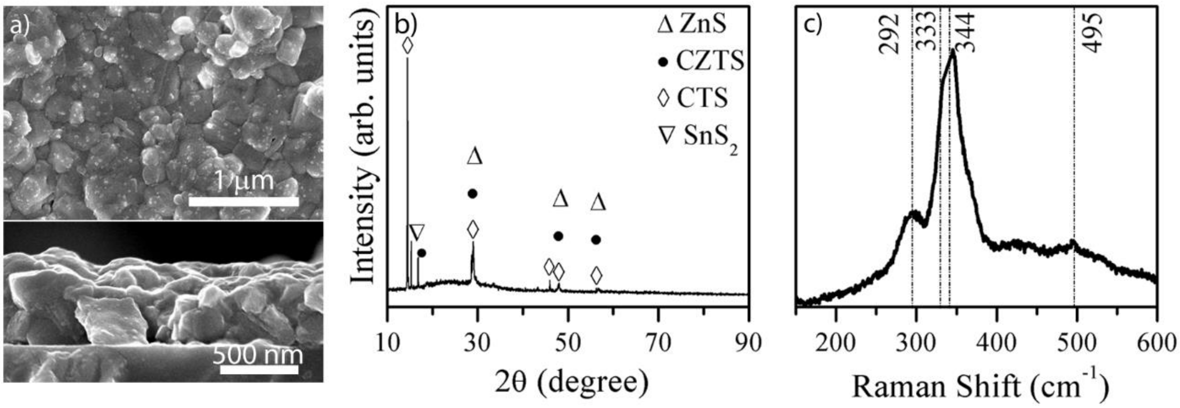

Fig. 6.8: (a) Surface and cross-sectional FESEM image of the film deposited using 1M $CuCl_2$ solution with single dipping cycle sulfurized for 60 min using 1 g sulfur. The corresponding XRD pattern (b) and Raman spectrum (c) clearly revealed the presence of secondary phases.

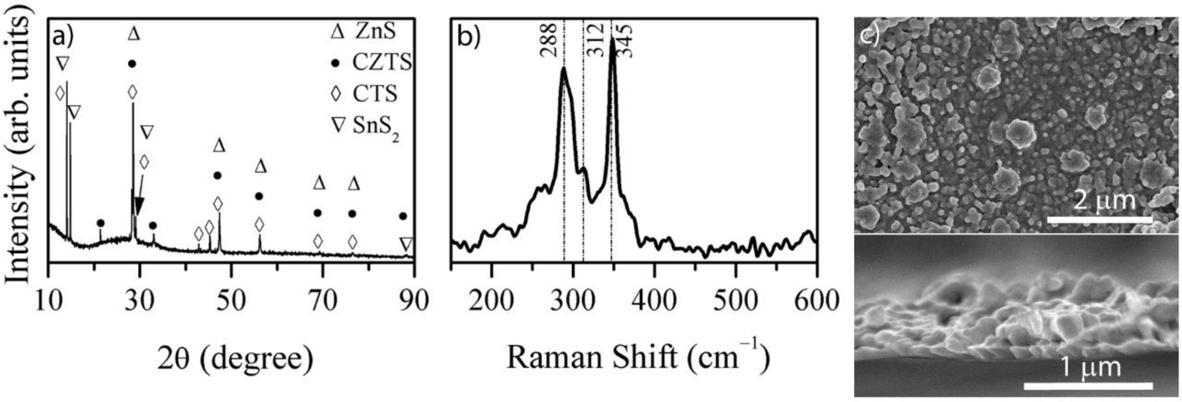

Fig 6.9: The corresponding XRD pattern (a) and Raman spectrum (b) clearly revealed the presence of secondary phases. (c) Surface and cross-sectional FESEM image of the film deposited using 1M $CuCl_2$ solution with single dipping cycle sulfurized for 120 min using 1g sulfur.

6.1.4.1 Impact of sulfur amount during sulfurization

Following the observations, as discussed in the above paragraph, we have prepared the films in identical process steps, but with increased amount of sulfur placed in the crucible during the sulfurization treatment. As expected, experiments with reduced amount of sulfur (i.e., 0.5 g) yielded clear signatures of impurity phases as indicated in Fig. 6.10.

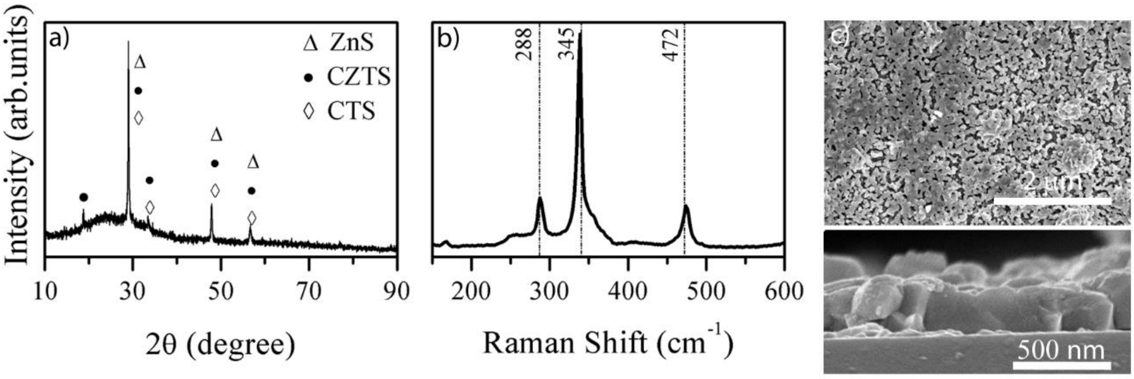

Fig. 6.10: The corresponding XRD pattern (a) and Raman spectrum (b) clearly revealed the presence of secondary phases. (c) Surface and cross-sectional FESEM image of the film deposited using 1M $CuCl_2$ solution with single dipping cycle sulfurized for 60 min using 0.5g sulfur.

On the other hand, the presence of additional amount of sulfur led to the formation of phase pure CZTS films. Figure 6.11 presents typical XRD patterns and Raman spectra, along with corresponding SEM micrographs, of the films sulfurized with 2 and 3 g of sulfur flakes placed in the crucible. The intense Bragg peaks at about 28.54, 32.95, 47.34, and 56.83° in the XRD patterns, supported by the Raman peaks at ~336 and 288 cm^{-1} clearly suggest the formation of the kesterite CZTS films [183,215]. The film prepared with 2 g of sulfur is of about 500 nm thick (Fig. 6.11c) and the surface of the film is characterized by crystallites of average size of about 120 nm along with a few occasional pin holes. Interestingly, when the sulfur amount was increased to 3 g during the sulfurization process, the pin holes disappeared leading to a dense microstructure, albeit reduced average crystallite size. In view of the importance of larger crystallites in the solar cell technology, we proceeded further to a double coating followed by sulfurization with 2 g sulfur in the crucible. It is worth mentioning that, as evidenced from the cross-sectional micrographs (Figs. 6.11c and 6.11d), the films had a bi-layered structure. A variety of multi-layered morphologies have been reported for CZTS based thin films [77, 216-218]. Typically, impurity-rich bottom fine-grained layer is device performance limiting and hence, is undesirable. As we show in the followings, a double-dip coating apparently alleviated this problem.

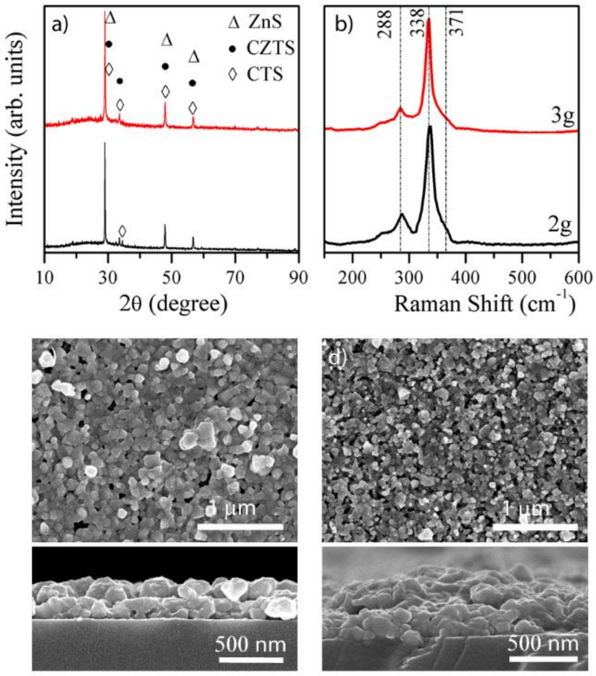

Fig. 6.11: Typical (a) XRD patterns and (b) Raman spectra of the films deposited using 1M $CuCl_2$ solution in a single dip and sulfurized with 2 and 3 g sulfur in the crucible during sulfurization; Corresponding surface and cross-sectional FESEM image of films sulfurized with 2 and 3 g of sulfur.

6.1.4.2 Increasing dipping cycle to improve thickness

Figures 6.12a and b present the typical XRD pattern and the Raman spectrum, respectively, of the double dip coated films from the solution with 1.0 M $CuCl_2$. The curves are remarkably similar to the ones corresponding to the single-coat films (Fig. 6.11a and b) suggesting phase purity of the films. Figure 6.12c shows the representative surface and cross-sectional FESEM images of the film. With the second dipping, thickness of the films was greatly improved to >800 nm. Furthermore, compared to the film dipped only once, the CZTS film resulted from dipping twice is composed of larger and densely packed grains. More importantly, the films showed a conformal deposition of the films, unlike the films grown by a single dipping cycle (Fig. 6.11c). This implies that the second coating not only increased the thickness of the film but also improved the quality and average grain size of the films. The larger size of the grain is an important factor as it affects the device performance because fine grains with more grain boundaries leads to recombination and reduces the collection of current [209,219,220].

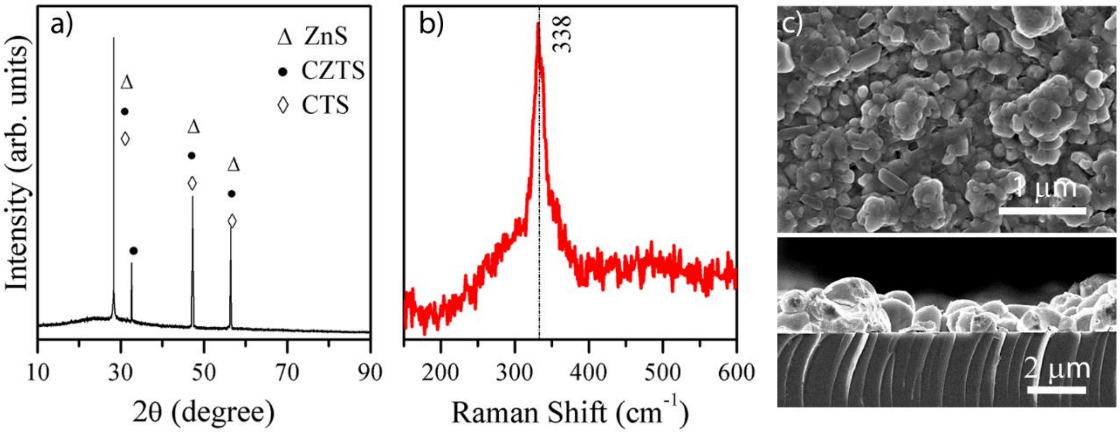

Fig. 6.12: (a) XRD pattern and (b) Raman spectrum of the film deposited with two dipping from solution having 1M $CuCl_2$ and sulfurized with 2 g of sulfur; (c) Corresponding surface and cross-sectional FESEM image of the film

6.1.4.3 Optical bandgap

Further characterization of this phase pure and sub-micrometer thick CZTS film (obtained by double dip-coating from 1.0 M solution and sulfurized with 2 g of sulfur for 60 min) was carried out. The bandgap of the films was estimated by analyzing the optical absorption data in the form of Tauc plots of the variation of $(\alpha h\nu)^2$ versus photon energy hν, where α is the absorption coefficient, as shown in Figure 6.13. The value for α was estimated from the UV-visible-NIR reflectance (*R*) and transmittance (*T*) curves (Inset of Fig. 6.13) of the sample using the formula $\alpha = (1/d)\ \ln\,[(1-R)^2/T]$ for the film of thickness *d*. By extrapolating the linear portion of the $(\alpha h\nu)^2$ vs hν curve, the bandgap was found to be 1.42 eV, which is similar to the values reported by several earlier researchers [43,80,187].

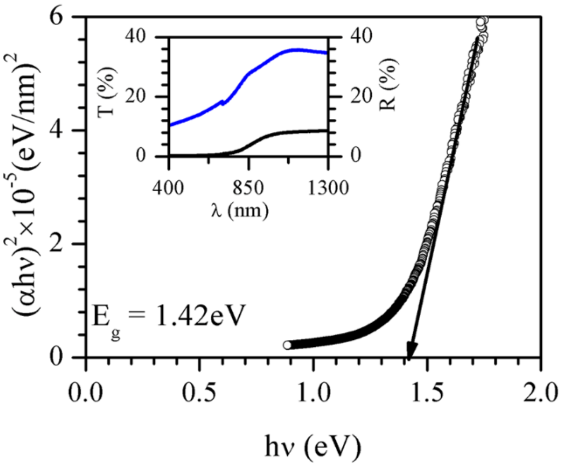

Fig. 6.13: Tauc plot of $(\alpha h\nu)^2$ vs hν and the typical reflectance and transmittance curves (inset) for the phase pure CZTS films grown from solutions using 1M $CuCl_2$ solution with two dipping cycle and sulfurized with 2 g of sulfur at 500 °C.

6.1.4.4 Photoresponse properties

The photoresponse behavior of the films are summarized in Fig. 6.14. The I–V characteristic curves of single-dip coated CZTS thin films were almost linear and remained the same for both dark and white light (AM 1.5G, 100 mW/cm^2) illumination, indicating negligible photoresponse of the films. The observed poor performance may be understood in terms of dissociation followed by rapid recombination of the electron-hole pairs created due to white light illumination [187,221,222]. On the other hand, the double-dip coated films showed huge increase in current under illumination compared to that in dark, suggestive of a promising photoresponse performance, as expected from an absorber layer to be potentially used in photovoltaic devices (Fig. 6.14b). A mechanism based on thermionic emission associated with the two back-to-back Schottky junctions is being proposed to explain the observed photoresponse behavior of the double-dip coated CZTS thin films [195-197]. In view of the difference in the work function of Al (Φ_{Al} = 4.06 - 4.26 eV) [223] and the Fermi level of CZTS (E_F = 4.5 eV) [224], shifting of the levels leading to formation of Schottky junctions of Al and CZTS is expected when Al is deposited on the films. As a result, a built-in field is ensued across the interfaces due to band bending, as shown in Fig. 6.14c. In the dark condition, when a bias is applied, of the two Al/CZTS junctions, one gets forward biased while the other one is reverse biased. Assuming that the barrier heights at both contacts remain the same, a symmetric *V-I* (in first and third quadrant) is followed, as observed. For the case of white light illumination, electron-hole pairs are created due to absorption of photons with energy higher than the bandgap of the CZTS film (Fig. 6.14d). These additional carriers (i.e., photo-carriers) cause the split of the Fermi level into quasi-Fermi levels and consequently, affect the barrier heights and the carrier transport dynamics. As reported earlier [196] lowering of the barrier height favors a higher current density.

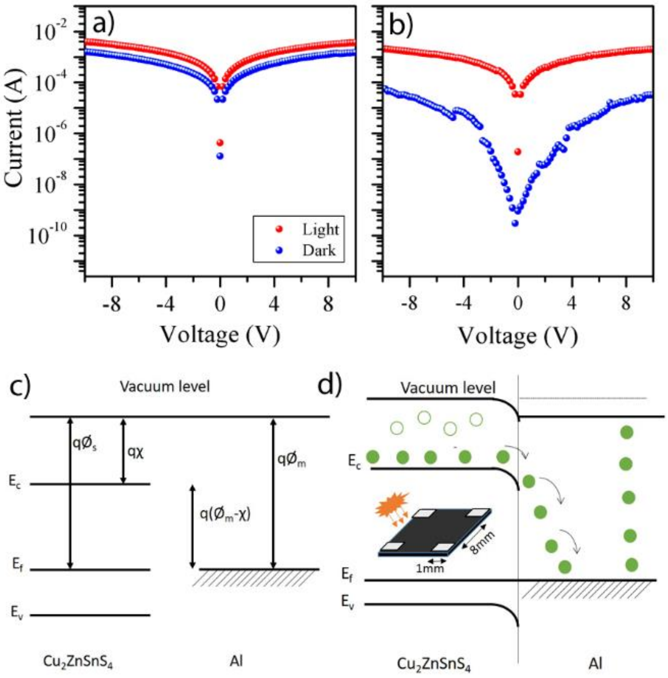

Fig. 6.14: Voltage - current characteristics under dark and white light illumination (100 mW/cm^2) of the phase pure CZTS film based device grown from solutions using 1M CuCl2 solution and sulfurized with 2 g of sulfur at 500 °C with (a) one dipping cycle and (b) two dipping cycles. Schematic representation of energy band diagram expected for CZTS and Al junction (c) in dark and (d) under white light illumination.

6.2 ANALYSIS OF CATION ORDER-DISORDER

It may be noted that in addition to establishing the phase purity of the samples, the Raman measurements have been used in literature to assess the Cu-Zn cationic disorder in the CZTS films [225]. Due to the smaller chemical and ionic size difference between the Cu$^+$ and Zn^{2+}, the Cu$_{Zn}$ and Zn$_{Cu}$ antisites are spontaneously formed and represent the dominant point defects in the CZTS films [27,226,227] In the Raman spectrum, the intensity of the m$_{2A}$ (~288 cm^{-1}) and m$_{3A}$ (~304 cm^{-1}) peaks have been correlated with the degree of disordering in the lattice. In particular, higher the ratio of the m$_{2A}$ and m$_{3A}$ peak intensities (Q), the more ordered is the film [225]. Correspondingly, we have deconvoluted the Raman spectra of selected phase pure samples and calculated the intensity ratio Q, which is summarized in Fig. 6.15. It is seen that Q remained fairly high around 2.5 for the films single dip coated from solutions with 0.5 and 0.75 M followed by annealing at 500 °C for 60 min with 1 g sulfur. However, for the phase-pure films grown from 1 M precursor solution (single and double dip coated and annealed at 500 °C for 60 min with 2 g sulfur), Q decreased considerably, suggesting the increase in the disorder in the films with increasing thickness.

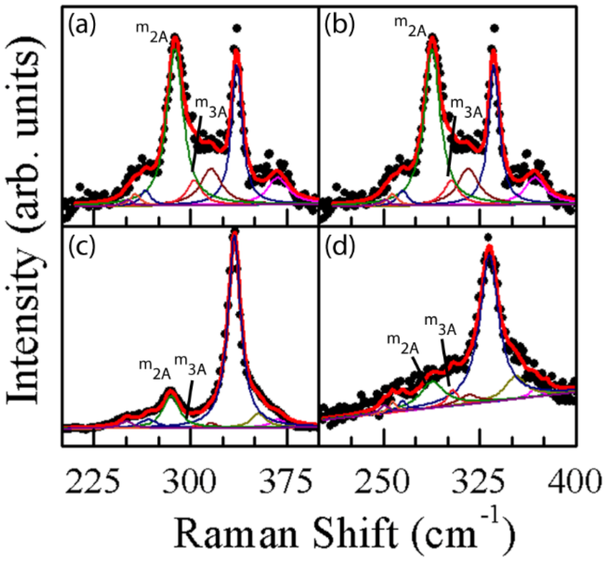

Fig. 6.15: The deconvoluted Raman spectra of the films grown by (a) single dip from 0.5 M solution and annealed for 60 min with 1 g sulfur, (b) single dip from 0.75 M solution and annealed for 60 min with 1 g sulfur, (c) single dip from 1 M solution and annealed for 60 min with 2 g sulfur, (d) double dip from 1 M solution and annealed for 60 min with 2 g sulfur. The annealing temperature was 500 °C for all cases.

Considering the typical CZTS based solar cell structure, we have separately prepared films from precursor solutions of different concentrations on sputter-deposited Mo films and examined the difference in the results, if any, compared to those discussed above. Figure 6.16 summarizes the results by depicting typical XRD, Raman and FESEM (surface and cross-sectional) images of various samples grown on Mo/glass. Similar to the results shown in Fig. 6.5 and Fig. 6.6, the film grown on Mo/glass from the solutions with 0.75 M $CuCl_2$ by a single dip (panel (i), Fig. 6.16) is phase-pure in nature with thickness of ~180 nm while that with two dipping cycles (panel (ii), Fig. 6.16) showed the presence of impurity phases. When the concentration was increased to 1 M (panel (iii), Fig. 6.16), the thickness of the film expectedly increased; however, secondary phases were observed in the film grown by a single dip followed by sulfurization at 500 °C for 60 min with 1g sulfur. The results are very similar to those obtained for the films grown on glass substrates (Fig. 6.8). However, films grown in identical conditions, but sulfurized with 2 g sulfur at 500 °C for 60 min (panel (iv), Fig. 6.16) were found to be phase pure, similar to the results obtained for samples grown on glass substrates (Fig. 6.11). To further improve the thickness of these films, dipping cycle was repeated twice. The double dip coated films from 1 M precursor solution and annealed for 60 min with 2 g sulfur at 500 °C showed only kesterite phase, similar to the ones grown on glass substrates (Fig. 6.12). The results thus shows that the growth pattern of the films on Mo/glass substrates remained the same as that of the films on glass substrates and highlights how the precursor concentration and the amount of sulfur vapor during post-deposition heat treatment critically affected the reaction pathway and the morphology of the eventual films of sub-micrometer thickness.

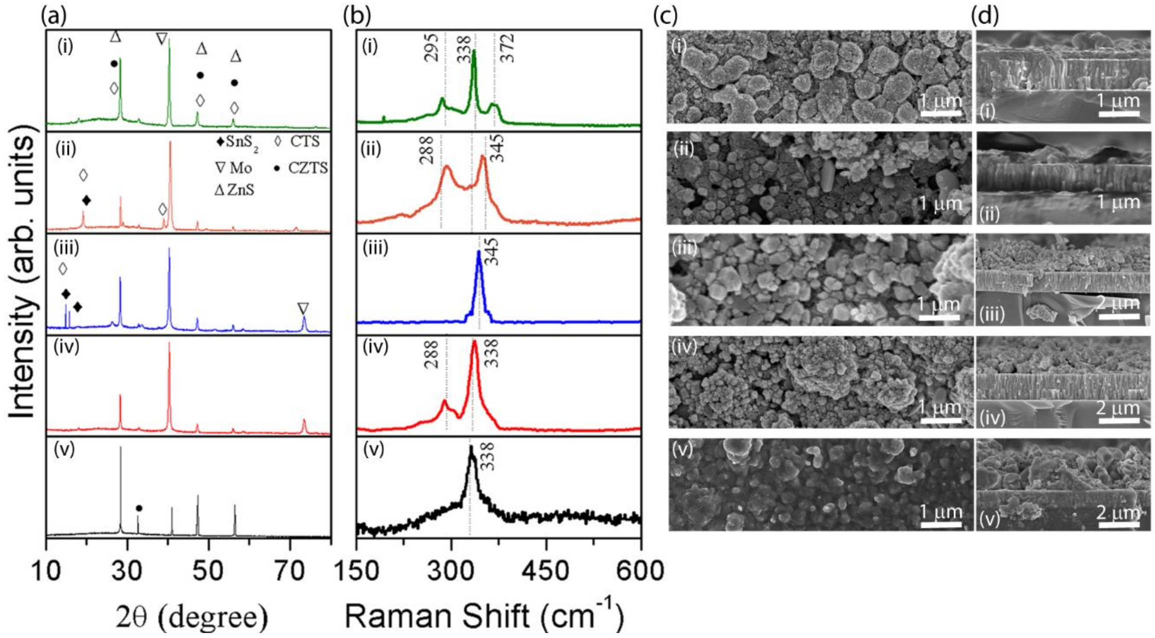

Fig. 6.16: Typical (a) XRD patterns, (b) Raman spectra, (c) FESEM surface and (d) cross-sectional images of the films grown from precursor solutions of different concentrations on Mo coated glass slides. (i) single coat from 0.75 M precursor solution (annealed for 60 min with 1 g sulfur), (ii) double coat from 0.75 M precursor solution (annealed for 60 min with 1 g sulfur), (iii) single coat from 1 M precursor solution (annealed for 60 min with 1 g sulfur), (iv) single coat from 1 M precursor solution (annealed for 60 min with 2 g sulfur), (v) double coat from 1 M precursor solution (annealed for 60 min with 2 g sulfur). The annealing temperature was 500 °C for all cases.

6.3 IMPACT OF SULFURIZATION TEMPERATURE

6.3.1 Determination of phase

In order to study whether sulfurization at a higher temperature can yield larger grains, we have prepared the films by double coating using 1M $CuCl_2$ solutions and sulfurized at 525, 550 and 575 °C. Figure 6.17a shows the typical XRD pattern of the sulfurized film having 1M $CuCl_2$ sulfurized at 525, 550 and 575 °C. It can be seen that all the XRD pattern contains diffraction peaks at $2\theta = 28.54°$, 47.34°, and 56.83° can be attributed to either (112), (220) and (312) planes of Cu_2ZnSnS_4 (JCPDS file: 26-0575), or (111), (220) and (311) peak of ZnS (JCPDS file: 3-65-5476), or (111), (220) and (311) of cubic Cu_2SnS_3 (JCPDS file: 1-89-2877) respectively. The Raman measurements showed a strong peak at 338 cm^{-1} in Fig. 6.17b, which is consistent with the previously reported CZTS Raman spectral data [214,215].

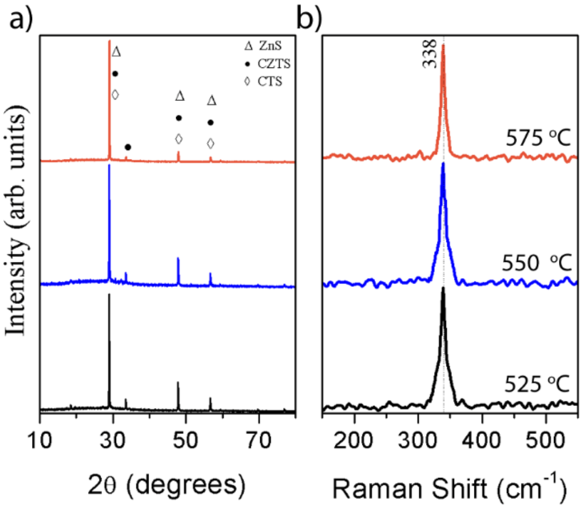

Fig. 6.17: Typical (a) XRD patterns and (b) Raman spectra of film sulfurized at various temperatures ranging from 525 to 575 °C. The main peaks in both the panels are marked

6.3.2 Surface microstructures: Grain growth

Figure 6.18 shows representative cross-section and surface FE-SEM images of CZTS films prepared by double coating using 1M $CuCl_2$ solutions and sulfurized at different temperatures wherein a uniform dense microstructure was observed. The cross-sectional images of CZTS film confirm the thickness of the films to be about 850 nm. It should be noticed that the increase in temperature also increased the grain size of the films. The larger size of the grain is an important factor as it affects the device performance because fine grains with more grain boundaries leads to recombination and reduces the collection of current [209,219,220].

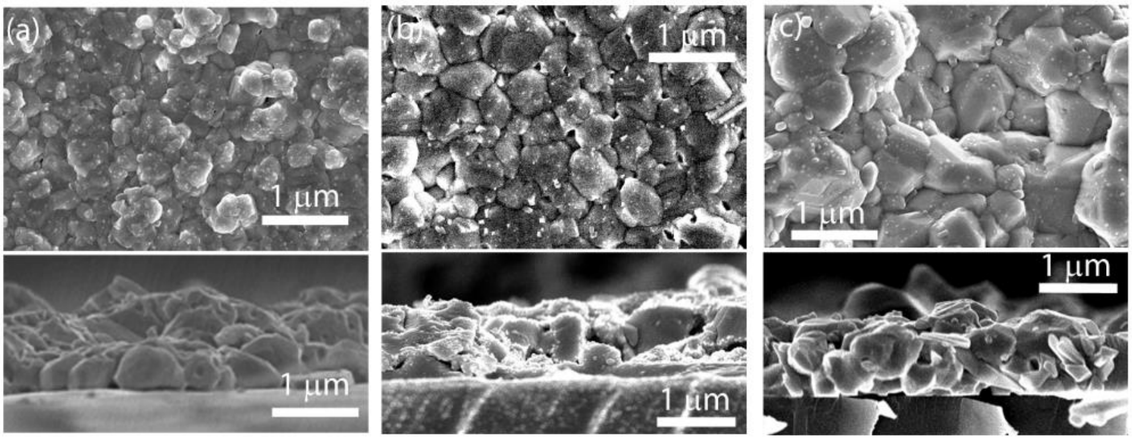

Fig. 6.18: Representative surface and corresponding cross-sectional FE-SEM images of CZTS films sulfurized at a) 525 ºC, b) 550 ºC and c) 575 ºC

6.3.3 Optical bandgap

As described in the experimental section, optical bandgap of the above films was determined from the Tauc plots of $(\alpha h\nu)^2$ vs photon energy $h\nu$, where α is the absorption coefficient. The optical bandgap E_g of the films sulfurized at various temperatures in the range of 525 - 575 °C remained the same at 1.42 eV, as shown in Fig. 6.19a. The observed value of the bandgap of the CZTS films is similar to the values reported by several earlier researchers [43,80,187].

6.3.4 Electrical properties

The results of the Hall measurement, summarized in Table 6.1, revealed the p-type conductivity of the above sample. The obtained values of carrier concentration, resistivity and Hall mobility are similar to the ones reported in literature [192]. In CZTS films, the electrical properties of the CZTS films are reportedly governed by the native defects and are strongly influenced by the processing of the films. In particular, the high carrier concentration in CZTS films has been attributed to the Cu-poor and Zn-rich composition.

Table 6.1: Summary of the results of Hall measurement of films prepared by double coating using 1M $CuCl_2$ solutions and sulfurized at different temperatures

	500 °C	**525 °C**	**550 °C**	**575 °C**
ρ (Ω-cm)	0.870	0.699	0.638	0.425
R_H (cm^3/C)	0.838	0.675	0.616	0.597
n (cm^{-3})	7.46×10^{18}	9.26×10^{18}	10.15×10^{18}	10.47×10^{18}
μ (cm^{2}V^{-1}s^{-1})	0.963	0.966	0.966	1.406

The photoresponse behavior of the films are summarized in Fig. 6.19b. The relatively inferior performance of the film sulfurized at 500 °C (also shown in Fig. 6.14) may be understood in terms of dissociation followed by rapid recombination of the electron-hole pairs created due to white light (AM 1.5G, 100 mW/cm^2) illumination.[196] On the other hand, huge increase in current under illumination compared to that in dark with increase in the sulfurization temperature was observed, suggesting a promising photoresponse performance, as expected from an absorber layer to be potentially used in photovoltaic devices (Fig. 6.19b).

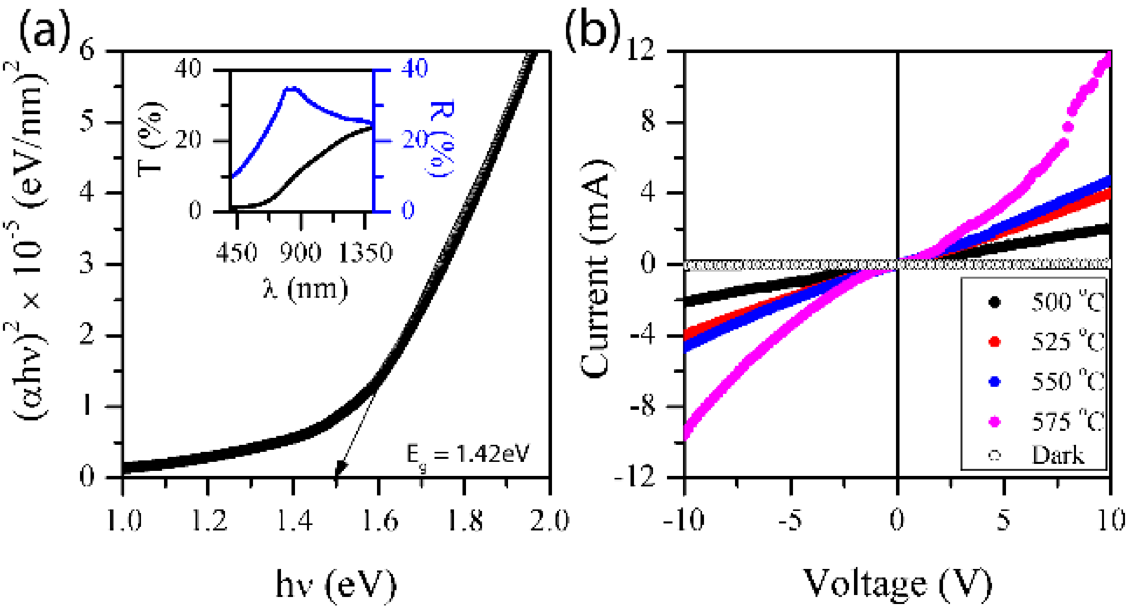

Fig. 6.19: (a) Optical bandgap and UV-Vis transmission spectra (inset) of CZTS thin films sulfurized at 575 °C and (b) Voltage - current characteristics under dark and light illumination of the phase pure CZTS film sulfurized at different temperatures.

In summary, we have presented a detailed study of growth mechanism of phase pure sub-micrometer thick CZTS thin films prepared from a direct solution approach (via dip-coating) from ethanol based true solutions by intuitively manipulating the starting molar concentration of reagent solutions and the sulfurization ambience. The processing with precursor solution of lower ionic concentration and sulfurization with nominal sulfur amount, although yielded phase-pure films, had several issues including requirement of multiple process steps to yield films of appropriate thickness, and relatively small grain size of the films. This problem was apparently alleviated by increasing the ionic concentration in the precursor solution and the sulfur amount. It is highlighted that with just two dipping cycles of solution with 1M Cu-solution, direct solution coating followed by sulfurization at 575 °C, phase pure kesterite CZTS films of ~850 nm thickness can be obtained. Additionally, in contrast to the reported bilayered structure (i.e., performance limiting small-grained bottom layer and large grained top layer), the resulting films exhibited a conformal microstructure with reasonably large grains. The films showed the bandgap of 1.42 eV and very high photosensitivity upon illumination of white light of intensity of 100 mW/cm^2, typical of an absorber layer to be potentially used in photovoltaic devices.

CHAPTER – 7

EFFECT OF Se ALLOYING IN CZTS THIN FILMS

As discussed in the Introduction (Chapter 1), Se alloying with CZTS (i.e., the formation of $Cu_2(ZnSn)(S_{1-x}Se_x)_4$ or CZTSSe) lowers the V_{oc} deficit (i.e., $E_g/q - V_{oc}$) and helps in obtaining higher efficiency [123] and different Se/(S+Se) ratios exhibit a significant impact on the electronic characteristics of the device such as open circuit voltage (V_{oc}), short circuit current density (J_{sc}) and the power conversion efficiency of CZTSSe based solar cells. This chapter deals with a systematic study of Se inclusion as a consequence of selenization of the already sulfurized films (as discussed in the previous chapter).

The phase pure CZTS films were prepared with the optimized parameters as established in chapter 6, i.e., deposited with two dipping from solution having 1M $CuCl_2$ and sulfurized with 2 g of sulfur. These CZTS films were selenized for different durations and with different Se amount. Table 7.1 list the sample codes and the selenization conditions.

Table 7.1: Sample code and the selenization conditions (selenization temperature was same as sulfurization temperature of 575 °C)

Sample code	Selenization condition
S1	No selenization (0g Se)
S2	2.0 g Se, 60 min
S3	2.0 g Se, 15 min
S4	1.5 g Se, 15 min
S5	1.0 g Se, 15 min
S6	1.5 g Se, 30 min
S7	1.5 g Se, 60 min

Fig. 7.1: Photograph of the film selenized for 60 min with 2 g of Se (sample S2). Note the non-uniform and patchy appearance of the film.

7.1 IMPACT OF Se AMOUNT

When the amount of Se (2g) and selenization duration (60 min) was same as that of optimized sulfurization (i.e., sample S2) the resultant film had a very patchy appearance (Fig. 7.1). This may be due to the initial alloying of Se with CZTS followed by the evaporation of volatile components/loss of adhesion due to prolonged heat treatment. In order to examine the validity of this assumption and to improve the adherence of the film, we decreased the selenization duration to 15 min (sample S3). The adherence of the film to the substrate was indeed improved and a smooth uniform film was obtained. The XRD pattern of the film showed reflections at 26.55, 27.43, 33.38, 45.37, 46.52, 51.08 and 54.01° (Fig. 7.2a). The peaks at 26.55, 33.38 and 51.08° belong to (220), (321) and (531) planes of Cu_4SnS_4 (JCPDS file: 27-196) respectively whereas the peak at 45.37° is attributed to either (512) plane of Cu_4SnS_4 or (220) plane of ZnSe (JCPDS file: 3-65-9602). The peaks at 27.43, 46.52 and 54.01° can be attributed respectively to (112), (220) and (312) planes of CZTSSe. This is inferred from the fact that these peaks are positioned in between the diffraction peaks expected of CZTS (28.54, 47.33 and 56.17°) and CZTSe (27.10, 45.06 and 53.41°) [228,229]. The partial replacement of S by Se atoms in the lattice is expected to result in shifting of Bragg peaks towards lower 2θ values. The presence of the secondary phases, as mentioned above, were also confirmed by the Raman spectroscopy in the form of peaks at 294, 319, 342, 355 and 373 cm^{-1} in the Raman spectrum of the sample belonging to various forms of Cu-Sn-S. [176,179,180]

In an effort to grow phase pure films, we then prepared the films in identical process steps, but with decreased amount of Se placed in the crucible during the selenization treatment. The decreased amount of selenium led to the formation of phase pure CZTSSe films. When the quantity of Se was reduced to 1.5 g and selenized for 15 min (sample S4), peaks at 27.67, 45.63 and 53.96° were observed in the XRD patterns (Fig. 7.2a). These peaks are identified as reflections from to (112), (220) and (312) planes of CZTSSe since these peaks are positioned between those expected for pure sulfide and pure selenide compounds. However, for the films grown by selenization for 15 min with 1 g of Se (sample S5), diffraction peaks at 27.15, 45.19 and 53.42° were observed, which are attributed to (112), (220) and (312) planes of pure selenide CZTSe (JCPDS file: 52-868), respectively. The phase of the films was further confirmed by the Raman spectroscopy. Sample S4 (Fig. 7.2) showed an intense peak at 194 cm^{-1} and a small hump at 175 cm^{-1} which correspond to the kesterite CZTSSe phase, consistent with the previously reported Raman spectral data [230]. On the other hand, Raman spectrum of sample S5 showed an intense peak at 192 cm^{-1} and a small hump at 231 cm^{-1} typical of CZTSe [230].

The FESEM images of surface and cross sectional view of the phase pure samples S4 and S5 are shown in Figs. 7.2 c and d, respectively. Sample S4 is characterized by relatively larger grains with a uniform microstructure with 1.2 μm thickness whereas smaller grains with a porous microstructure are observed in sample S5. In view of the better microstructure and single phase corresponding to CZTSSe (compound containing both S and Se) nature of sample S4 is considered to be more suitable for the photovoltaic application compared to sample S2, S3 and S5. Further studies were carried out for samples selenized with 1.5 g Se.

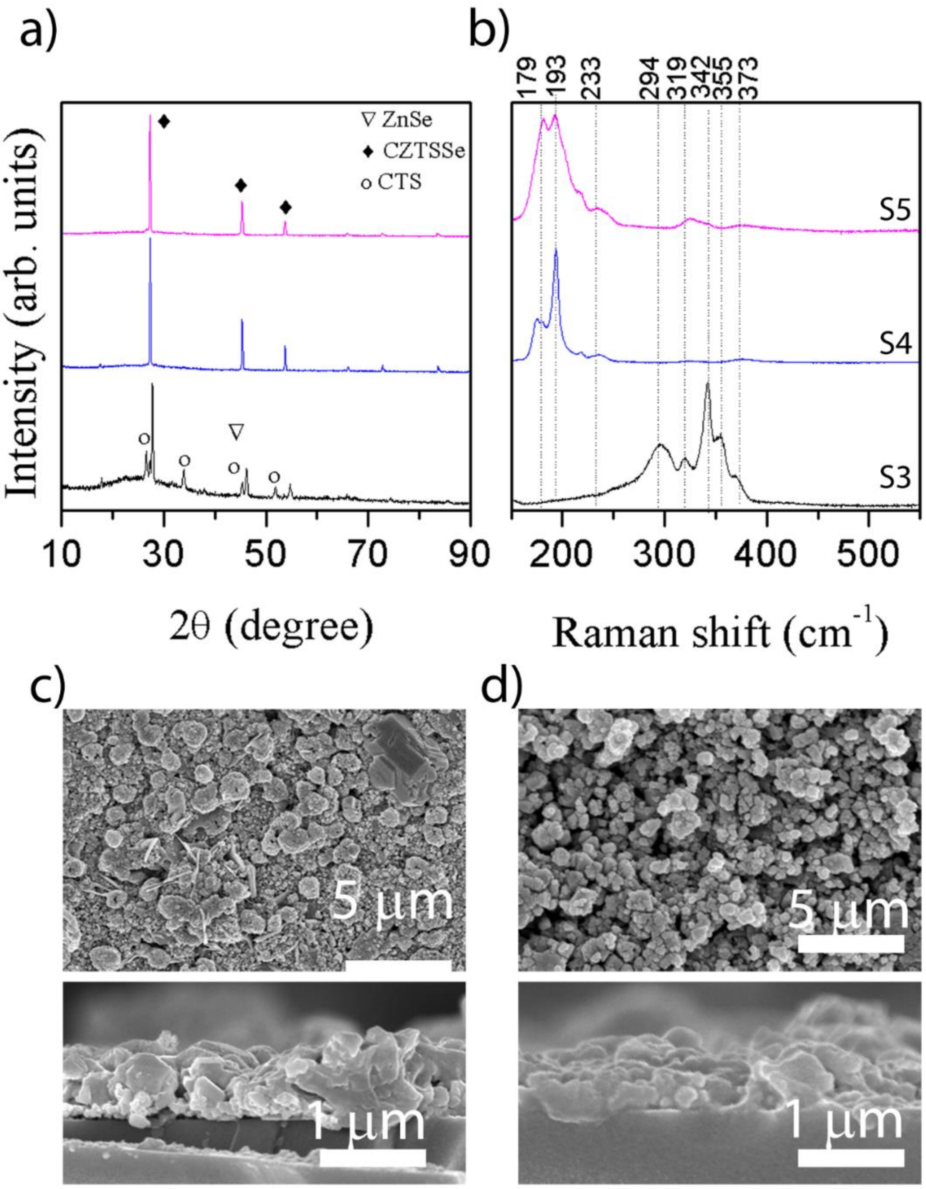

Fig. 7.2: Typical (a) XRD pattern and (b) Raman spectrum of the films selenized with 2.0g (sample S3), 1.5g (sample S4) and 1.0g (sample S5) of Se. Surface and cross-sectional FESEM image of the film selenized with 1.5g (c) and 1.0g (d) of Se. Selenization duration was 15 min for all samples.

7.2 IMPACT OF SELENIZATION DURATION

7.2.1 Evolution of phase and microstructure

In addition to the requirement of single phase nature of the films, the amount of Se incorporated into the CZTS is very important as different Se/(S+Se) ratios exhibit a significant impact on the properties of the films including bandgap, passivation of grain boundaries and trap centers, etc., which direct affect the performance of the devices. As shown in the previous section, selenization of the phase pure CZTS at 575 °C for 15 min with 1.5 g of Se yielded phase pure CZTSSe thin films with a compact microstructure. Results of the EDS measurements showed the Se/(S+Se) ratio for this sample to be about 0.68 (Table 7.2). We have investigated whether the Se/(S+Se) ratio and hence the properties of the films can be manipulated by further optimization through varying the selenization duration. Table 7.2 shows the [Se]/[S + Se] ratio (as determined by EDS) as a function of selenization duration. In fact, significant changes in the ratio with the selenization duration was observed. For example, the ratio continuously decreased from 0.68 for 15 min selenization to 0.28 for 60 min selenization.

Figures 7.3 a and b show the surface and cross sectional view of the films selenized for 30 and 60 min (sample S6 and S7), respectively. Compared to sample S4 (Fig. 7.2c), the films showed decreased thickness and a deteriorated microstructure. The surface FESEM images for the sample selenized for 60 min showed clear degradation of the microstructure characterized by very small crystallite size and a channel like network of voids/pores. This degradation is thought to stem from the annealing for prolonged duration, which might have resulted in the loss of volatile components. In fact as shown below, a clear loss of Se from the films is found from the analysis of the XRD and Raman results.

Figure 7.3c shows the XRD patterns of CZTS films obtained by selenization of the CZTS film for 15 min (sample S4), 30 min (sample S6) and 60 min (sample S7). For easy comparison the figure also contains the XRD pattern for the only sulfurized sample (sample S1). For sample S6, the XRD pattern shows three peaks at 27.92, 46.10 and 54.56°, which can be attributed respectively to (112), (220) and (312) planes of CZTSSe. Interestingly, the peak positions are shifted to higher 2θ values compared to the 15 min-selenized sample (sample S4). On further increasing the selenization time to 60 min (sample S7), there was marginal right shift of the peaks (observed at 27.97, 46.15 and 54.61°). The right shift of the Bragg reflection peak positions may be due to the loss of Se from the thin films, which is also supported by the EDS as explained earlier. It also suggests that although single phase CZTSSe ($Cu_2ZnSn(S_{1-x}Se_x)_4$) films are formed, there is a compositional variation (i.e., value of x) and that selenization beyond 15 min resulted in significant loss of Se as manifested from the decreased value of Se/(S+Se) ratio. This compositional variation is also reflected from the corresponding Raman spectra (Fig. 7.3d). For example, compared to the Raman spectrum for the 15 min-selenized sample (sample S4), sample S6 (selenized for 30 min) showed evolution of a peak at about 263 cm^{-1}. On the other hand, selenization for 60 min (sample S7) resulted in complete disappearance of the peaks at 175 and 193 cm^{-1} and occurrence of only two peaks at 263 and 362 cm^{-1} corresponding to the CZTSSe phase.

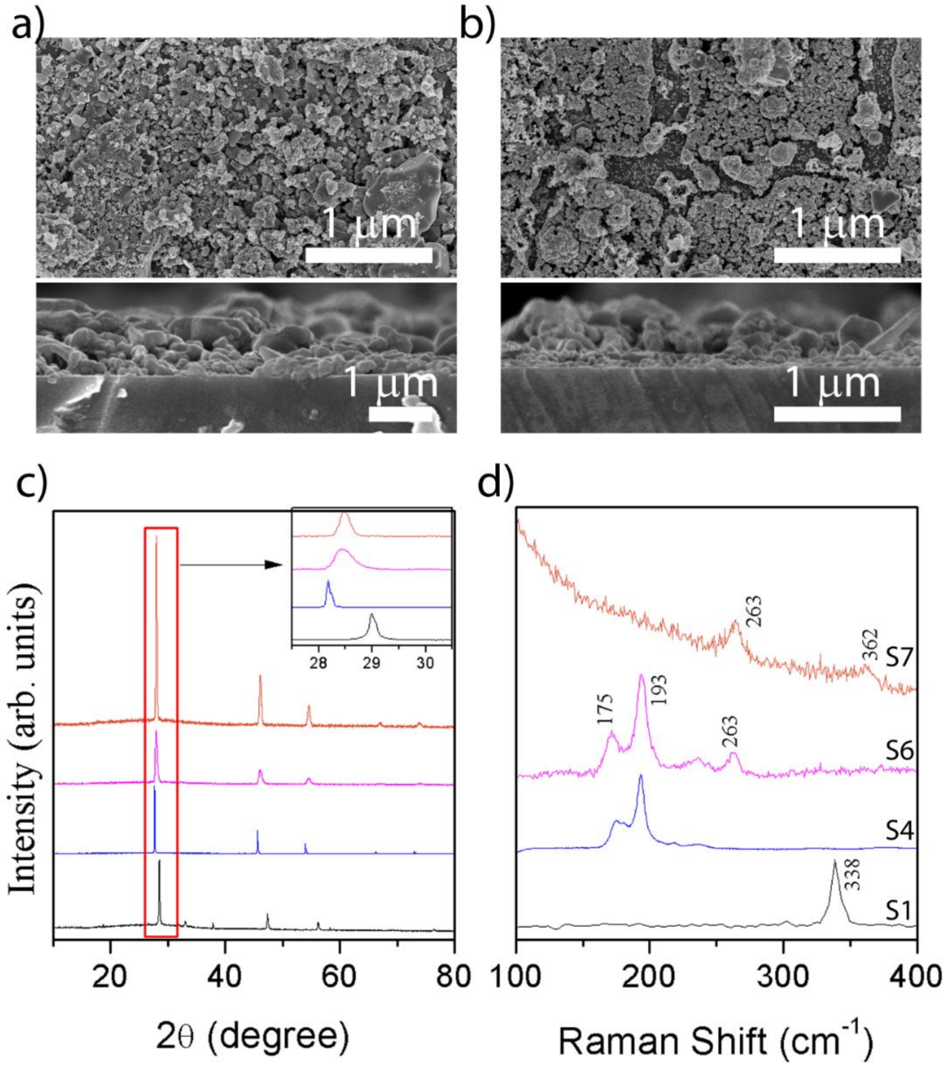

Fig. 7.3: Surface and cross-sectional FESEM image of the film selenized for (a) 30 min (Sample S6) and (b) 60 min (Sample S7). The corresponding (c) XRD patterns and (d) Raman spectra of the samples. Inset to (c) shows the zoomed up region nearer to the (112) peak in the XRD pattern.

7.2.2 Optical and electrical properties

We then evaluated various properties such as optical bandgap, electrical resistivity, carrier concentration and photo-responsive properties of the single phase CZTSSe samples (selenized with 1.5 g Se at 575 °C for 0, 15, 30 and 60 min). Figure 7.4a shows the typical UV-visible-NIR reflectance (R) and transmittance (T) curves of the films. The optical absorption coefficient α estimated using the formula $\alpha = (1/d) \ln [(1-R)^2/T]$ for the film of thickness d, was the order of 10^5 cm^{-1}. Such a high of absorption coefficient is highly favorable for efficient photon absorption and generation of electron-hole pairs [186]. The optical bandgap of the films was determined from the Tauc plots of $(\alpha h\nu)^2$ vs photon energy hν, as shown in Fig. 7.4b. It was observed that the bandgap values were evaluated to be 1.42, 1.06, 1.25 and 1.41 eV for samples selenized for S1, S4, S6 and S7 respectively. The observed value of the bandgap of the films is consistent with the expected values based on the Se/(S+Se) ratio and is similar to the values reported by several earlier researchers [22,80,187]. The results of the Hall measurement revealed the p-type conductivity of the above samples. The carrier concentration, resistivity and Hall mobility of the films are tabulated in Table 7.2. The obtained values are similar to the ones reported in literature and supported the above reported data [97,188,189]

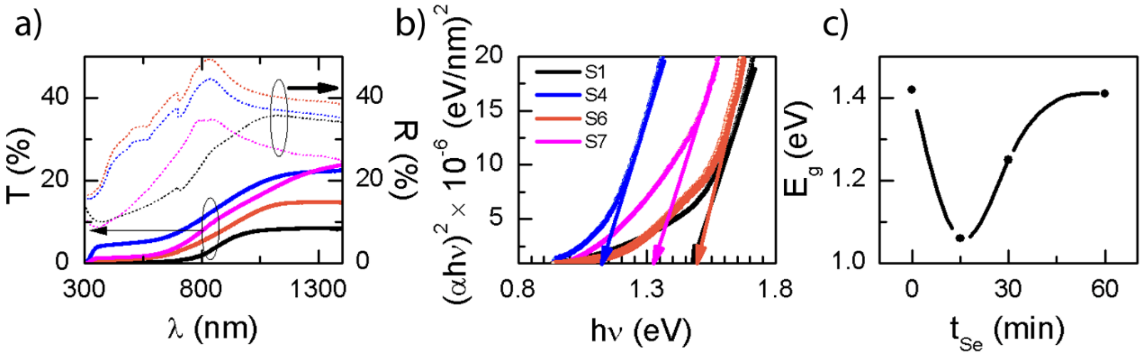

Fig. 7.4: (a) Typical reflectance and transmittance curves (b) Tauc plot of $(\alpha h\nu)^2$ vs hν and (c) plot of variation in bandgap of the films selenized with 1.5 gm Se at 575 °C for different durations.

Figure 7.4c shows the variation in bandgap of the films with respect to the selenization time. The bandgap value of 1.4 eV at 0 min selenization time (no selenization, only sulfurization) is attributed to the CZTS phase. The formation of the CZTS phase has been confirmed by the XRD and Raman measurements. With the increase in the selenization time, the bandgap first decreased and then increased. This is attributed to the varying Se/(S+Se) ratio in the films. For small duration of selenization (15 min), alloying is believed to have taken place, as indicated by a Se/(S+Se) = 0.68. For increase in selenization duration, the Se amount in the films decreased (Table 7.2) and correspondingly the bandgap has increased. The observed values are similar to the ones reported in literature [22,80,187].

Table 7.2 Various properties of the samples selenized with 1.5 gm Se at 575 °C for different durations.

	0 min (Sample S1)	15 min (Sample S4)	30 min (Sample S6)	60 min (Sample S7)
Se/S+Se	0	0.68	0.52	0.28
R_h (cm^3/C)	0.59	14.97	11.08	8.51
ρ (Ω-cm)	0.43	13.68	10.23	7.71
n (cm^{-3})	10.47×10^{18}	4.17×10^{17}	5.63×10^{17}	7.35×10^{17}
μ ($cm^2V^{-1}s^{-1}$)	1.41	1.09	1.09	1.11
E_g (eV)	1.42	1.06	1.25	1.41

The analysis of the results of the XRD, Raman, FESEM, EDS and Hall measurements revealed that the selenization at 575 °C for 15 min with 1.5 gm of Se resulted in single phase CZTSSe thin films with Se/S+Se ratio of 0.68 and bandgap of 1.06 eV. Additionally, these films having a thickness of 1.2 μm exhibited a very compact and large-grained microstructure. Thus, in the given experimental setting, this presents a case of optimized condition for the formation of CZTSSe films for photovoltaic application. Further confirmation of the phase and chemical environment of the elements was carried out by the XPS measurements. The typical high resolution core level spectra acquired in the Cu 2p, Zn 2p, Sn 3d, S 2p and Se 3d regions CZTSSe sample S4 was presented in Fig. 7.5. The presence of similar peaks for Cu, Zn, Sn and S as in sample S1 depicts that Cu, Zn, Sn and S are in +1, +2, +4 and -2 oxidation states which is a prerequisite for the formation of CZTSSe phase. The Se 3d spectrum has a broad peak at a binding energy range of 53 – 54eV. Deconvolution of this broad peak gives two different peaks at 53 and 54.1 eV which is in accordance with the previous reports [231].

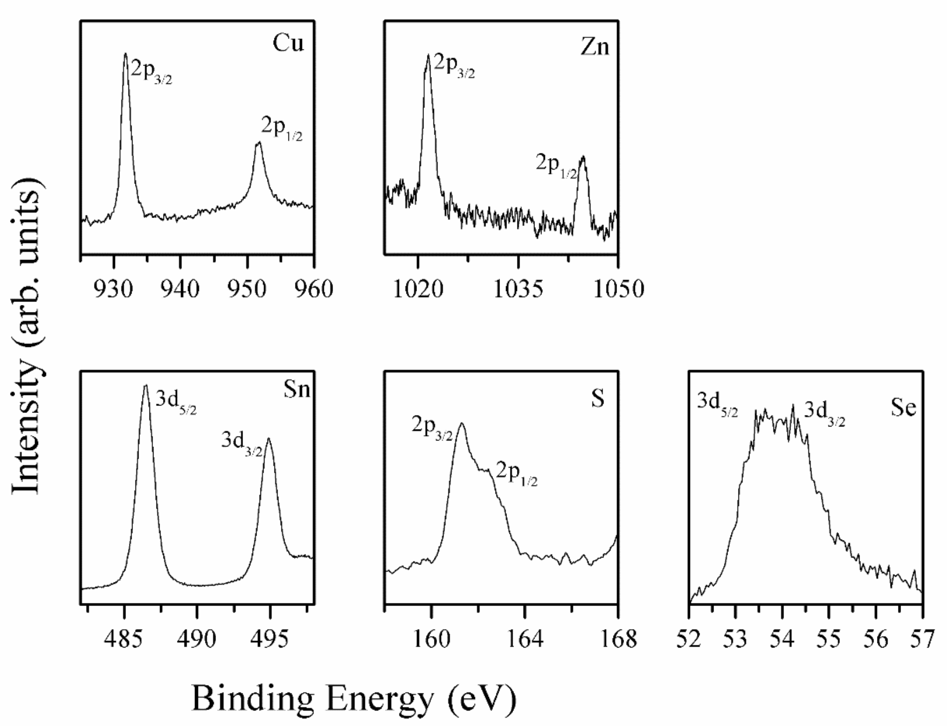

Fig. 7.5: Typical core level spectra for Cu 2p, Zn 2p, Sn 3d, S 2p and Se 3d of the CZTSSe film selenized with 1.5 g of Se for 15 min.

7.3 FABRICATION OF DEVICE

7.3.1 Cell structure

Thin film solar cells work on the principle of p-n heterojunction formed by placing two electronically dissimilar semiconductor materials together. A typical CZTS thin film based device consist of layers of different materials in thin film form as shown in Fig. 7.6.

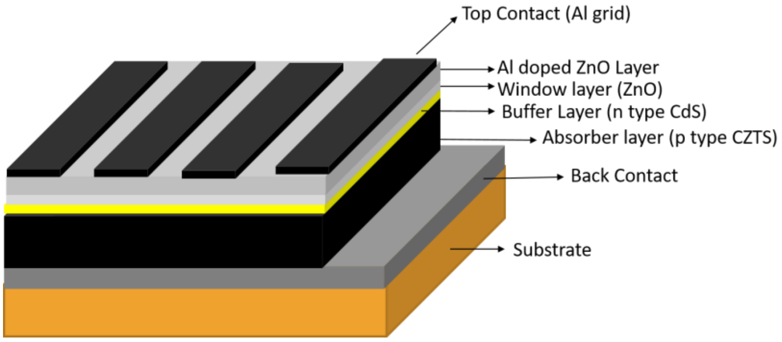

Fig. 7.6: Schematic diagram of the CZTSe based thin film solar cell.

In a typical structure (glass/Mo/CZTS/CdS/i:ZnO/ZnO:Al/Al), optimized Mo films in the form of bilayers are used as bottom electrode. The details of the growth of the layers is given in Section 2.3, Chapter 2. The absorber layer (i.e., the optimized CZTS layer) was grown as detailed in the previous section. The n-type layer in the form of a 50 nm thick CdS layer was grown by CBD method (as discussed in Chapter 3). The i-ZnO (~100 nm) and ZnO:Al (~500 nm) layers were grown by RF magnetron sputtering from compound targets (Section 2.4, Chapter 2). The top contact was given as Al grids, prepared by thermal evaporation through a shadow mask. Area of the solar cell was defined by physically scribing and was kept about 0.25 cm^2. Figure 7.7a shows the photograph of devices while Fig. 7.7b shows the cross-sectional FESEM images of various layers of a typical cell. The cross sectional micrograph of the CZTS film substantiates the nearly uniform well-adhered film. The interfacial MoS_2 layer between CZTS and Mo spontaneously developed during the deposition of the CZTS layer and its sulfurization at elevated temperatures [113,232]. The presence of MoS_2 layer offers additional benefits for the strong adherence of the CZTS absorber layer over the Mo coated substrates [113,232].

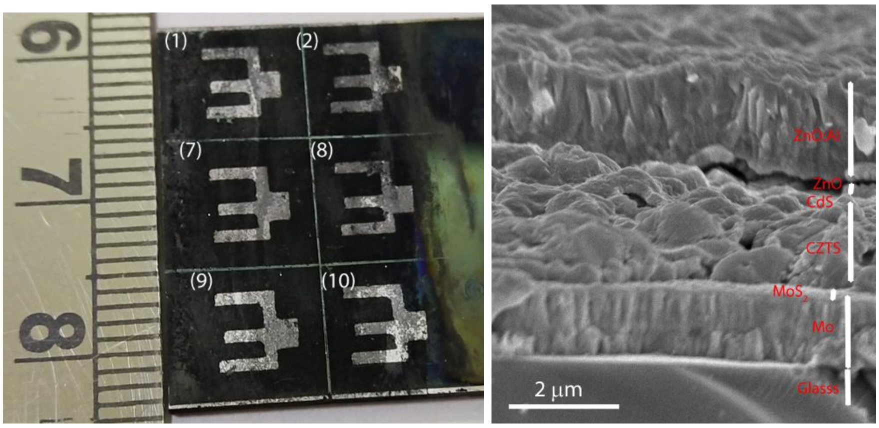

Fig. 7.7: (a) photograph of the device prepared and (b) Representative cross-section FE-SEM micrographs showing different layers of a completed CZTSSe solar cell

7.3.2 Device performance

The current density–voltage (J–V) curves of the resultant cells under 1000 W/cm^2 illumination are shown in Fig 7.8. All devices showed clear signatures of photovoltaic effect. From the J-V curves, the performance metrics such as open circuit voltage V_{oc}, short circuit current density J_{sc}, fill factor FF and conversion efficiency η, were estimated and are presented in Table 7.3.

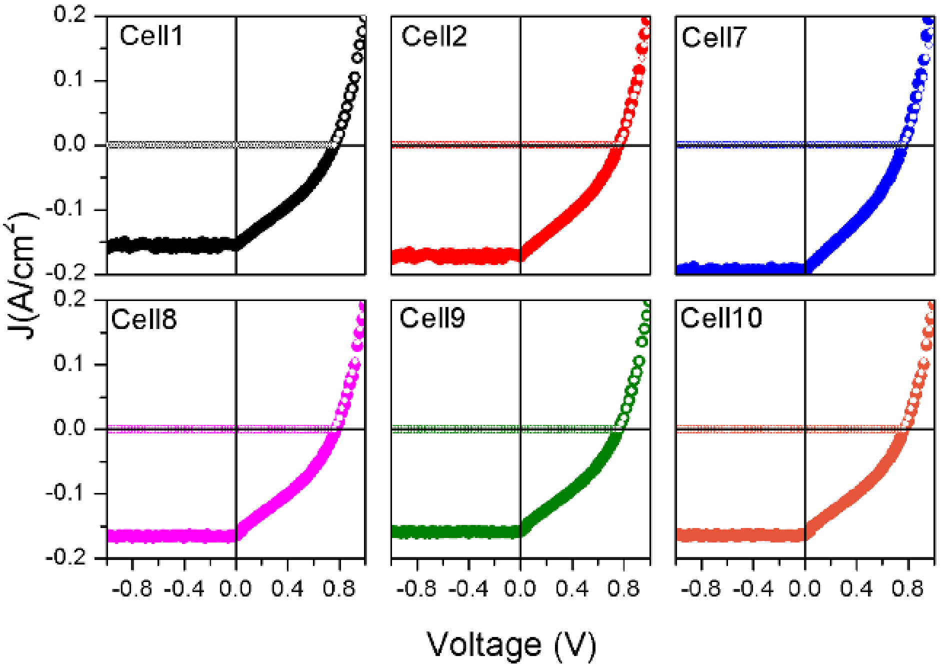

Figure 7.8: Current density versus voltage (J-V) characteristics under dark and illumination conditions for Al:ZnO/ZnO/CdS/CZTS/Mo/SLG solar cells.

Table 7.3: Performance metrics of the prepared photovoltaic cells

	Cell 1	Cell 2	Cell 7	Cell 8	Cell 9	Cell 10
V_{oc}(V)	0.76	0.76	0.76	0.77	0.76	0.78
I_{sc} (A)	0.039	0.043	0.049	0.041	0.039	0.041
P_{max} (W)	0.00097	0.01073	0.01220	0.01048	0.00973	0.01033
FF (%)	32.88	32.89	32.89	32.57	32.88	32.18
η (%)	0.39 ± 0.10	0.43 ± 0.17	0.49 ± 0.15	0.42 ± 0.05	0.39 ± 0.12	0.41 ± 0.19

Among all devices studied, a maximum efficiency of 0.49 % has been obtained. The main reason of the poor performance of the devices may be the low J_{SC} and the very low fill-factor (FF), as noted from the table. Very often, the low FF has been attributed to the high series resistance and low shunt resistance of the device, which originate from the poor microstructure, reactions at interfaces, inappropriate electrical properties of the window layers, etc.[233]. Furthermore, a high carrier concentration and low resistivity of the CZTS films as obtained in this work also contribute to enhanced recombination [232,233]. Thus further examination of the devices to improve the performance is warranted and may form the future scope of this work. Nevertheless, this preliminary result indicates that proposed approach of film growth from non-toxic ethanol based solutions via dip-coating followed by a high temperature annealing is potentially viable. Further optimization of other layers is of significant interest to improve the device performance.

CHAPTER – 8

SUMMARY AND FUTURE SCOPE

In this chapter, the major conclusions of work are highlighted. The scope for further investigations has also been suggested.

CdS thin films, which has been established as the most popular choice for n-type layer in CZTS based solar cells, were grown by the CBD process using ammonia-free solutions in a single dip at various bath temperatures ranging from 40 - 80 °C. The bandgap of the films was in the range of 2.3 - 2.6 eV, suggesting their suitability for application CZTS based solar cells. While a higher bath temperature showed fast increase in the thickness, there was structural degradation for thicker films as evidenced from the analysis of the XRD patterns. In view of the slow deposition rate and hence better control, deposition at 40 °C is believed to be suitable for solar cell applications. In order to study the roughening of the films deposited at 40 °C, dynamic scaling theory was employed. The analyses revealed anomalous scaling of roughness with rapid roughening of the surfaces as a consequence of bulk diffusion instability. The characteristic exponents $\alpha_{loc} = 0.78 \pm 0.07$, $\alpha = 2.20 \pm 0.08$, $\alpha_s = 1.49 \pm 0.22$, $1/z = 0.46 \pm 0.06$, $\beta = 0.86 \pm 0.05$ and $\beta_{loc} = 0.43 \pm 0.10$ were determined using the real and Fourier space correlation functions. The values of the exponents suggests that nonlocal effect plays an important role in the evolution of growth front of the CBD thin films. In the light of previous studies on electroless and electrodeposited films, the results indicate that nonlocal effects in the form of diffusional instability should be incorporated in the models to further our understanding of growth mechanism of these films.

In view of the potential of non-toxic solution processing of Cu_2ZnSnS_4 (CZTS) thin films for development of low cost solar cells, in this work, the CZTS thin films were grown by a direct solution approach (via dip-coating) from ethanol based true solutions of common salts of $CuCl_2$, $SnCl_2$, $ZnCl_2$ and thioacetamide (TAA). We have elucidated the role of complexing agent in the reaction mechanisms in transformation from precursor solution to CZTS phase via intermediate solid state binary and ternary compounds during deposition and the subsequent sulfurization treatment in the ethanol based solution process. In the initial stage of solution mixing, the presence of the complexing agent MEA inhibited the complete reduction of Cu^{2+} to Cu^{+} and oxidation of Sn^{2+} to Sn^{4+}, which subsequently affected the reaction pathway resulting in undesirable secondary phases. Contrastingly, the absence MEA facilitated early formation of the CZTS phase revealing a smaller activation energy for the decomposition of the precursor complex. The reaction pathway is demonstrated to be different to the other liquid based methods that requires dispersing agents to suspend nano- or micro-scale particles at elevated temperature.

Considering that post-deposition high temperature annealing (HTA) in a chalcogen environment is critical to the grain growth and phase evolution in the CZTS based thin films, we have demonstrated a geometry controlled heat treatment strategy using elemental sulfur flakes to prepare phase pure CZTS thin films from the ethanol based solutions via dip coating. From the comparative investigation of the HTA settings including systematic variations in the ramp rate, sulfur source temperature and the reaction temperature, the influencing mechanisms of phase evolution are explained. The results elucidate the critical dependence of the HTA setting, in particular of the sulfur vapor flux constrained by the geometry of the placement of sulfur flakes, on the phase evolution of the films and highlight the promise of the approach including the proposed HTA strategy for reproducible growth of phase pure kesterite CZTS films.

In addition, we have shown how by intuitively manipulating the starting molar concentration of reagent solutions and the sulfurization ambience uniform large grained submicrometer thick CZTS layers, as required for solar cell application, can be prepared. The processing with precursor solution of lower ionic concentration and sulfurization with nominal sulfur amount, although yielded phase-pure films, had several issues including requirement of multiple process steps to yield films of appropriate thickness. This problem was apparently alleviated by increasing the ionic concentration in the precursor solution and the sulfur amount. It is highlighted that with just two dipping cycles of solution with 1M Cu-solution, direct solution coating followed by sulfurization at 500 °C, phase pure kesterite CZTS films of ~850 nm thickness can be obtained. Additionally, in contrast to the reported bilayered structure (i.e., performance limiting small-grained bottom layer and large grained top layer), the resulting films exhibited a conformal microstructure with reasonably large grains. The films showed the bandgap of 1.42 eV and very high photosensitivity upon illumination of white light of intensity of 100 mW/cm^2, typical of an absorber layer to be potentially used in photovoltaic devices.

It was found that the post-deposition heat treatment ambience, especially the selenization critically influenced the grain structure and properties of the eventual films. Based on the results of experiments with variation in amount of Se flakes and selenization duration, a detailed discussion on the influencing mechanism of the selenization processes has been presented. It was revealed that the selenization at 575 °C for 15 min with 1.5 gm of Se resulted in single phase CZTSSe thin films with Se/S+Se ratio of 0.68 and bandgap of 1.06 eV. These films having a thickness of 1.2 μm exhibited a very compact and large-grained microstructure. Thus, in the given experimental setting, this presents a case of optimized condition for the formation of CZTS films for photovoltaic application. Solar cells in a typical structure of glass/Mo/CZTS/CdS/i:ZnO/ ZnO:Al/Al were fabricated. A maximum efficiency of 0.49 % has been obtained. The main reason of the poor performance of the devices may be the low J_{SC} and the very low fill-factor (FF). The low FF has been attributed to the high series resistance and low shunt resistance of the device, which originate from the poor microstructure, reactions at interfaces, and inappropriate electrical properties of the window layers.

Although the understanding of reaction mechanism leading to the growth of single phase CZTSSe thin films has been the motivation of this work, we believe further research is warranted to realize high efficiency devices based on the obtained films. In the following, we suggest further experiments which can be helpful in this regard.

- In view of the obtained poor short-circuit current density and the low fill-factor, the current collection mechanism should be investigated. For a study of surface potential at grain boundaries can provide information about the nanoscale carrier transport in the films.
- Admittance spectroscopy can provide information about crucial factors of the heterojunction such as the acceptor concentration, depletion width, etc. which can be useful for further optimization.
- Reactions at the interfaces have been fund to be critical for efficient charge collection. Thus Mo/CZTSSe and CZTSSe/CdS interfaces should be probed further.
- Trap states and the role of defects should be investigated to further the understanding of the CZTSSe thin films.

REFERENCES

1. http://www.un.org/climatechange/mitigation/reducing-emissions/.
2. https://www.iea.org/geco/data/.
3. J. N. Mayer, S. Philipps, N. S. Hussein, T. Schlegl and C. Senkpiel. “Current and future cost of photovoltaics: Long-term scenarios for market development, system prices and LCOE of utility-scale PV systems.”
4. W. Shockley and H. J. Queisser. “Detailed balance limit of efficiency of p-n junction solar cells.” *Journal of applied physics* **32** (1961) 510-519.
5. R. Kamada, T. Yagioka, S. Adachi, A. Handa, K. F. Tai, T. Kato and H. Sugimoto. “New world record Cu(In,Ga)(Se,S)$_2$ thin film solar cell efficiency beyond 22%.” In *2016 IEEE 43rd Photovoltaic Specialists Conference (PVSC)*, 1287-1291. IEEE, 2016.
6. P. Y. Chen, J. Qi, M. T. Klug, X. Dang, P. T. Hammond and A. M. Belcher. "Environmentally responsible fabrication of efficient perovskite solar cells from recycled car batteries" *Energy & Environmental Science* **7** (2014) 3659–3665.
7. J. S. Manser, J. A. Christians and P. V. Kamat. "Intriguing Optoelectronic Properties of Metal Halide Perovskites" *Chemical Reviews* **116** (2016) 12956–13008.
8. National Renewable Energy Lab (NREL), Best Research-Cell Efficiencies, NREL, Golden, CO (2018).
9. I. C. Smith, E. T. Hoke, D. Solis-Ibarra, M. D. McGehee and H. I. Karunadasa. “A Layered Hybrid Perovskite Solar-Cell Absorber with Enhanced Moisture Stability” *Angewandte Chemie* **126** (2014) 1 – 5.
10. http://investor.firstsolar.com/releasedetail.cfm?ReleaseID=828273/.
11. http://www.solar-frontier.com/eng/news/2017/0227_press.html/.
12. S. Bag, O. Gunawan, T. Gokmen, Y. Zhu, T. K. Todorov and D. B. Mitzi. “Low bandgap liquid-processed CZTSe solar cell with 10.1% efficiency.” *Energy & Environmental Science* **5** (2012) 7060-7065.
13. http://investor.firstsolar.com/releasedetail.cfm?ReleaseID=833971/.
14. H. Katagiri, K. Jimbo, W. S. Maw, K. Oishi, M. Yamazaki, H. Araki and A. Takeuchi. “Development of CZTS-based thin film solar cells.” *Thin Solid Films* **517** (2009) 2455-2460.
15. W. Wang, M. T. Winkler, O. Gunawan, T. Gokmen, T. K. Todorov, Y. Zhu and D. B. Mitzi. “Device characteristics of CZTSSe thin-film solar cells with 12.6% efficiency.” *Advanced Energy Materials* **4** (2014) 1301465.
16. B. Pejjai, V. R. M. Reddy, S. Gedi and C. Park. “Status review on earth-abundant and environmentally green Sn-X (X = Se, S) nanoparticle synthesis by solution methods for photovoltaic applications.” *International Journal of Hydrogen Energy* **42** (2017) 2790-2831.

17. H. Katagiri, N. Sasaguchi, S. Hando, S. Hoshino, J. Ohashi and T. Yokota. "Preparation and evaluation of Cu_2ZnSnS_4 thin films by sulfurization of E- B evaporated precursors." *Solar Energy Materials and Solar Cells* **49** (1997) 407-414.

18. T. M. Friedlmeier, et al., Proc. 14thEurop. Photovolt. Solar Energy Conf., Bedford, 1242 (1997).

19. H. Katagiri, et al., Tech. Dig. Photovoltaic Science and Engineering Conf.-11, Sapporo, 647 (1999).

20. H. Katagiri, et al., Proc. World Conf. on Photovoltaic Energy Conversion-3, Osaka, 2874 (2003).

21. H. Katagiri, K. Jimbo, S. Yamada, T. Kamimura, W. S. Maw, T. Fukano, T. Ito and T. Motohiro. "Enhanced conversion efficiencies of Cu_2ZnSnS_4-based thin film solar cells by using preferential etching technique." *Applied physics express* 1 (2008) 041201.

22. T. K. Todorov, K. B. Reuter and D. B. Mitzi. "High-Efficiency Solar Cell with Earth-Abundant Liquid-Processed Absorber." *Advanced Energy Materials* **22** (2010) E156-E159.

23. D. Aaron, R. Barkhouse, O. Gunawan, T. Gokmen, T. K. Todorov and D. B. Mitzi. "Device characteristics of a 10.1% hydrazine-processed $Cu_2ZnSn(Se,S)_4$ solar cell." *Progress in Photovoltaics: Research and Applications* **20** (2012) 6-11.

24. T. K. Todorov, J. Tang, S. Bag, O. Gunawan, T. Gokmen, Y. Zhu and D. B. Mitzi. "Beyond 11% efficiency: characteristics of state-of-the-art $Cu_2ZnSn(S, Se)_4$ solar cells." *Advanced Energy Materials* **3** (2013) 34-38.

25. J. Paier, R. Asahi, A. Nagoya and G. Kresse. "Cu_2ZnSnS_4 as a potential photovoltaic material: a hybrid Hartree-Fock density functional theory study." *Physical Review B* **79** (2009) 115126.

26. T. Maeda, S. Nakamura, and T. Wada, Jpn. J. Appl. Phys., Part I 50, 4 (2011).

27. S. Chen, J.-H. Yang, X.-G. Gong, A. Walsh and S.-H. Wei. "Intrinsic point defects and complexes in the quaternary kesterite semiconductor Cu_2ZnSnS_4." *Physical Review B* **81** (2010) 245204.

28. J. J. Scragg. *Studies of Cu_2ZnSnS_4 films prepared by sulfurization of electrodeposited precursors*. (PhD thesis, University of Bath, 2010).

29. I. D. Olekseyuk, I. V. Dudchak and L. V. Piskach. "Phase equilibria in the Cu_2S–ZnS–SnS_2 system." *Journal of alloys and compounds* **368** (2004) 135-143.

30. H. Flammersberger. *Experimental study of Cu_2ZnSnS_4 thin films for solar cells*. (PhD. Thesis, Uppasala University, 2010).

31. R. Scheer and H.-W. Schock. *Chalcogenide photovoltaics: physics, technologies, and thin film devices*. (John Wiley & Sons, Germany, 2011).

32. S. Adachi. *Earth-abundant materials for solar cells: Cu_2-II-IV-VI_4 semiconductors*. (John Wiley & Sons, United Kingdom, 2015).

33. S. R. Kodigala. *Thin film solar cells from earth abundant materials: growth and characterization of $Cu_2(ZnSn)(SSe)_4$ thin films and their solar cells*. (Elsevier, Newnes, 2013).

34. S. Chen, X. G. Gong, A. Walsh and S. H. Wei. "Electronic structure and stability of quaternary chalcogenide semiconductors derived from cation cross-substitution of II-VI and I-III-VI_2 compounds." *Physical Review B* **79** (2009) 165211.

35. A. Redinger, D. M. Berg, P. J. Dale and S. Siebentritt. "The consequences of kesterite equilibria for efficient solar cells." *Journal of the American Chemical Society* **133** (2011) 3320-3323.

36. L. Choubrac, A. Lafond, C. G. Deudon, Y. Moëlo and S. Jobic. "Structure flexibility of the Cu_2ZnSnS_4 absorber in low-cost photovoltaic cells: from the stoichiometric to the copper-poor compounds." *Inorganic chemistry* **51** (2012) 3346-3348.

37. J. J. Scragg, T. Ericson, T. Kubart, M. Edoff and C. P. Björkman. "Chemical insights into the instability of Cu_2ZnSnS_4 films during annealing." *Chemistry of Materials* **23** (2011) 4625-4633.

38. C. M. Sutter-Fella, A. R. Uhl, Y. E. Romanyuk and A. N. Tiwari. "Large-grained Cu_2ZnSnS_4 layers sintered from Sn-rich solution-deposited precursors." *Physica Status Solidi (a)* **212** (2015) 121-125.

39. S. Siebentritt. "Why are kesterite solar cells not 20% efficient?" *Thin solid films* **535** (2013) 1-4.

40. R. Touati, M. B. Rabeh and M. Kanzari. "Structural and optical properties of the new absorber Cu_2ZnSnS_4 thin films grown by vacuum evaporation method." *Energy Procedia* **44** (2014) 44-51.

41. J. J. Scragg, T. Ericson, X. Fontané, V. Izquierdo-Roca, A. Pérez-Rodríguez, T. Kubart, M. Edoff and C. Platzer-Björkman. "Rapid annealing of reactively sputtered precursors for Cu_2ZnSnS_4 solar cells." *Progress in photovoltaics: Research and Applications* **22** (2014) 10-17.

42. H. Yoo and J. Kim. "Growth of Cu_2ZnSnS_4 thin films using sulfurization of stacked metallic films." *Thin Solid Films* **518** (2010) 6567-6572.

43. T. Todorov and D. B. Mitzi. "Direct liquid coating of chalcopyrite light-absorbing layers for photovoltaic devices." *European Journal of Inorganic Chemistry* **2010** (2010) 17-28.

44. J. J. Scragg, P. J. Dale and L. M. Peter. "Towards sustainable materials for solar energy conversion: Preparation and photo-electrochemical characterization of Cu_2ZnSnS_4." *Electrochemistry Communications* **10** (2008) 639-642.

45. B. Ananthoju, F. J. Sonia, A. Kushwaha D. Bahadur, N. V. Medhekar, M. Aslam. "Improved structural and optical properties of Cu_2ZnSnS_4 thin films via optimized potential in single bath electrodeposition." *Electrochimica Acta* **137** (2014) 154-163.

46. Q. Guo, H. W. Hillhouse and R. Agrawal. "Synthesis of Cu_2ZnSnS_4 nanocrystal ink and its use for solar cells." *Journal of the American Chemical Society* **131** (2009) 11672-11673.

47. Q. Guo, G. M. Ford, W.-C. Yang, B. C. Walker, E. A. Stach, H. W. Hillhouse and R. Agrawal. "Fabrication of 7.2% efficient CZTSSe solar cells using CZTS nanocrystals." *Journal of the American Chemical Society* **132** (2010) 17384-17386.

48. M. G. Panthani, V. Akhavan, B. Goodfellow, J. P. Schmidtke, L. Dunn, A. Dodabalapur, P. F. Barbara and B. A. Korgel. "Synthesis of $CuInS_2$, $CuInSe_2$, and $Cu(In_xGa_{1-x})Se_2$

(CIGS) nanocrystal "inks" for printable photovoltaics." *Journal of the American Chemical Society* **130** (2008) 16770-16777.

49. W. Ki, and H. W. Hillhouse. "Earth-abundant element photovoltaics directly from soluble precursors with high yield using a non-toxic solvent." *Advanced Energy Materials* **1** (2011) 732-735.

50. T. K. Chaudhuri and D. Tiwari. "Earth-abundant non-toxic Cu_2ZnSnS_4 thin films by direct liquid coating from metal–thiourea precursor solution." *Solar Energy Materials and Solar Cells* **101** (2012) 46-50.

51. M. Krunks, V. Mikli, O. Bijakina, H. Rebane, A. Mere, T. Varema and E. Mellikov. "Composition and structure of $CuInS_2$ films prepared by spray pyrolysis." *Thin Solid Films* **361** (2000) 61-64.

52. Y. Sun, Y. Zhang, H. Wang, M. Xie, K. Zong, H. Zheng, Y. Shu et al. "Novel non-hydrazine solution processing of earth-abundant $Cu_2ZnSn(S,Se)_4$ absorbers for thin-film solar cells." *Journal of Materials Chemistry A* **1** (2013) 6880-6887.

53. W. Yang, H-S. Duan, B. Bob, H. Zhou, B. Lei, C-H. Chung, S-H. Li, W. W. Hou and Y. Yang. "Novel solution processing of high-efficiency earth-abundant $Cu_2ZnSn(S,Se)_4$ solar cells." *Advanced Materials* **24** (2012) 6323-6329.

54. N. Moritake, Y. Fukui, M. Oonuki, K. Tanaka and H. Uchiki. "Preparation of Cu_2ZnSnS_4 thin film solar cells under non-vacuum condition." *Physica Status Solidi c* **6** (2009) 1233-1236.

55. G. M.vIlari, C. M. Fella, C. Ziegler, A. R. Uhl, Y. E. Romanyuk and A. N. Tiwari. "$Cu_2ZnSnSe_4$ solar cell absorbers spin-coated from amine-containing ether solutions." *Solar Energy Materials and Solar Cells* **104** (2012) 125-130.

56. K. Woo, Y. Kim and J. Moon. "A non-toxic, solution-processed, earth abundant absorbing layer for thin-film solar cells." *Energy & Environmental Science* **5** (2012) 5340-5345.

57. Q. Guo, G. M. Ford, H. W. Hillhouse and R. Agrawall, presented at the 37th IEEE Photovoltaics Specialists Conference (PVSC37), Seattle, WA, June 19-24, (2011**)** .

58. Q. Guo et. al., presented at the 38th IEEE Photovoltaics Specialists Conference (PVSC38), Austin, Texas, June 3-8, (2012).

59. G. Wang, W. Zhao, Y. Cui, Q. Tian, S. Gao, L. Huang and D. Pan. "Fabrication of a $Cu_2ZnSn(S,Se)_4$ photovoltaic device by a low-toxicity ethanol solution process." *ACS Applied Materials & Interfaces* **5** (2013) 10042-10047.

60. M. Jiang, J. Wu, G. Di and G. Li, "Nanostructured solar cell based on solution processed Cu_2ZnSnS_4 nanoparticles and vertically aligned ZnO nanorod array." *Physica Status Solidi: RRL- Rapid Research Letters* **8** (2014) 1-5.

61. M. B. Ortuno-Lopez, J. J. Valenzuela-Jauregui, R. Ramırez-Bon, E. Prokhorov and J. González-Hernández. "Impedance spectroscopy studies on chemically deposited CdS and PbS polycrystalline films." *Journal of Physics and Chemistry of Solids* **63** (2002) 665-668.

62. H. Xin, J. K. Katahara, I. L. Braly and H. W. Hillhouse. "8% Efficient $Cu_2ZnSn(S,Se)_4$ solar cells from redox equilibrated simple precursors in DMSO." *Advanced Energy Materials* **4** (2014) 1301823.

63. Z. Su, K. Sun, Z. Han, H. Cui, F. Liu, Y. Lai, J. Li, X. Hao, Y. Liu and M. A. Green. “Fabrication of Cu_2ZnSnS_4 solar cells with 5.1% efficiency via thermal decomposition and reaction using a non-toxic sol–gel route.” *Journal of Materials Chemistry A* **2** (2014) 500-509.

64. T. Schnabel, M. Löw and E. Ahlswede. “Vacuum-free preparation of 7.5% efficient $Cu_2ZnSn(S,Se)_4$ solar cells based on metal salt precursors.” *Solar Energy Materials and Solar Cells* **117** (2013) 324-328.

65. M. Jiang, F. Lan, X. Yan and G. Li. "$Cu_2ZnS(S_{1-x}Se_x)_4$ thin film solar cells prepared by water-based solution process." *Physica Status Solidi (RRL)–Rapid Research Letters* **8** (2014) 223-227.

66. H. Zhou, H-S. Duan, W. Yang, Q. Chen, C-J. Hsu, W-C. Hsu, C-C. Chen and Y. Yang. "Facile single-component precursor for Cu_2ZnSnS_4 with enhanced phase and composition controllability." *Energy & Environmental Science* **7** (2014) 998-1005.

67. S-N. Park, S-J. Sung, D-H. Son, D-H. Kim, M. Gansukh, H. Cheong and J-K. Kang. "Solution-processed Cu_2ZnSnS_4 absorbers prepared by appropriate inclusion and removal of thiourea for thin film solar cells." *RSC Advances* **4** (2014) 9118-9125.

68. Z. Li, J. C. W. Ho, K. K. Lee, X. Zeng, T. Zhang, L. H. Wong and Y. M. Lam. "Environmentally friendly solution route to kesterite $Cu_2ZnSn(S,Se)_4$ thin films for solar cell applications." *RSC advances* **4** (2014) 26888-26894.

69. Y. Zhang, Q. Ye, J. Liu, H. Chen, X. He, C. Liao, J. Han, H. Wang, J. Mei and W. Lau. "Earth-abundant and low-cost CZTS solar cell on flexible molybdenum foil." *Rsc Advances* **4** (2014) 23666-23669.

70. W-C. Hsu, H. Zhou, S. Luo, T-B. Song, Y-T. Hsieh, H-S. Duan, S. Ye et al. "Spatial element distribution control in a fully solution-processed nanocrystals-based 8.6% $Cu_2ZnSn(S,Se)_4$ device." *ACS nano* **8** (2014) 9164-9172.

71. G. Larramona, S. Bourdais, A. Jacob, C. Choné, T. Muto, Y. Cuccaro, B. Delatouche, C. Moisan, D. Péré and G. Dennler. "8.6% efficient CZTSSe solar cells sprayed from water–ethanol CZTS colloidal solutions." *The journal of physical chemistry letters* **5** (2014) 3763-3767.

72. Y. Yang, G. Wang, W. Zhao, Q. Tian, L. Huang and D. Pan. "Solution-processed highly efficient $Cu_2ZnSnSe_4$ thin film solar cells by dissolution of elemental Cu, Zn, Sn, and Se powders." *ACS applied materials & interfaces* **7** (2014) 460-464.

73. V. T. Nguyen, D. Nam, M. Gansukh, S-N. Park, S-J. Sung, D-H. Kim, J-K Kang, C. D. Sai, T. H. Tran and H. Cheong. "Influence of sulfate residue on Cu_2ZnSnS_4 thin films prepared by direct solution method." *Solar Energy Materials and Solar Cells* **136** (2015) 113-119.

74. R. Zhang, S. M. Szczepaniak, N. J. Carter, C. A. Handwerker and R. Agrawal. "A versatile solution route to efficient $Cu_2ZnSn(S,Se)_4$ thin-film solar cells." *Chemistry of Materials* **27** (2015) 2114-2120.

75. G. Larramona, S. Levcenko, S. Bourdais, A. Jacob, C. Choné, B. Delatouche, C. Moisan, J. Just, T. Unold and G. Dennler. "Fine-tuning the Sn content in CZTSSe thin films to achieve 10.8% solar cell efficiency from spray-deposited water–ethanol-based colloidal inks." *Advanced Energy Materials* **5** (2015) 1501404.

76. S-H. Wu, C-W. Chang, H-J. Chen, C-F. Shih, Y-Y. Wang, C-C. Li and S-W. Chan. "High-efficiency $Cu_2ZnSn(S,Se)_4$ solar cells fabricated through a low-cost solution process and a two-step heat treatment." *Progress in Photovoltaics: Research and Applications* **25** (2017) 58-66.

77. J. A. Clark, A. R. Uhl, T. R. Martin and H. W. Hillhouse. "Evolution of Morphology and Composition during Annealing and Selenization in Solution-Processed $Cu_2ZnSn(S,Se)_4$." *Chemistry of Materials* **29** (2017) 9328-9339.

78. Y. E. Romanyuk, C. M. Fella, A. R. Uhl, M. Werner, A. N. Tiwari, T. Schnabel and E. Ahlswede. "Recent trends in direct solution coating of kesterite absorber layers in solar cells." *Solar Energy Materials and Solar Cells* **119** (2013) 181-189.

79. K. Moriya, K. Tanaka and H. Uchiki. "Characterization of Cu_2ZnSnS_4 thin films prepared by photo-chemical deposition." *Japanese Journal of Applied Physics* **44** (2005) 715.

80. A. Fischereder, T. Rath, W. Haas, H. Amenitsch, J. Albering, D. Meischler, S. Larissegger et al. "Investigation of Cu_2ZnSnS_4 formation from metal salts and thioacetamide." *Chemistry of materials* **22** (2010) 3399-3406.

81. A. Wangperawong, J. S. King, S. M. Herron, B. P. Tran, K. Pangan-Okimoto and S. F. Bent. "Aqueous bath process for deposition of Cu_2ZnSnS_4 photovoltaic absorbers." *Thin Solid Films* **519** (2011) 2488-2492.

82. S. S. Mali, P. S. Shinde, C. A. Betty, P. N. Bhosale, Y. W. Oh and P. S. Patil. "Synthesis and characterization of Cu_2ZnSnS_4 thin films by SILAR method." *Journal of physics and chemistry of solids* **73** (2012) 735-740.

83. S. S. Mali, B. M. Patil, C. A. Betty, P. N. Bhosale, Y. W. Oh, S. R. Jadkar, R. S. Devan, Y-R. Ma and P. S. Patil. "Novel synthesis of kesterite Cu_2ZnSnS_4 nanoflakes by successive ionic layer adsorption and reaction technique: characterization and application." *Electrochimica Acta* **66** (2012) 216-221.

84. N. M. Shinde, , D. P. Dubal, D. S. Dhawale, C. D. Lokhande, J. H. Kim and J. H. Moon. "Room temperature novel chemical synthesis of Cu_2ZnSnS_4 (CZTS) absorbing layer for photovoltaic application." *Materials Research Bulletin* **47** (2012) 302-307.

85. N. M. Shinde, C. D. Lokhande, J. H. Kim and J. H. Moon. "Low cost and large area novel chemical synthesis of Cu_2ZnSnS_4 (CZTS) thin films." *Journal of Photochemistry and Photobiology A: Chemistry* **235** (2012) 14-20.

86. Z. Su, C. Yan, K. Sun, Z. Han, F. Liu, J. Liu, Y. Lai, J. Li and Y. Liu. "Preparation of Cu_2ZnSnS_4 thin films by sulfurizing stacked precursor thin films via successive ionic layer adsorption and reaction method." *Applied Surface Science* **258** (2012) 7678-7682.

87. C. Gao, H. Shen, F. Jiang and H. Guan. "Preparation of Cu_2ZnSnS_4 film by sulfurizing solution deposited precursors." *Applied Surface Science* **261** (2012) 189-192.

88. M. Cao, L. Li, B. L. Zhang, J. Huang, L. J. Wang, Y. Shen, Y. Sun, J. C. Jiang and G. J. Hu. "One-step deposition of Cu_2ZnSnS_4 thin films for solar cells." *Solar Energy Materials and Solar Cells* **117** (2013) 81-86.

89. X. Liu, C. Wang, J. Xu, X. Liu, R. Zou, L. Ouyang, X. Xu, X. Chen and H. Xing. "Fabrication of $ZnO/CdS/Cu_2ZnSnS_4$ p–n heterostructure nanorod arrays via a solution-based route." *Crystal Engineering Communications* **15** (2013) 1139-1145.

90. A. V. Kumar, N-K. Park and E-T. Kim. "A simple chemical approach for the deposition of Cu_2ZnSnS_4 thin films." *Physica Status Solidi (a)* **211** (2014) 1857-1859.

91. B. U. Maheshwari and V. S. Kumar. "Influence of annealing on p-type Cu_2ZnSnS_4 thin film by dip coating solution growth technique for the application of solar cell." *Journal of Modern Optics* **61** (2014) 1225-1230.

92. E. P. Subramaniam, G. Rajesh, N. Muthukumarasamy, M. Thambidurai, V. Asokan, D. Velauthapillai. “Solar cells of Cu_2ZnSnS_4 thin films prepared by chemical bath deposition method.” *Indian Journal of Pure & Applied Physics* **52** (2014) 620-624.

93. J. Li, G. Chen, C. Xue, X. Jin, W. Liu and C. Zhu. "$Cu_2ZnSn(S_{1-x}Se_x)_4$ solar cells fabricated with precursor stacked layer ZnS/Cu/SnS by a CBD method." *Solar Energy Materials and Solar Cells* **137** (2015) 131-137.

94. Y. Sun, H. Zheng, X. Li, K. Zong, H. Wang, J. Liu, H. Yan and K. Li. "Reaction routes for the formation of a Cu_2ZnSnS_4 absorber material from homogenous ethanol-based solution." *RSC Advances* **3** (2013) 22095-22101.

95. Y. Sun, K. Zong, H. Zheng, H. Wang, J. Liu, H. Yan and M. Zhu. "Ethylene glycol-based dip coating route for the synthesis of Cu_2ZnSnS_4 thin film." *Materials Letters* **92** (2013) 195-197.

96. K. Tanaka, N. Moritake and H. Uchiki. "Preparation of Cu_2ZnSnS_4 thin films by sulfurizing sol–gel deposited precursors." *Solar Energy Materials and Solar Cells* **91** (2007) 1199-1201.

97. G. Rajesh, N. Muthukumarasamy, E. P. Subramaniam, S. Agilan and D. Velauthapillai. "Synthesis of Cu_2ZnSnS_4 thin films by dip-coating method without sulphurization." *Journal of sol-gel science and technology* **66** 2 (2013) 288-292.

98. G. Chen, J. Li, M. Wu, J. Liu, F. Lai and C. Zhu. "Effect of post sulfurization temperature on the microstructure of $Cu_2ZnSn(S,Se)_4$ thin film." *Materials Letters* **159** (2015) 32-34.

99. K. V. Gurav, , S. W. Shin, U. M. Patil, M. P. Suryawanshi, S. M. Pawar, M. G. Gang, S. A. Vanalakar, J. H. Yun and J. H. Kim. "Improvement in the properties of CZTSSe thin films by selenizing single-step electrodeposited CZTS thin films." *Journal of Alloys and Compounds* **631** (2015) 178-182.

100. D-C. Nguyen, S. Ito and D. V. A. Dung. "Effects of annealing conditions on crystallization of the CZTS absorber and photovoltaic properties of $Cu_2(Zn,Sn)(S,Se)_4$ solar cells." *Journal of Alloys and Compounds* **632** (2015) 676-680.

101. S. Ranjbar, M. R. R. Menon, P. A. Fernandes and A. F. Da Cunha. "Effect of selenization conditions on the growth and properties of $Cu_2ZnSn(S,Se)_4$ thin films." *Thin solid films* **582** (2015) 188-192.

102. S. Hwang, D-H. Kim, D-H. Son, K-J. Yang, D. Nam, H. Cheong, J-K. Kang and S-I. In. "Effects of a pre-annealing treatment (PAT) on $Cu_2ZnSn(S,Se)_4$ thin films prepared by rapid thermal processing (RTP) selenization." *Solar Energy Materials and Solar Cells* **143** (2015) 218-225.

103. M. G. Gang, K. V. Gurav, S. W. Shin, C. W. Hong, J. H. Min, M. P. Suryawanshi, S. A. Vanalakar, D. S. Lee and J. H. Kim. "A 5.1% efficient kesterite Cu_2ZnSnS_4 (CZTS) thin film solar cell prepared using modified sulfurization process." *Physica Status Solidi (c)* **12** (2015) 713-716.

104. P. Jackson, D. Hariskos, R. Wuerz, W. Wischmann and M. Powalla. "Compositional investigation of potassium doped Cu (In, Ga) Se2 solar cells with efficiencies up to 20.8%." *Physica Status Solidi (RRL)–Rapid Research Letters* **8** (2014) 219-222.

105. G. Choudhary and H. Hansen. "Human health perspective of environmental exposure to hydrazines: A review." *Chemosphere* **37** (1998) 801-843.

106. F. J. C. Roe, G. A. Grant and D. M. Millican. "Carcinogenicity of hydrazine and 1, 1-dimethylhydrazine for mouse lung." *Nature* **216** (1967) 375.

107. Z. Su, K. Sun, Z. Han, F. Liu, Y. Lai, J. Li and Y. Liu. "Fabrication of ternary Cu–Sn–S sulfides by a modified successive ionic layer adsorption and reaction (SILAR) method." *Journal of Materials Chemistry* **22** (2012) 16346-16352.

108. H. Katagiri. "Cu_2ZnSnS_4 Thin Film Solar Cells." *Thin Solid Films* **480–481** (2005) 426–432.

109. A. Weber, R. Mainz and H. W. Schock. "On the Sn loss from thin films of the material system Cu–Zn–Sn–S in high vacuum." *Journal of Applied Physics* **107** (2010) 013516.

110. W. J. Timo, J. Engman, M. Edoff and C. Platzer-Björkman. "Direct evidence of current blocking by ZnSe in Cu2ZnSnSe4 solar cells." *Applied Physics Letters* **100** (2012) 173510.

111. W-C. Hsu, I. Repins, C. Beall, C. DeHart, G. Teeter, B. To, Y. Yang and R. Noufi. "The effect of Zn excess on kesterite solar cells." *Solar Energy Materials and Solar Cells* **113** (2013) 160-164.

112. Y. Ren, N. Ross, J. K. Larsen, K. Rudisch, J. J. Scragg and C. Platzer-Björkman. "Evolution of Cu_2ZnSnS_4 during non-equilibrium annealing with quasi-in situ monitoring of sulfur partial pressure." *Chemistry of Materials* **29** (2017) 3713-3722.

113. B. Shin, Y. Zhu, N. A. Bojarczuk, S. J. Chey and S. Guha. "Control of an interfacial $MoSe_2$ layer in $Cu_2ZnSnSe_4$ thin film solar cells: 8.9% power conversion efficiency with a TiN diffusion barrier." *Applied Physics Letters* **101** (2012) 053903.

114. C-J. Hsu, H-S. Duan, W. Yang, H. Zhou and Y. Yang. "Benign solutions and innovative sequential annealing processes for high performance $Cu_2ZnSn(Se,S)_4$ photovoltaics." *Advanced Energy Materials* **4** (2014) 1301287.

115. C. Platzer-Björkman, J. J. Scragg, H. Flammersberger, T. Kubart and M. Edoff. "Influence of precursor sulfur content on film formation and compositional changes in Cu_2ZnSnS_4 films and solar cells." *Solar Energy Materials and Solar Cells* **98** (2012) 110-117.

116. A. Emrani, P. Vasekar and C. R. Westgate. "Effects of sulfurization temperature on CZTS thin film solar cell performances." *Solar Energy* **98** (2013) 335-340.

117. A. I. Inamdar, S. Lee, K-Y. Jeon, C. H. Lee, S. M. Pawar, R. S. Kalubarme, C. J. Park, H. Im, W. Jung and Hyungsang Kim. "Optimized fabrication of sputter deposited Cu_2ZnSnS_4 (CZTS) thin films." *Solar Energy* **91** (2013) 196-203.

118. J. H. Lee, H. J. Choi, W. M. Kim, J. H. Jeong and J. K. Park. "Effect of pre-annealing on the phase formation and efficiency of CZTS solar cell prepared by sulfurization of Zn/(Cu, Sn) precursor with H_2S gas." *Solar Energy* **136** (2016) 499-504.

119. H. Guan, H. Shen, C. Gao and X. He. "Sulfurization time effects on the growth of Cu_2ZnSnS_4 thin films by solution method." *Journal of Materials Science: Materials in Electronics* **24** (2013) 2667-2671.

120. P. A. Fernandes, P. M. P. Salomé, A. F. Sartori, J. Malaquias, A. F. Da Cunha, B-A. Schubert, J. C. González and G. M. Ribeiro. "Effects of sulphurization time on Cu_2ZnSnS_4 absorbers and thin films solar cells obtained from metallic precursors." *Solar Energy Materials and Solar Cells* **115** (2013) 157-165.

121. K. Maeda, K. Tanaka, Y. Nakano and H. Uchiki. "Annealing temperature dependence of properties of Cu_2ZnSnS_4 thin films prepared by sol–gel sulfurization method." *Japanese Journal of Applied Physics* **50** (2011) 05FB08.

122. H. S. Duan, W. Yang, B. Bob, C-J. Hsu, B. Lei and Y. Yang. "The role of sulfur in solution-processed $Cu_2ZnSn(S,Se)_4$ and its effect on defect properties." *Advanced Functional Materials* **23** (2013) 1466-1471.

123. C. Voss, Y-J. Chang, S. Subramanian, S. O. Ryu, T-J. Lee, and C-H. Chang. "Growth kinetics of thin-film cadmium sulfide by ammonia-thiourea based CBD." *Journal of the Electrochemical Society* **151** (2004) C655-C660.

124. K. Orgassa, H.W. Schock and J.H. Werner. “Alternative back contact materials for thin film $Cu(In,Ga)Se_2$ solar cells.” *Thin Solid Films* **431–432** (2003) 387–391.

125. W.N. Shafarman and J.E. Phillips. “Direct current–voltage measurements of the Mo/ $CuInSe_2$ contact on operating solar cells.” *Proceedings of the 25th IEEE Photovoltaic Specialists Conference* (1996) 917–919.

126. I. Repins, M.A. Contreras, B. Egaas, C. DeHart, J. Scharf, C.L. Perkins, B. To and R. Noufi. “19.9%- efficienct ZnO/CdS/$CuInGaSe_2$ solar cell with 81.2% fill factor.” *Prog. Photovoltaics Res. Appl.* **16** (2008) 235–239.

127. J.H. Scofield, A. Duda, D. Albin, B.L. Ballard and P.K. Predecki. “Sputtered molybdenum bilayer back contact for copper indium diselenide-based polycrystalline thin-film solar cells.” *Thin Solid Films* **260** (1995) 26–31.

128. H.M. Wu, S.C. Liang, Y.L. Lin, C.Y. Ni, H.Y. Bor, D.C. Tsai and F.S. Shieu. “Strucuture and electrical properties of Mo back contact for $Cu(In, Ga)Se_2$ solar cells.” *Vacuum* **86** (2012) 1916–1919.

129. N. Akcay, N. Akin, B. Comert and S. Ozcelik. “Temperature effects on the structural, optical, electrical and morphological properties of the RF-sputtered Mo thin films.” *Journal of Material Science: Materials in Electronics* **28** (2017) 399–406.

130. https://www.indiamart.com/proddetail/afm-atomic-force-microscopy-16339203312.html

131. L. J. Vander Pauw. “A method of measuring specific resistivity and hall effect of dics of arbitrary shape” *Philips Research Reports* **13** (1958) 1-9.

132. L. E. Brus. “Quantum crystallites and nonlinear optics.” *Applied Physics A* **53** (1991) 465-474.

133. N. Saxena, P. Kumar, V. Gupta and D. Kanjilal. "“Radiation stability of CBD grown nanocrystalline CdS films against ion beam irradiation for solar cell applications” *Journal of Material Science: Materials in Electronics* **29** (2018) 13.

134. R. Rossetti, R. Hull, J. M. Gibson, and Louis E. Brus. "Excited electronic states and optical spectra of ZnS and CdS crystallites in the range of 15 to 50 Å size range: Evolution from molecular to bulk semiconducting properties." *The Journal of chemical physics* **82** (1985) 552-559.

135. J. K. Dongre, V. Nogriya and M. Ramrakhiani. “Structural, optical and photoelectrochemical characterization of CdS nanowire synthesized by chemical bath deposition and wet chemical etching” *Applied Surface Science* **255** (2009) 6115-6120.

136. A. Kadhim, A. Hmood, and H. Abu Hassan. "Physical properties of $Bi_2(Te,Se)_3$ and $Bi_2Se_{1.2}Te_{1.8}$ prepared using solid-state microwave synthesis." *Materials letters* **65** (2011) 3105-3108.

137. A. E. Rakhshani and A. S. Al-Azab. "Characterization of CdS films prepared by chemical-bath deposition." *Journal of Physics: Condensed Matter* **12** (2000) 8745.

138. S. R Gosavi, C. P Nikam, A. R Shelke, A. M Patil, S-W Ryu, J. S Bhat and N. G Deshpande. “Chemical synthesis of porous web-structured CdS thin films for photosensor applications” *Materials Chemistry and Physics.* **160** (2015) 244-250.

139. L. Barabási, L. and H. E. Stanley. *Fractal Concepts in Surface Growth* (Cambridge University Press, 1995).

140. P. Meakin. *Fractals, Scaling and Growth Far From Equilibrium* (Cambridge University Press, 1998).

141. J. Krim and G. Palasantzas. “Experimental observations of self-affine scaling and kinetic roughening at sub-micron length scales.” *Int. J. Mod. Phys. B* **9** (1995) 599-632.

142. M. A. Muñoz. “Multiplicative noise in non-equilibrium phase transitions: a tutorial.” *Advances in Condensed Matter and Statistical Physics*." (2004) 37-68.

143. S. Steudel, S. De Vusser, S. De Jonge, D. Janssen, S. Verlaak, J. Genoe and P. Heremans. “Influence of the dielectric roughness on the performance of pentacene transistors.” *Applied Physics Letters* ***85*** (2004) 4400-4402.

144. A. Rosengren, L. M. Bjursten, N. Danielsen, H. Persson, and M. Kober. "Tissue reactions to polyethylene implants with different surface topography." *Journal of Materials Science: Materials in Medicine* **10** (1999) 75-82.

145. M. Berginski, J. Hüpkes, M. Schulte, G. Schöpe, H. Stiebig, B. Rech, and M. Wuttig. "The effect of front ZnO: Al surface texture and optical transparency on efficient light trapping in silicon thin-film solar cells." *Journal of applied physics* **101** (2007) 074903.

146. H. Gao and W. D. Nix. "Surface roughening of heteroepitaxial thin films." *Annual Review of Materials Science* **29** (1999) 173-209.

147. M. Kardar, G. Parisi, and Y.-C. Zhang. "Dynamic scaling of growing interfaces." *Physical Review Letters* **56** (1986) 889-892.

148. F. Family and T. Vicsek. *Dynamics of Fractal Surfaces* (World Scientific, 1991).

149. L. Vázquez, R. C. Salvarezza and A. J. Arvia. "Validity of the linear growth equation for interface evolution for copper electrodeposition in the presence of organic additives." *Physical review letters* **79** (1997) 709-712.

150. B. E. Roberds and S. N. Farrens. “An atomic force microscopy study on the roughness of silicon wafers correlated with direct wafer bonding.” *Journal of Electrochemical Society* **143** (1996) 2365-2371.

151. J. M. López, M. A. Rodriguez and R. Cuerno. "Superroughening versus intrinsic anomalous scaling of surfaces." *Physical Review E* **56** (1997) 3993-3998.

152. M. Castro, R. Cuerno, A. Sánchez and F. Domínguez-Adame. "Anomalous scaling in a nonlocal growth model in the Kardar-Parisi-Zhang universality class." *Physical Review E* **57** (1998) R2491-R9494.

153. J. J. Ramasco, J. M. López and M. A. Rodríguez. "Generic dynamic scaling in kinetic roughening." *Physical review letters* **84** (2000) 2199-2202.

154. N. Pand and W. Tzeng. “Interfaces with superroughness.” *Physical Review E* **61** (2000) 3559-3563.

155. J. M. Lo´pez and J. Scmittbuhl. “Anomalous scaling of fracture surfaces.” *Physical Review E* **57** (1998) 6405-6408.

156. S. Morel, J. Schmittbuhl, J. M. Lo´pez and G. Valentin. “Anomalous roughening of wood fractured surfaces.” *Physical Review E* **58** (1998) 6999-7005.

157. H. N. Yang, G. C. Wang and T. M. Lu. "Instability in low-temperature molecular-beam epitaxy growth of Si/Si (111)." *Physical review letters* **73** (1994) 2348-2351.

158. Z-J. Liu, N. Jiang, Y. G. Shen and Y-W. Mai. "Atomic force microscopy study of surface roughening of sputter-deposited TiN thin films." *Journal of applied physics* **92** (2002) 3559-3563.

159. J. J. Yang, B. Liu, Y. Wang and K. W. Xu. "Homologous temperature dependence of global surface scaling behaviors of polycrystalline copper films." *Applied Physics Letters* **95** (2009) 194104.

160. M. A. Auger, L. Vázquez, R. Cuerno, M. Castro, M. Jergel and O. Sánchez. “Intrinsic anomalous surface roughening of TiN films deposited by reactive sputtering.” *Physical Review B* **73** (2006) 045436.

161. D. Siniscalco, M. Edely, J. F. Bardeau and N. Delorme. “Statistical Analysis of mounded surfaces: Application to the evolution of ultrathin gold film morphology with deposition temperature.” *Langmuir* **29** (2013) 717-726.

162. J. M. López, M. Castro and R. Gallego. "Scaling of local slopes, conservation laws, and anomalous roughening in surface growth." *Physical review letters* **94** (2005) 166103.

163. B. C. Mohanty, H. R. Choi and CY. S. Cho. “Fluctuations in global surface scaling behavior in sputter-deposited ZnO thin films. *EuroPhysics Letters* **93** (2011) 26003.

164. S. Huo and W. Schwarzacher. "Anomalous scaling of the surface width during Cu electrodeposition." *Physical review letters* **86** (2001) 256-259.

165. R. Aogaki, K. Kitazawa, Y. Kose and K. Fueki. "Theory of powdered crystal formation in electrocrystallization—Occurrence of morphological instability at the electrode surface." *Electrochimica Acta* **25** (1980) 965-972.

166. Y. Xu, X. M. Ge, B. Y. Du, C. Xu, Y. W. Wang and J. Z. Jiang. "Anomalous scaling in amorphous PdNiP films electrodeposition." *Journal of The Electrochemical Society* **155** (2008) D731-D733.

167. M. Saitou. “Anomalous scaling of nickel surfaces in pulse-current electrodeposition growth.” *Physical Review B* **66** (2002) 073416.

168. N. M. Hasan, J. J. Mallett, S. G. dos Santos Filho, A. A. Pasa and W. Schwarzacher. "Dynamic scaling of the surface roughness of Cu deposited using a chemical bath." *Physical Review B* **67** (2003) 081401.

169. I. J. Lee, M. Yun, S-M. Lee and J-Y. Kim. "Growth mechanisms of vapor-born polymer films." *Physical Review B* **78** (2008) 115427.

170. K. Woo, Y. Kim and J. Moon. "A non-toxic, solution-processed, earth abundant absorbing layer for thin-film solar cells." *Energy & Environmental Science* **5** (2012) 5340-5345.

171. L. Pauling, *General Chemistry*. (W.H. Freeman and Company, San Francisco, 1970).

172. C. G. Munce, G. K. Parker, S. A. Holt and G. A. Hope. "A Raman spectroelectrochemical investigation of chemical bath deposited CuxS thin films and their modification." *Colloids and Surfaces A: Physicochemical and Engineering Aspects* **295** (2007) 152-158.

173. K. Borgohain, N. Murase and S. Mahamuni. "Synthesis and properties of Cu 2 O quantum particles." *Journal of applied physics* **92** (2002) 1292-1297.

174. J. Ghijsen, L-H. Tjeng, J. V. Elp, H. Eskes, J. Westerink, G. A. Sawatzky and M. T. Czyzyk. "Electronic structure of Cu_2O and CuO." *Physical Review B* **38** (1988) 11322-11330.

175. V. M. Dzhagan, A. P. Litvinchuk, M. Kruszynska, J. Kolny-Olesiak, M. Y. Valakh and D. RT Zahn. "Raman scattering study of Cu_3SnS_4 colloidal nanocrystals." *The Journal of Physical Chemistry C* **118** (2014) 27554-27558.

176. A. Weber, R. Mainz, T. Unold, S. Schorr and H-W. Schock. “In-situ XRD on formation reactions of Cu_2ZnSnS_4 thin films” *Physica Status Solidi C* **6** (2009) 1245–1248.

177. A. J. Smith, P. E. Meek and W. Y. Liang. "Raman scattering studies of SnS2 and $SnSe_2$." *Journal of Physics C: Solid State Physics* **10** (1977) 1321-1333.

178. P. A. Fernandes, P. M. P. Salomé and A. F. Da Cunha. "A study of ternary Cu2SnS3 and Cu3SnS4 thin films prepared by sulfurizing stacked metal precursors." *Journal of Physics D: Applied Physics* **43** (2010) 215403.

179. T. He, N. Lin, Z. Du, Y. Chao and J. Cui. "The role of excess Sn in $Cu_4Sn_7S_{16}$ for modification of the band structure and a reduction in lattice thermal conductivity." *Journal of Materials Chemistry C* **5** (2017) 4206-4213.

180. A. Fairbrother, V. Izquierdo-Roca, X. Fontané, M. Ibáñez, A. Cabot, E. Saucedo and A. Pérez-Rodríguez. "ZnS grain size effects on near-resonant Raman scattering: optical non-destructive grain size estimation." *Crystal Engineering Communications* **16** (2014) 4120-4125.

181. A. Khare, B. Himmetoglu, M. Johnson, D. J. Norris, M. Cococcioni and E. S. Aydil. "Calculation of the lattice dynamics and Raman spectra of copper zinc tin chalcogenides and comparison to experiments." *Journal of Applied Physics* **111** (2012) 083707 1-9.

182. Y. Li, Q. Han, T. W. Kim and W. Shi. "Synthesis of wurtzite–zincblende Cu_2ZnSnS_4 and $Cu_2ZnSnSe_4$ nanocrystals: insight into the structural selection of quaternary and ternary compounds influenced by binary nuclei." *Nanoscale* **6** (2014) 3777-3785.

183. S. Ji, T. Shi, X. Qiu, J. Zhang, G. Xu, C. Chen, Z. Jiang and C. Ye. "A route to phase controllable $Cu_2ZnSn(S_{1-x}Se_x)_4$ nanocrystals with tunable energy bands." *Scientific reports* **3** (2013) 2733.

184. S. C. Riha, B. A. Parkinson and A. L. Prieto. "Solution-based synthesis and characterization of Cu_2ZnSnS_4 nanocrystals." *Journal of the American Chemical Society* **131** (2009) 12054-12055.

185. J. Xu, X. Yang, Q-D. Yang, T-L. Wong and C-S. Lee. "Cu_2ZnSnS_4 hierarchical microspheres as an effective counter electrode material for quantum dot sensitized solar cells." *The Journal of Physical Chemistry C* **116** (2012) 19718-19723.

186. K. Ito and T. Nakazawa. "Electrical and Optical Properties of Stannite-Type Quaternary Semiconductor Thin Films." *Japanese Journal of Applied Physics* **27** (1988) 2094-2097.

187. K. Tanaka, M. Oonuki, N. Moritake and H. Uchiki. "Cu_2ZnSnS_4 thin film solar cells prepared by non-vacuum processing." *Solar Energy Materials and Solar Cells* **93** (2009) 583-587.

188. M. Z. Ansari and N. Khare. "Structural and optical properties of CZTS thin films deposited by ultrasonically assisted chemical vapour deposition" *Journal of Physics D: Applied Physics*, **47** (2014) 185101 (1-6).

189. R. B. V. Chalapathy, G. Sun, J. Byung and T. Ahn. "Fabrication of Cu2ZnSnS4 films by sulfurization of Cu/ZnSn/Cu precursor layers in sulfur atmosphere for solar cells" *Solar Energy Materials and Solar Cells*, **95** (2011) 3216-3221.

190. A. Tang, Z. Li, F. Wang, M. Dou and W. Mao. "Preparation of Cu_2ZnSnS_4 thin films with high carrier concentration and high carrier mobility by optimized annealing." *Journal of Materials Science: Materials in Electronics* **29** (2018) 7613-7620.

191. A. Tang, J. Liu, J. Ji, M. Dou, Z. Li and F Wang. "One-step electrodeposition for targeted off-stoichiometry Cu_2ZnSnS_4 thin films." *Applied Surface Science* **383** (2016) 253-260.

192. K. Ito. *Copper Zinc Tin Sulfide Based Thin Film Solar Cell*. (Wiley, Chichester, 2015).

193. A. D. Collord and H. W. Hillhouse. "Composition control and formation pathway of CZTS and CZTGS nanocrystal inks for kesterite solar cells." *Chemistry of Materials* **27** (2015) 1855-1862.

194. P. W. M. Blom, V. D. Mihailetchi, L. J. A. Koster and D. E. Markov. "Device physics of polymer: fullerene bulk heterojunction solar cells." *Advanced Materials* **19** (2007) 1551-1566.

195. T. Nagano, M. Tsutsui, R. Nouchi, N. Kawasaki, Y. Ohta, Y. Kubozono, N. Takahashi and A. Fujiwara. "Output properties of C60 field-effect transistors with Au electrodes modified by 1-alkanethiols." *The Journal of Physical Chemistry C* **111** (2007) 7211-7217.

196. Y. Liu, Q. Yang, Y. Zhang, Z. Yang and Z. L. Wang. "Nanowire Piezo-phototronic Photodetector: Theory and Experimental Design." *Advanced Materials* **24** (2012) 1410-1417.

197. A. J. Chiquito, C. A. Amorim, O. M. Berengue, L. S. Araujo, E. P. Bernardo and E. R. Leite. "Back-to-back Schottky diodes: the generalization of the diode theory in analysis and extraction of electrical parameters of nanodevices." *Journal of Physics: Condensed Matter* **24** (2012) 225303.

198. S. Ahmed, K. B. Reuter, O. Gunawan, L. Guo, L. T. Romankiw and H. Deligianni. "A high efficiency electrodeposited Cu_2ZnSnS_4 solar cell." *Advanced Energy Materials* **2** (2012) 253-259.

199. J. Ge, Y. Wu, C. Zhang, S. Zuo, J. Jiang, J. Ma, P. Yang and J. Chu. "Comparative study of the influence of two distinct sulfurization ramping rates on the properties of Cu_2ZnSnS_4 thin films." *Applied Surface Science* **258** (2012) 7250-7254.

200. R. Liu, M. Tan, L. Xu, X. Zhang, J. Chen and X. Tang. "Preparation of high-quality Cu_2ZnSnS_4 thin films for solar cells via the improvement of sulfur partial pressure using a static annealing sulfurization approach." *Solar Energy Materials and Solar Cells* **157** (2016) 221-228.

201. S. Padhy, V. Kumar and U. P. Singh. "CZTSSe absorber layer formation and impact of annealing process on its properties." *Journal of Materials Science: Materials in Electronics* **30** (2019) 1100-1108.

202. D. Fan, R. Zhang, Y. Zhu, H. Peng and J. Zhang. "Structural development and dynamic process in sulfurizing precursors to prepare Cu_2ZnSnS_4 absorber layer." *Journal of Alloys and Compounds* **583** (2014) 566-573.

203. B. Shin, O. Gunawan, Y. Zhu, N. A. Bojarczuk, S. J. Chey and S. Guha. "Thin film solar cell with 8.4% power conversion efficiency using an earth-abundant Cu_2ZnSnS_4 absorber." *Progress in Photovoltaics: Research and Applications* **21** (2013) 72-76.

204. S. A. Vanalakar, S. W. Shin, G. L. Agawane, M. P. Suryawanshi, K. V. Gurav, P. S. Patil and J. H. Kim. "Effect of post-annealing atmosphere on the grain-size and surface morphological properties of pulsed laser deposited CZTS thin films." *Ceramics International* **40** (2014) 15097-15103.

205. C. Ritchie, A. S. R. Chesman, M. Styles, J. J. Jasieniak and P. Mulvaney. "Aqueous Synthesis of High-Quality Cu_2ZnSnS_4 Nanocrystals and Their Thermal Annealing Characteristics." *Langmuir* **34** (2018) 1655-1665.

206. Z. Su, K. Sun, Z. Han, H. Cui, F. Liu, Y. Lai, J. Li, X. Hao, Y. Liu and M. A. Green. "Fabrication of Cu_2ZnSnS_4 solar cells with 5.1% efficiency via thermal decomposition and reaction using a non-toxic sol–gel route." *Journal of Materials Chemistry A* **2** (2014) 500-509.

207. I. Gupta and B. C. Mohanty. "Eliminating secondary phases: Understanding kesterite phase evolution of Cu_2ZnSnS_4 thin films grown from ethanol based solutions with high photosensitivity." *Solar Energy* **181** (2019) 214-221.

208. G. Hodes, *Chemical Solution Deposition of Semiconductor Films*, (New York, USA, 2003).

209. K. Patel, V. Kheraj, D.V. Shah, C.J. Panchal, and N.G. Dhere. “Cu_2ZnSnS_4 Thin Films Grown By Dip-Coating: Effects of Annealing.” *Journal of Alloys and Compound* **663** (2016) 842-847.

210. G. Rajesh, N. Muthukumarasamy, D. Velauthapillai and S.K. Batabyal. “Annealing Induced Shape Transformation of CZTS Nanorods Based Thin Films.” *Langmuir* **33** (2017) 6151-6158.

211. R. D’Angelo, C.L.A. Ricardo, A. Mittiga, P. Scardi and M. Leoni. “A Water-and Sulfurization-Free Solution Route to $Cu_{2-X}Zn_{1+X}SnS_4$.” *Journal of Sol-Gel Science and Technololgy* **72** (2014) 490-495.

212. F. Aslan and A. Tumbul. “Non-Vacuum Processed Cu_2ZnSnS_4 Thin Films: Influence of Copper Precursor on Structural, Optical and Morphological Properties.” *Journal of Alloys and Compound* **612** (2014) 1-4.

213. M. Paris, L. Choubrac, A. Lafond, C. Guillot-Deudon and S. Jobic. “Solid-State NMR and Raman Spectroscopy to Address the Local Structure of Defects and the Tricky Issue of the Cu/Zn Disorder in Cu-Poor, Zn-Rich CZTS Materials.” *Inorganic Chemistry* **53** (2014) 8646-8653.

214. P.A. Fernandes, P.M.P. Salomé and A.F. da Cunha. “Growth and Raman Scattering Characterization of Cu_2ZnSnS_4 Thin Films.” *Thin Solid Films* **517** (2009) 2519–2523.

215. Z. Li, A.L.K. Lui, K.H. Lam, L. Xi and Y.M. Lam. “Phase-Selective Synthesis of Cu_2ZnSnS_4 Nanocrystals using Different Sulfur Precursors” *Inorganic Chemistry* **53** (2014) 10874-10880.

216. T.R. Martin, J.K. Katahara, C.N. Bucherl, B.W. Krueger, H.W. Hillhouse and C.K. Luscombe “Nanoparticle Ligands and Pyrolized Graphitic Carbon in CZTSSe Photovoltaic Devices.” *Chemistry of Materials* **28** (2015) 135-145.

217. S.G. Haass, M. Diethelm, M. Werner, B. Bissig, Y.E. Romanyuk and A.N. Tiwari. “11.2% Efficient Solution Processed Kesterite Solar Cell with a Low Voltage Deficit.” *Advanced Energy Materials* **5** (2015) 1500712.

218. T. Schnabel and E. Ahlswede. “On the Interface Between Kesterite Absorber and Mo Back Contact and its Impact on Solution-Processed Thin-Film Solar Cells.” *Solar Energy Materials and Solar Cells* **159** (2017) 290-295.

219. P. Prabeesh, P. Saritha, I.P. Selvam and S.N. Potty. “Fabrication of CZTS Thin Films by Dip Coating Technique for Solar Cell Applications.” *Materials Research Bulletin* **86** (2017) 295-301.

220. T.T. Mau and K.H. Kim. “Synthesis of Cu_2ZnSnS_4 Thin Film Absorbers by Sulfurizing Dip-Coated Precursors.” *Journal of Ceramic Processing Research* **13** (2012) 301-304.

221. Q. Yi, J. Wu, J. Zhao, H. Wang, J. Hu, X. Dai and G. Zou. “Tuning Bandgap of p-Type $Cu_2Zn(Sn,Ge)(S,Se)_4$ Semiconductor Thin Films via Aqueous Polymer-Assisted Deposition.” *ACS Applied Materials and Interfaces* **9** (2017) 1602–1608.

222. Q. Tian, G. Wang, W. Zhao, Y. Chen, Y. Yang, L. Huang and D. Pan. “Versatile and Low-Toxic Solution Approach to Binary, Ternary, and Quaternary Metal Sulfide Thin Films and Its Application in $Cu_2ZnSn(S,Se)_4$ Solar Cells.” *Chemistry of Materials* **26** (2014) 3098–3103.

223. CRC Handbook of Chemistry and Physics, 2008, 12–114.

224. R. Pandiyan, Z.O. Elhmaidi, Z. Sekkat, M. Abd-lefdil and A.E. Khakani. “Reconstructing the Energy Band Electronic Structure of Pulsed Laser Deposited CZTS Thin Films

Intended for Solar Cell Absorber Applications." *Applied Surface Sciences* **396** (2017) 1562-1570.

225. J. J. S. Scragg, L. Choubrac, A. Lafond and T. Ericson. "A low temperature order-disorder transition in Cu_2ZnSnS_4 thin films." *Applied Physics Letters* **104** (2014) 041911 (1-4).

226. C. Rinco´n and R. Ma´rquez. "Defect physics of the $CuInSe_2$ chalcopyrite semiconductor." *Journal of Physics and Chemistry of Solids* **60** (1999) 1865-1873.

227. D. K. Kumar, T. N. Rao and A. Subrahmanyam**. "**Studies on the disorder in DC magnetron sputtered Cu_2ZnSnS_4 (CZTS) thin films grown in sulfide plasma." *Surface and Coatings Technology* **314** (2017) 85-91.

228. S. M. Lee, B. C. Mohanty, Y. H. Jo, D. H. Yeon and Y. S. Cho. "Phase development, microstructure and optical properties of $Cu_2ZnSnSe_4$ thin films modified with Pb and Ti." *Surface Coatings and Technology* **231** (2013) 389–393.

229. G. Zoppi, I .Forbes, R. W. Miles, P. J. Dale, J. J. Scragg and L. M. Peter. "$Cu_2ZnSnSe_4$ thin film solar cells produced by selenization of magnetron sputtered precursors." *Progess in Photovoltaics* **17** (2009) 315–319.

230. M. Dimitrievska, H. Xie, A. Fairbrother, X. Fontane, G. Gurieva, E. Saucedo, A. Perez-Rodriguez, S. Schorr and V. Izquierdo-Roca. "Multiwavelength excitation Raman scattering of $Cu_2ZnSn(S_xSe_{1-x})_4$ ($0 \le x \le 1$) polycrystalline thin films: vibrational properties of sulfoselenide solid solutions." *Applied Physics Letters* **105** (2014) 031913.

231. S. Li and D. Pan. "Cu_2SnSe_3 and alloyed $(ZnSe)_x(Cu_2SnSe_3)_{1-x}$ nanocrystals with a metastable zincblende and wurtzite structure." *Journal of Crystal Growth* **358** (2012) 38-42.

232. G. K. Gupta, A. Garg and A. Dixit. "Electrical and impedance spectroscopy analysis of sol-gel derived spin coated Cu_2ZnSnS_4 solar cell." *Journal of Applied Physics* **123** (2018) 013101.

233. K. Wang, O. Gunawan, T. Todorov, B. Shin, S. J. Chey, N. A. Bojarczuk, D. Mitzi, and S. Guha. "Thermally evaporated Cu_2ZnSnS_4 solar cells." *Applied Physics Letters* **97** (2010) 143508.